

# Electrical impedance tomography for external wound monitoring

*Measurements, signal  
processing and image  
reconstruction*

---

Master thesis submitted in partial fulfillment of the  
requirements for the degree of

**Master in biomedical engineering**

By

**Loris Mendolia**

Under the supervision of

**Pr. Jean-Michel Redouté (ULiège)**

---



*Montefiore Institute of Electrical Engineering and  
Computer Science  
University of Liège - Faculty of Applied Sciences*

Academic year 2021 - 2022

# Abstract

Assessing the state of chronic open wounds and monitoring their healing in the long term is an important but delicate task in the medical world. Manipulating and perturbing traumatized tissues too often hinders the healing process and prolongs the burden for the patient and the medical system. Conversely, ignoring complications such as bacterial infection or necrotic tissue for too long can lead to dramatic consequences, from the need for amputation to septic shock and death.

Nowadays, chronic wound monitoring is still a matter of frequent visual inspections, which requires medical expertise and intrusions into the daily lives of patients.

The Vitapatch research project, for which this thesis has been carried out, aims at solving this issue by creating easily deployable smart sensor patches capable of long-term continuous monitoring of a chronic wound in a non-invasive manner.

This thesis explores the use of bioimpedance spectroscopy to assess the state of human skin, and electrical impedance tomography as an image reconstruction tool to provide a non-intrusive visual assessment of wound healing.

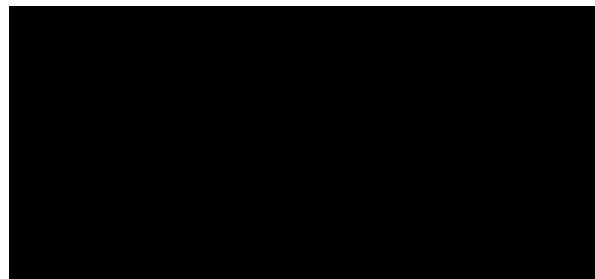
After briefly reminding the concepts of electrical impedance and conduction of electricity, the physiological and electrical properties of human skin and tissues are presented, and the impacts of a wound on these properties are discussed. Then, the methodology for bioimpedance measurements is explained, with specific care toward long-term medical applications. Following, the prototype bioimpedance spectroscopy circuit created by Microsys is analyzed and simulated. After that, the required signal processing steps to make this circuit work are presented, and the journey towards experimental validation of the processing routine is described. Proceeding, electrical impedance tomography is introduced, different algorithms are assessed through simulations and a preliminary application is presented. Adaptations of the EIT problem to wound imaging are performed, and image reconstruction on a finite-element model of wounded skin is simulated. Finally, an experimental setup for wound assessment on phantom skin is presented. Repeated hardware delays and unfinished or faulty components have prevented the completion of real-life experiments, but simulations show promising prospects for a nontraditional approach to impedance spectroscopy and signal processing, as well as for skin modeling and applications of electrical impedance tomography to non-invasive wound imaging.

**Keywords:** *wound monitoring, skin impedance measurements, electrical impedance tomography, impedance spectrum signal processing*

## Declaration of authorship

I, *Loris Mendolia*, hereby declare that this master thesis titled "***Electrical impedance tomography for external wound monitoring : Measurements, signal processing and image reconstruction***" is the product of my own work, unless stated otherwise. I confirm that

- This work was done entirely with the sole purpose of obtaining a master degree at the University.
- Where I have consulted the published work of others for this project, it is always clearly indicated.
- Where I have quoted from the work of others, the source is always given in the bibliography and cited.
- Where this thesis is based on work done by myself jointly with others, the work of other contributors is always attributed to them.
- I have acknowledged all main sources of help.
- In all other cases, the work presented in this document is entirely my own and the result of my research and previous technical knowledge.



---

MENDOLIA Loris  
  
University of Liège

Flémalle, Liège, Belgium  
August 22, 2022

## Acknowledgements

First and foremost, I would sincerely like to thank my academic supervisor Professor Jean-Michel Redouté, and Ir. Morgan Diepart for giving me the opportunity of contributing to the Vitapatch project and entrusting me with this work. I am grateful for their advice and guidance, and for the freedom they gave me to explore the parts of the research I felt were the most relevant and interesting. The teachings and recommendations I received from Prof. Redouté have greatly contributed to the realization of this thesis, as has the research work and the help of Morgan.

I also want to express my thanks to all the other members of the Microsys laboratory who welcomed me into their facilities, gave me access to all the equipment and coffee I needed, took interest in my research, and advised me along the way. Some special thanks also go to Profs. Lionheart and Adler from the Manchester and Carleton Universities, and to the maintainers of the EIDORS software, without whom a big part of the foundations of this work would not exist.

All the professors, lecturers, and teaching assistants of the Faculty of Applied Sciences and the Montefiore Institute of ULiège from whom I was fortunate to receive knowledge, training, and teachings during my years as a student have all contributed to making me the person and engineer I am today. For that, I want to express my gratitude to all of them.

Finally, I want to show appreciation and love to my mother, brother, and grandparents, who have always supported me, cared for me, and provided me with everything I ever needed. They were always the first and last people to believe in me, and I could not have achieved a fraction of what I did in my life without them. My friends, acquaintances, and anyone who ever expressed their support or believed in me also deserve a profound acknowledgment.



# Contents

<b>Introduction</b>	<b>7</b>
<b>0 Electrical impedance primer</b>	<b>10</b>
0.1 Currents, voltages and material properties . . . . .	10
0.2 Definition of electrical impedance . . . . .	11
<b>I Electrical properties of wounded skin</b>	<b>13</b>
I.1 Physiological composition of healthy skin . . . . .	13
I.1.1 The epidermis . . . . .	14
I.1.2 The dermis . . . . .	15
I.1.3 The subcutis . . . . .	15
I.2 Electrical behavior of healthy skin . . . . .	15
I.2.1 Current conduction in biological tissues . . . . .	16
I.2.2 Frequency dependence of current penetration . . . . .	16
I.2.3 Conductivity and permittivity of human skin . . . . .	17
I.2.4 Perturbating effects . . . . .	21
I.3 Impacts of a wound on the electrical properties of the skin . . . . .	23
<b>II Bioimpedance measurements</b>	<b>27</b>
II.1 Bioimpedance measurement setup . . . . .	27
II.1.1 Impedance measurement methodology . . . . .	27
II.1.2 Non-invasive impedance measurement modeling . . . . .	29
II.1.3 Electrical safety and medical standards . . . . .	33
II.2 Impedance measurements of skin and tissues . . . . .	35
II.2.1 Biological potentials and contact variables . . . . .	35
II.2.2 Investigation of suitable electrodes for long-term applications	35
II.2.3 State-of-the-art wound assessment via bioimpedance spectroscopy	40

<b>III</b>	<b>Proposed spectroscopy method and circuit</b>	<b>44</b>
III.1	Prototype PCB description . . . . .	44
III.1.1	Microcontroller . . . . .	45
III.1.2	Excitation signal . . . . .	45
III.1.3	Analog circuit components . . . . .	50
III.1.4	Electrode multiplexing . . . . .	55
III.1.5	Sampling and analog-to-digital conversion . . . . .	55
III.2	Circuit modeling and measurement simulations . . . . .	56
III.2.1	Simulink model . . . . .	56
III.2.2	Frequency response of circuit components . . . . .	57
III.2.3	Electrode modeling . . . . .	60
III.2.4	Simulation results for a basic load . . . . .	61
<b>IV</b>	<b>Signal processing for low-power PRBS spectroscopy</b>	<b>63</b>
IV.1	Fourier analysis for impedance spectroscopy . . . . .	63
IV.2	Machine learning-inspired spectrum de-noising . . . . .	67
IV.2.1	Impact of signal windowing . . . . .	68
IV.2.2	Hampel filtering . . . . .	69
IV.2.3	Least-squares forest boosting for noise removal . . . . .	70
IV.3	Experimental results . . . . .	73
IV.3.1	Experimental setup . . . . .	73
IV.3.2	Initial tests and improvements . . . . .	74
<b>V</b>	<b>Image reconstruction algorithms and methods</b>	<b>81</b>
V.1	Principles of tomographic imaging and EIT . . . . .	82
V.1.1	Traditional tomographic imaging . . . . .	82
V.1.2	Concepts of electrical impedance tomography . . . . .	82
V.2	Electrical impedance tomography algorithms . . . . .	90
V.2.1	The EIDORS software . . . . .	90
V.2.2	Gauss-Newton algorithms . . . . .	90
V.2.3	The Graz consensus algorithm . . . . .	92
V.2.4	Comparison of available EIT algorithms . . . . .	93
V.3	Preliminary application: object imaging in aqueous medium . . . . .	99
V.3.1	Experimental setup . . . . .	100
V.3.2	Results . . . . .	101

<b>VI</b>	<b>Electrical impedance tomography applied to wound imaging</b>	<b>103</b>
VI.1	Adaptation of the reconstruction problem . . . . .	103
VI.1.1	Inadequacy of traditional EIT geometries . . . . .	104
VI.1.2	Skin EIT experimental model . . . . .	106
VI.2	Simulations . . . . .	108
VI.2.1	Injection patterns evaluation . . . . .	108
VI.2.2	Simulated reconstructions on skin layers model . . . . .	113
VI.2.3	Performance numbers . . . . .	117
<b>VII</b>	<b>Experimental setup for skin phantom experimentation</b>	<b>118</b>
VII.1	Experimental setup . . . . .	118
VII.1.1	Measurements . . . . .	118
VII.1.2	Electrode setup . . . . .	119
VII.1.3	Skin phantoms . . . . .	120
VII.2	Results . . . . .	122
	<b>Conclusion and perspectives</b>	<b>123</b>
	<b>Appendices</b>	<b>125</b>
	<b>Bibliography</b>	<b>136</b>

# List of Figures

0.1	Illustration of the concept of a wound monitoring smart sensor patch similar to the one envisioned for the Vitapatch project . . . . .	8
0.2	Example of the impedance spectrum of a R//C dipole . . . . .	12
I.1	Schematic of a section of human skin . . . . .	14
I.2	Cell bi-lipid membrane as a capacitor . . . . .	16
I.3	Evolution of the conductivity and permittivity of human skin with frequency . . . . .	18
I.4	Frequency dependence of the conductivity of individual skin layers . . . . .	20

I.5	Typical frequency dependence of the conductivity and permittivity of biological tissues . . . . .	22
I.6	Evolution of skin resistance, reactance and phase angle around an ulcer during healing . . . . .	24
I.7	Magnitude and phase spectra of wounded tissues at different stages of healing . . . . .	25
I.8	Magnitude impedance spectra of healthy and superficially wounded skin before and after healing . . . . .	25
II.1	Two-point impedance measurements . . . . .	28
II.2	Four-point impedance measurements . . . . .	29
II.3	Cole bioimpedance model . . . . .	30
II.4	Illustration of charge carrier motion at an electrode-electrolyte interface	32
II.5	Electrical models of the electrode-electrolyte interfaces at the surface of the skin . . . . .	33
II.6	Principle of operation of capacitive electrodes . . . . .	37
II.7	Gold electrodes on a PET substrate embedded into medical tape . . . .	39
II.8	Self-adhesive conductive polymer film electrodes . . . . .	40
II.9	Four-point bioimpedance measurement around a pressure ulcer . . . .	41
II.10	Clinical proof-of-concept of a bioimpedance method for monitoring ulcers	42
III.1	Prototype Vitapatch bioimpedance measurement PCB manufactured by Microsys . . . . .	45
III.2	Illustration of a chirp signal in time and frequency domains . . . . .	47
III.3	Illustration of a pseudo-random binary sequence in time and frequency domains . . . . .	49
III.4	Mirrored Modified Howland current source schematic . . . . .	51
III.5	Frequency response of the AD8231 instrumentation amplifier for different gains . . . . .	53
III.6	First order RC filters . . . . .	54
III.7	Bode plot of the mirrored modified Howland current source . . . . .	59
III.8	Bode plot of the voltage amplification and filtering stage . . . . .	60
III.9	Part of the simulated voltage by current ratio sampled for measurement of a 200 $\Omega$ resistor . . . . .	61
III.10	Part of the simulated voltage by current ratio sampled for measurement of a 200 $\Omega$ // 1 $\mu$ F R//C dipole . . . . .	62
IV.1	Illustrations of a sinc function and Hamming window . . . . .	66
IV.2	Simulated magnitude spectrum of a resistive load . . . . .	66
IV.3	Simulated magnitude spectrum of a R//C load . . . . .	67
IV.4	Single-sided magnitude response of the Hamming window applied to the signals . . . . .	68
IV.5	Effect of a Hampel filter on the simulated magnitude spectrum of a resistive load . . . . .	70
IV.6	Effect of a Hampel filter on the simulated magnitude spectrum of an R//C load . . . . .	70

IV.7	Least-squares forest boosting regression of the Hampel-filtered simulated spectrum of a resistive load . . . . .	72
IV.8	Least-squares forest boosting regression of the Hampel-filtered simulated spectrum of a R//C load . . . . .	73
IV.9	Initial signal processing tests on real measured loads . . . . .	74
IV.10	Processed impedance spectrum of a R//C load measured in a Faraday cage . . . . .	75
IV.11	Processed impedance spectrum of a R//C load measured in a Faraday cage . . . . .	76
IV.12	Processed impedance spectrum of a resistive load measured with a battery-powered PCB . . . . .	78
IV.13	Processed impedance spectrum of a R//C load measured with a battery-powered PCB . . . . .	79
IV.14	Zoom on the processed impedance spectra measured with a battery-powered PCB . . . . .	80
V.1	General concept of electrical impedance tomography . . . . .	84
V.2	Illustration of adjacent and opposite injection patterns . . . . .	88
V.3	Finite element model used for algorithm comparison . . . . .	94
V.4	Comparison of Gauss-Newton difference EIT reconstruction priors for a centered object . . . . .	96
V.5	Comparison of Gauss-Newton difference EIT reconstruction priors for an off-center object . . . . .	97
V.6	GREIT reconstruction of the two conductive targets used for algorithm comparison . . . . .	98
V.7	Absolute Gauss-Newton EIT reconstruction with NOSER prior for the centered object . . . . .	98
V.8	Absolute Gauss-Newton EIT reconstruction with NOSER prior for the off-center object . . . . .	98
V.9	Metal piece immersed in the SPECTRA electrode tank filled with tap water . . . . .	101
V.10	3D FEM model of the SPECTRA EIT tank using point electrodes . . . . .	101
V.11	OpenEIT image reconstruction of the metal pieces using the built-in GREIT algorithm . . . . .	102
V.12	EIDORS image reconstruction of the metal pieces using a tuned GREIT algorithm . . . . .	102
VI.1	Qualitative COMSOL simulations of current propagation in a cylinder of skin with a ring of electrodes . . . . .	105
VI.2	Finite element model of a piece of skin with a ring of surface electrodes for forward EIT simulations . . . . .	107
VI.3	Illustration of the reconstruction model on top of the forward FEM model	108
VI.4	First simulated image reconstruction attempts with a circular electrode array on a flat surface . . . . .	109
VI.5	Simulation of the geophysical EIT example . . . . .	110

VI.6	Fixed simulated image reconstruction of the centered object with a circular electrode array on a flat surface . . . . .	111
VI.7	Fixed simulated image reconstruction of the off-center object with a circular electrode array on a flat surface . . . . .	112
VI.8	Difference imaging of several simulated wounds on the skin FEM model	114
VI.9	Absolute imaging of several simulated wounds on the skin FEM model	115
VI.10	GREIT reconstruction of the wound models of Figure VI.9 . . . . .	116
VII.1	3D-printed electrode holding ring . . . . .	120
VII.2	Second version of the 3D-printed electrode holder . . . . .	121
VII.3	Electrode ring applied to pork skin, with a blob of conductive gel as the object to image . . . . .	122

## List of Tables

I.1	Thickness ranges of the conductive layers of human skin . . . . .	15
II.1	Patient auxiliary current limits as a function of frequency according to the IEC 60601-1-11:2015 ISO standard . . . . .	34
VI.1	Computation times of various EIDORS tasks for measurement simulation and image reconstruction . . . . .	117

# Introduction

When an open wound does not heal within a few months, it is considered a chronic wound [1]. These long-term injuries are caused by anomalies in the healing process and are subject to multiple complications. Chronic wounds are a major burden for the victims, causing sharp and frequent pain, and putting them at risk of health complications.

Healing difficulties of a wound can be caused by a variety of factors, such as poor circulation, old age, repeated trauma, or unattended bacterial infection [1, 2]. A major factor for developing chronic wounds is diabetes [2], as diabetic patients tend to have restricted vascular flow and reduced mobility. Lack of frequent movements and sedentarity can cause pressure ulcers, a type of damage to the skin and underlying tissue caused by prolonged pressure on the skin [3]. Bed-ridden patients are also at risk of pressure ulcers for the same reason. Another common type of chronic wound is venous ulcers. These are caused by minor injuries, very often to the leg or foot, which degenerate into more serious ulcers as a result of high venous pressure applied to the traumatized tissue [4]. As diabetes becomes a more widespread problem in modern societies, so do its complications like the apparition of chronic wounds.

To treat chronic wounds, a careful and frequent assessment of their status is required [1]. A variety of specialized treatments such as application of antibiotic agents, removal of necrotic tissue, cleaning, and use of anti-inflammatory ointments, ... are possible to help promote tissue healing. Wound status assessment needs to be performed regularly by medical professionals. Otherwise, patients are at risk of suffering a widespread infection, in addition to prolonged pain caused by the wound itself. However, removing wound dressings every day to examine the wound visually is not an ideal scenario, as it can perturb the healing process and disturb reforming tissues [5, 6]. Moreover, the assessment procedure is subject to variations as it is dependent on the judgment of healthcare professionals and caretakers. Unfortunately, visual wound assessment is still the only solution existing nowadays.

The need for visual monitoring of chronic wounds is a major inconvenience for the medical domain and the quality of life of patients. An estimated 75% of diabetic patients are expected to develop venous ulcers at some point in their lives, which can degenerate to the point of requiring amputation if not attended to [2]. The financial consequences are also relevant, as the workload of medical professionals is increased

and unnecessary replacement of wound dressings leads to increased material costs [5].

## The Vitapatch project

The Vitapatch project is an FNRS research project that aims at creating miniaturized and easily deployable smart sensor patches for healthcare and convenient monitoring. This project is a multi-year project carried out by members of the Microsys laboratory of the Montefiore Institute of the University of Liège and led by Prof. Jean-Michel Redouté. Two distinct applications of smart sensor patches (*SSP*) are envisioned. The first is the measurements of a subject's vital signs, and the second is the monitoring of external chronic wounds. The purpose of this second application is to provide a novel and non-intrusive way of continuously assessing the state of a wound, following its healing, and detecting potential complications at an early stage.

The Vitapatch SSP could be fitted into a wound dressing used for covering large wounds such as those described at the beginning of this introduction. By being in contact with the tissues surrounding the wound, the patch would perform bioimpedance measurements to assess the state of the wound in a continuous and non-invasive manner and provide warnings when attention is required. This patch would be easily applied to the body and use ultra-low power solutions to guarantee long-term monitoring. To process the measured data, state-of-the-art Internet of Things protocols would be used to efficiently transfer the measurements to another device for data analysis and processing. A smartphone could be used as an intermediate gateway to a server, or as the processing device itself.

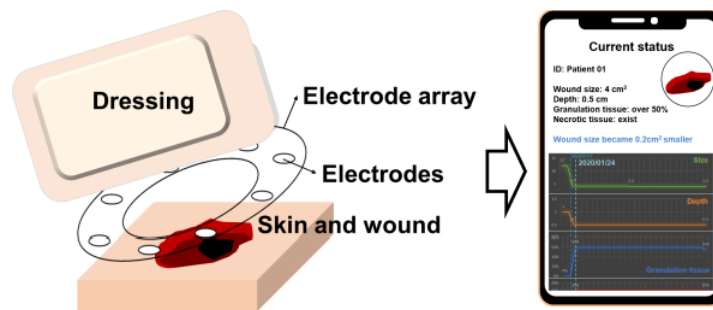


Figure 0.1: Illustration of the concept of a wound monitoring smart sensor patch similar to the one envisioned for the Vitapatch project (from [7])

## Goals of this thesis

This master thesis takes place in the context of the Vitapatch wound monitoring project. My first objective was to work in collaboration with Microsys and Ir. Morgan Diepart, responsible for the circuit design of the SSP, analyze the data obtained with



this circuit and develop appropriate signal processing routines for interpreting the bioimpedance measurements.

Based on these measurements, my second objective was to create or find image reconstruction protocols to create representative images of the status of the wound. My research led me to experiment with Electrical Impedance Tomography, a promising image reconstruction protocol based on impedance measurements of heterogeneous materials. EIT applications already exist for lung or brain imaging, but its use is not widespread in the medical field today.

A natural first step for this thesis was to study the electrical properties of the skin and the specificities of bioimpedance measurement protocols, to understand the meaning of bioimpedance changes, and perform suitable and safe measurements. Additionally, simulated and real-life experiments on suitable materials that mimic human skin, referred to as skin phantoms, were also envisioned to test my work on signal processing and image reconstruction against realistic scenarios.

## Part 0

# Electrical impedance primer

To start this thesis, a brief primer on the concepts of electrical impedance is in order, to improve the comfort of the unfamiliar reader. In this work, electromagnetic effects are not considered.

### 0.1 Currents, voltages and material properties

The scientific field of electricity is based on the presence and motion of charged particles. Electric charge originates from electrons and protons at the subatomic scale. A particle can be positively or negatively charged, with the amount of charge expressed in Coulombs (C). Charge carriers include electrons, ions, holes (absence of electrons in semiconductors), or larger molecules presenting electric charges at their surface. A charge produces an electric field, which affects other charges.

Under the effect of an electric field, charges can move if they are in a certain type of material, called a conductor. Moving electric charges define an electric current. The conductivity  $\sigma$  of a material indicates the ability for charges to move inside of a material. Its inverse, the resistivity  $\rho$ , is an indicator of the energy losses caused by the opposition of a material to current flows.

In other materials, called insulators, charges are not free to move. Some insulators, called dielectrics, still allow charges to rotate and orient themselves in response to an electric field. Similar to the conductivity, the permittivity  $\epsilon$  of a material represents the ability for charges to orient themselves inside of it. When charges of a dielectric material are all oriented in the same direction, the material is said to be polarized.

## 0.2 Definition of electrical impedance

In electricity, impedance is a quantity that expresses the opposition of a material to an alternating current generated by a voltage difference between two points of that material. It is the generalization of the concept of electrical resistance to alternating currents. A voltage is also called an electric potential difference. Electric potential is the negative spatial derivative of the electric field and depends on the number of charges present at any point in space.

For sinusoidal voltages  $V = |V| \sin(\omega t + \phi_V)$  and currents  $I = |I| \sin(\omega t + \phi_I)$  of angular frequency  $\omega$ , Ohm's law defines the impedance as  $Z = \frac{V}{I}$ . Electrical impedance is a complex number that can be expressed as the sum of a real resistance  $R$  and an imaginary reactance  $X$  :

$$Z = R + jX$$

where  $j$  is the imaginary number to avoid confusion with currents.

An impedance can also be expressed as a magnitude  $|Z| = \frac{|V|}{|I|}$  and a phase  $\theta = \phi_V - \phi_I$ , with both quantities being frequency dependent. The magnitude of an impedance indicates the relationship between the amplitude of a current flowing between two points of an impedance and the amplitude of the resulting voltage difference between these two points, for all frequencies. The phase indicates how much phase lag will be observed between the aforementioned current and voltage difference.

The frequency dependence of electrical impedance stems from the existence of three physical occurrences that act on current flow, and that define three types of ideal dipoles :

- Resistance is the ability of a material to oppose a current flow, regardless of frequency. For a homogeneous cylindrical element of resistivity  $\rho$ , length  $l$  and cross-section  $s$ , Pouillet's law defines the electrical resistance as  $R = \rho \frac{l}{s}$ , in Ohms ( $\Omega$ ). The impedance of a purely resistive component is simply its resistance  $Z_R = R$ .
- Self-inductance is an electromagnetic phenomenon in which alternating electrical currents generate a magnetic field which then leads to an induced voltage opposing the currents which gave rise to the magnetic field. Self-inductance  $L$  is expressed in Henrys (H). The impedance of a purely inductive component is directly proportional to its self-inductance and to frequency:  $Z_L = j\omega L$ .
- Capacitance is the ability of an object to accumulate electric charges on either side of itself. These charges accumulate on conductive domains, separated by a dielectric material (an electrical insulator that can be polarized by an electric field). A parallel-plate capacitor has a capacity  $C = \epsilon \frac{s}{d}$ , in Farads (F), for plates of surface  $s$  separated by a distance  $d$  by a dielectric material of permittivity  $\epsilon$ . The permittivity of a material measures its polarizability, and can be expressed as a relative permittivity  $\epsilon_r = \frac{\epsilon}{\epsilon_0}$ , where  $\epsilon_0$  is the permittivity of free space. The

impedance of a purely capacitive component is inversely proportional to both its capacitance and frequency:  $Z_C = \frac{1}{j\omega C}$ .

To illustrate the frequency dependence of electrical impedance, the magnitude and phase of an R//C dipole is illustrated in Figure 0.2. This impedance spectrum shows how much the value of an impedance, and the resulting voltage or current measurements, can vary depending on frequency when inductive or capacitive effects are at play. Additionally, it highlights how measuring an impedance at different frequencies is important to deduce the reactance of a material, as opposed to only its resistance.

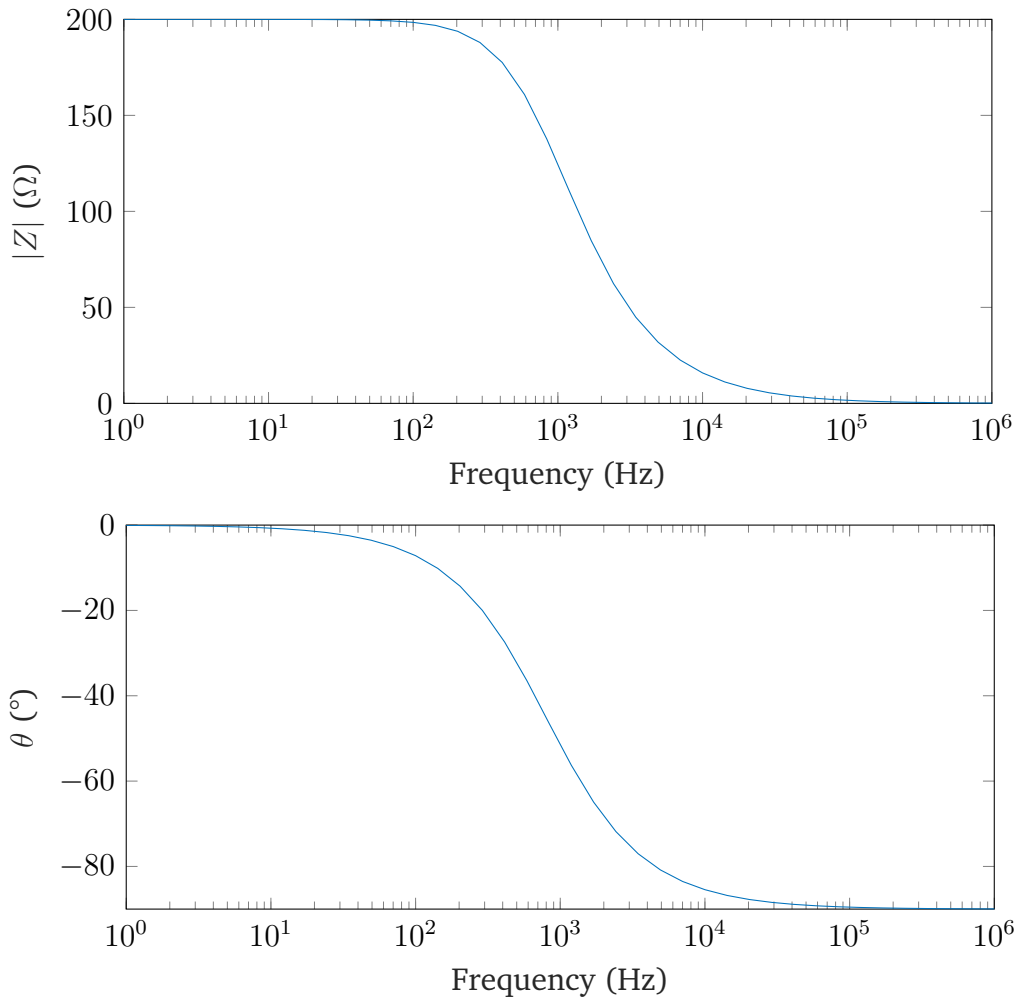


Figure 0.2: Example of the impedance spectrum (magnitude and phase) of an R//C dipole (200 Ω, 1 μF)

## Part I

# Electrical properties of wounded skin

The first step of this project, before electrical measurements and data processing, is to gather information about the electrical properties of the human skin and how these properties are affected by the presence of a wound. This is an important piece of work, as human tissue has a variety of properties that make it a unique material to measure. Notably, human skin cannot be expected to be homogeneous nor isotropic, and currents may cause physiological changes that would affect its electrical properties over time.

Armed with sufficient knowledge about the electrical behavior of human skin, it will be possible to establish suitable models that can be simulated to predict measurement results, compare them with practical ones, and understand the meaning and significance of the observed data.

In this first part, the physiological and electrical properties of healthy skin are summarized through a literature review. Notably, changes related to the frequency of applied currents are investigated. Finally, the consequences of an open wound are discussed, and corresponding changes in electrical impedance are explored.

## I.1 Physiological composition of healthy skin

This first section focuses on describing the different layers making up the human skin without entering into considerations regarding their electrical properties.

The skin is an organ covering the entire human body and providing a variety of functions, such as protecting the underlying tissues from foreign substances and radiations, regulating body temperature and moisture, and providing the sense of touch [8, 9]. These functions require a variety of tissues and cells as well as a certain organization of its different components.

The skin can be separated into three different layers that vary both in composition and functionality, although different classification methods can define up to seven layers. These layers are the epidermis, the dermis, and the subcutis, from the outermost to the innermost [10]. These layers are represented in Figure I.1, and their minimal, typical and maximal thicknesses in a human body are summarized in Table I.1. Knowing the thickness of each layer will be valuable when investigating open wounds and their impacts depending on their penetration depth.

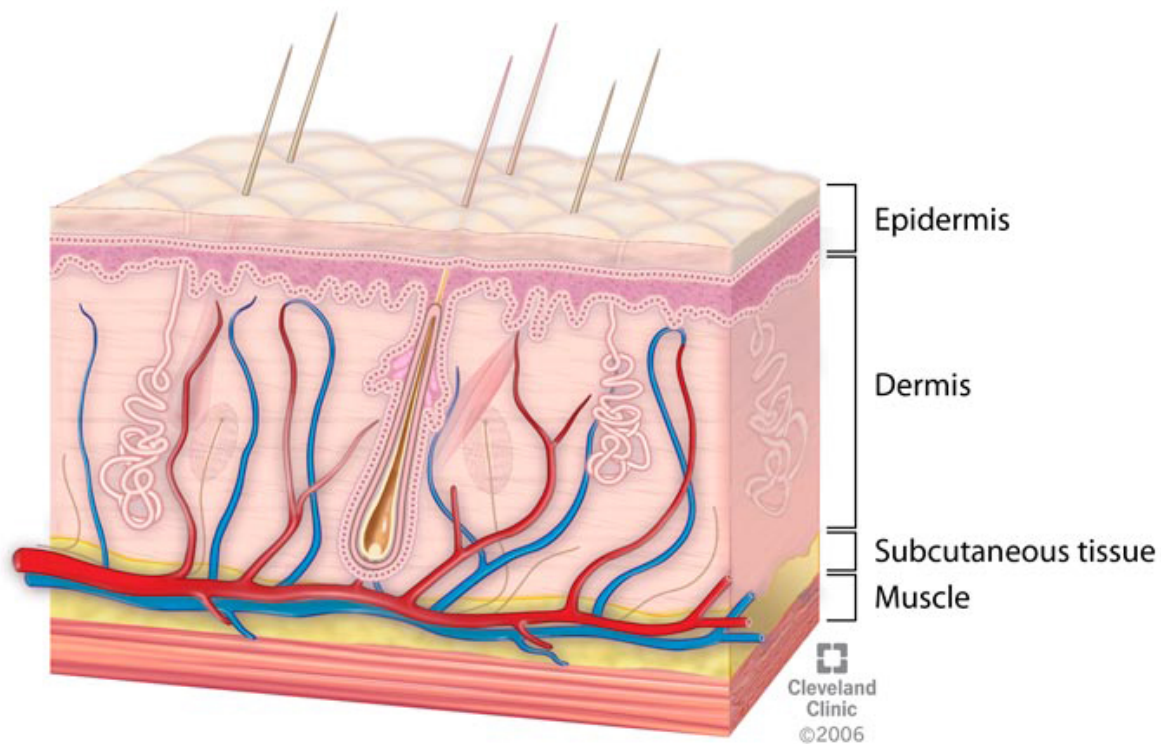


Figure I.1: Schematic of a section of human skin showing the 3 main layers (from [10])

### I.1.1 The epidermis

The epidermis is the external layer of the skin, which is in direct contact with the environment. It is not vascularized and is itself comprised of layers of different cells.

The very outside of the epidermis is called the stratum corneum. The cells that make up this layer are essentially dead, as they are mostly full of keratin and have lost their nuclei. This layer is porous and can absorb or release moisture. Below is the stratum lucidum, or living barrier. This part of the epidermis contains partially keratinized but living cells. It provides a barrier to fluids and is not permeable to anions.

Finally, the inner layer of the epidermis is the malpighian layer or stratum germinativum. This layer contains newly differentiated keratinocytes as well as melanocytes, which produce melanin, the skin pigment converting UV radiation into heat.

The cells making up the epidermis are mostly keratinocytes. They originate from the stratum germinativum and migrate to the outside of the skin as they produce more and more keratin. Keratin is a fibrous protein that plays a key role in the structural integrity and insolubility of the skin and other body parts such as hair and nails.

### I.1.2 The dermis

The dermis is the thickest layer of the skin, situated below the epidermis. Thanks to its matrix arrangement of collagen and elastin fibers, the dermis provides elasticity and mechanical strength to the skin.

The dermis is more varied than the epidermis in terms of its components. It contains fibroblasts, sweat glands, hair follicles, sensory receptors, blood vessels, mast cells, and macrophages among others. This layer is therefore responsible for immune and inflammatory responses, sensory functions, and temperature regulation along with its mechanical role. The dermis also communicates with the epidermis through intertwined ridges to supply it with nutrients, as the latter lacks blood vessels. This also explains why epidermis cells multiply and differentiate at the interface with the dermis.

### I.1.3 The subcutis

The subcutis is the innermost layer of the skin. It mostly contains lipocytes responsible for fat storage and loose connective tissue. The thickness of this layer can vary depending on the anatomical site but will also depend on an individual's nutrition and hormonal status.

Because of its fat supply, the subcutis acts as a good shock absorber and thermally insulating layer.

	Stratum corneum	Epidermis (incl. S.C.)	Dermis
Min. thickness	5 $\mu\text{m}$	50 $\mu\text{m}$ (eyelids)	0.3 mm
Typical thickness	20 $\mu\text{m}$	0.2 mm	variable
Max. thickness	2 mm (palms and soles)	2 mm	3 mm

Table I.1: Thickness ranges of the conductive layers of human skin (based on [9, 11, 12])

## I.2 Electrical behavior of healthy skin

Now that the general composition of human skin and its layers is established, the different electrical properties of skin and tissues can be explored. Because low to medium frequency currents are to be injected into the body through the skin for the Vitapatch project, this section describes how currents will travel inside the tissues and how they can react to it.

### I.2.1 Current conduction in biological tissues

By definition, an electric current is the result of a flow of charge carriers under the action of an electric potential. In regular electrical conductors, charge carriers are free electrons, while they can also be holes (absence of electrons) in semiconductors. In living tissues, currents flow thanks to the motion of dissolved ions [13]. A wide variety of ions are present in various concentrations in cells, blood, and interstitial fluid, which makes the human body a big electrolyte solution.

Generally speaking, the electrical conductivity of an electrolyte can be expected to be lower than the one of traditional electronic conductors because the larger size of ions gives them less mobility inside of the material compared to electrons. Because ion concentrations regulate many physiological processes in living tissues, some unwanted effects could be observed due to the injection of external currents. This concern will be explored later.

### I.2.2 Frequency dependence of current penetration

Every cell of living tissues is encapsulated by a cell membrane made up of two layers of lipids. From an electrical point of view, this bi-lipid layer creates a capacitive barrier between the intra- and extracellular media, as it acts as a dielectric separating two conductive domains, as illustrated in Figure I.2. This explains why it is widely accepted [8, 14, 15] that low-frequency currents will only travel within the extracellular medium, while higher-frequency currents will be able to penetrate the cell membranes and also travel through the cytoplasms of cells.

Therefore, as the frequencies of current increase, the contribution of the intracellular medium to the electrical properties of tissues will do so as well, creating a dependence between current frequency and material properties of living tissues.

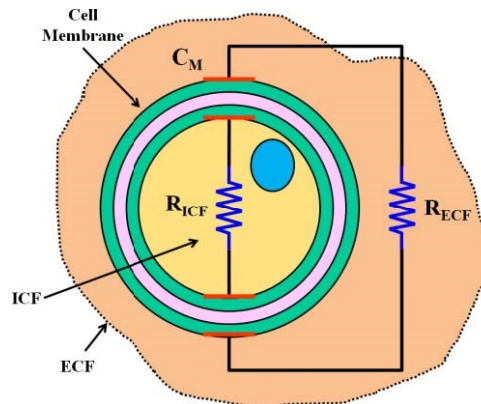


Figure I.2: Cell bi-lipid membrane as a capacitor between the intra- and extracellular media (from [14])



### I.2.3 Conductivity and permittivity of human skin

To establish or use realistic and relevant electrical models of human skin, and interpret the results of electrical measurements, it is useful to gather information about the electrical properties of the skin. Material properties of interest are the electrical conductivity  $\sigma$  (in Siemens per meter, S/m), the inverse of resistivity, and the permittivity (absolute  $\epsilon$  or relative  $\epsilon_r$ , in Farads per meter F/m or dimensionless) of the skin and underlying tissues.

In the literature, two measurement methodologies exist, and both provide different kinds of information. The first ones are non-invasive in-vivo measurements, measuring the properties of human skin from the outside. These measurements are valuable because they follow the same methodology that will be used in this project and provide a baseline for expected results on healthy skin.

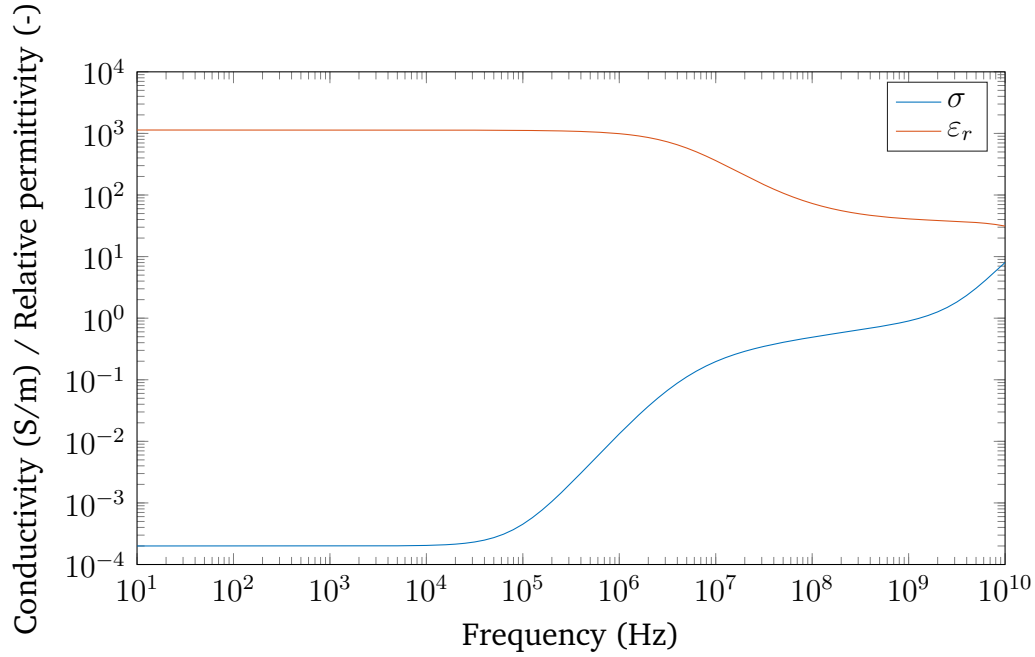
The second types of measurement found in the literature are ex-vivo measurements of the properties of individual skin layers. For modeling purposes and for relating a change in measurement to underlying tissue modifications, these measurements are also valuable, although their ex-vivo nature should be considered with caution as some properties of living tissues may be lost in the process.

#### I.2.3.1 Bulk properties of the skin

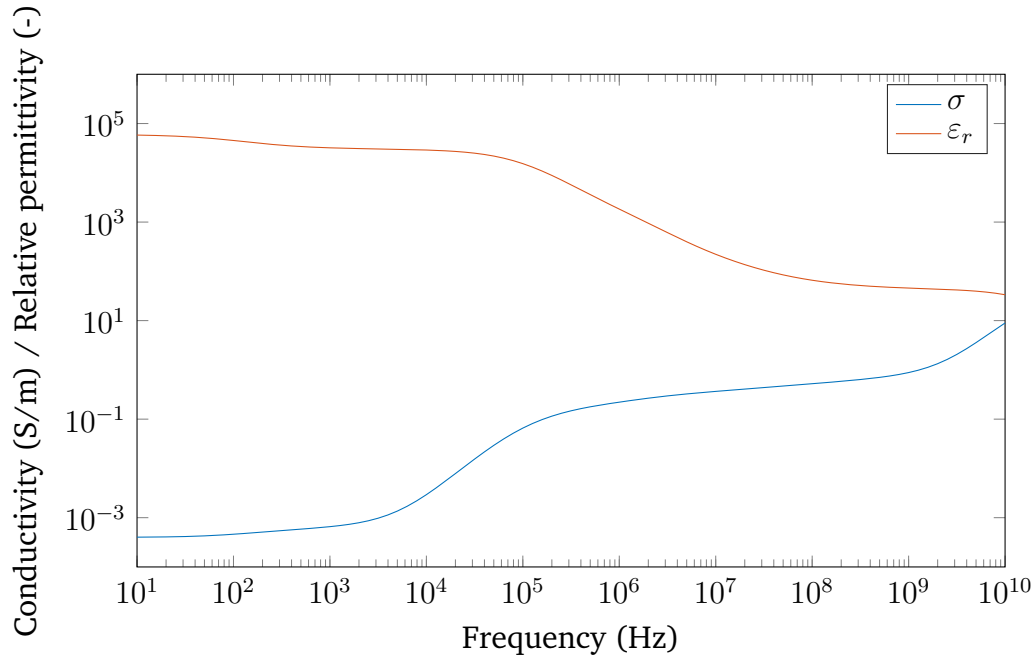
The most popular and widely cited values for in-vivo electrical properties of human tissues, including skin, originate from Gabriel [16] and Gabriel, Lau, and Gabriel [17]. These values were established by performing a large variety of measurements on several human tissues in different frequency ranges. Their massive research work concluded in the creation of parametric models to describe the evolution of electrical properties of tissues with frequency [18], which are leveraged by online databases such as [19] to provide easy access to the conductivity  $\sigma$  and relative permittivity  $\epsilon_r$  at any frequency.

These properties are expected to vary with frequency because of the frequency dependence of current penetration in the cells explained in Section I.2.2, but also because of a phenomenon known as dielectric dispersion, which will be explained later in Section I.2.4.2.

Figure I.3 showcases plots of the bulk skin properties following Gabriel's mathematical models as a function of frequency. Figure I.3a contains data for dry skin and Figure I.3b for wet skin.



(a) Dry skin



(b) Wet skin

Figure I.3: Evolution of the conductivity and permittivity of in vivo human skin with current frequency (from [19])

Both conductivity and permittivity are appreciably higher at low frequencies for wet skin, but these differences dwindle as higher frequency currents are considered. This will make sense later when an analysis of the properties of each skin layer is

presented.

In both types of tissues, conductivity only increases slightly with frequency at first, until a more drastic increase by several orders of magnitude starting around 100 kHz for dry skin and 10 kHz for wet skin. This increase can be explained by the ability of higher frequency currents to overcome the capacitive barrier of cell membranes and flow more freely in the entire tissue.

### I.2.3.2 Individual properties of skin layers

A more recent publication, by Wake, Sasaki, and Watanabe [20], explores conductivity measurements of the epidermis, dermis, and subcutis independently from one another. To that end, skin samples are analyzed through a parallel-plate setup, a common method for measuring the electrical properties of dielectric materials<sup>1</sup>. These measurements were performed at intermediate frequencies, between 10 kHz and 1 MHz, which is the frequency range in which wet skin conductivity started to increase in Figure I.3b.

The measurement results are illustrated in Figure I.4. There are several interesting takeaways to highlight from these graphs.

First, it is important to note that saline solution was applied to the skin samples. Therefore, these measurements should be interpreted as coming from wet skin. In that sense, the measured conductivities of bulk skin in this paper are in accordance with the previous measurements from Gabriel (Figure I.3b), which is a good sign for the validity of these findings.

A very interesting finding is the almost constant conductivity of the dermis and subcutis shown in Figure I.4a. This implies that the frequency dependence of skin conductivity can largely be attributed to the epidermis in this frequency range.

Speaking of the epidermis, not only is it the main reason for the frequency dependence of skin conductivity, Figure I.4b also shows that it is the main contributor to skin resistance, as its conductivity is two orders of magnitude lower than the one of the dermis.

To understand the stark difference between the measured conductivities of wet and dry skin, additional measurements of the individual conductivities of the stratum corneum and underlying layers of the epidermis, performed by Yamamoto and Yamamoto [22] are valuable. Their study involves in-vivo conductivity measurements before and after scraping off the stratum corneum layer. In doing so, they observed an increase in conductivity by two to three orders of magnitude when removing the most keratinized layers of dead cells from the skin.

This implies that the stratum corneum provides the majority of the electrical resistivity of dry skin, and prevents low-intensity currents from penetrating deeper into the inner skin layers, because of the high resistivity of keratin. In non-invasive in-

---

<sup>1</sup>Keysight Technologies. *Materials Measurement: Dielectric Materials*. Application Brief. July 2014. URL: <https://www.keysight.com/us/en/assets/7018-08589/brochures/5989-4713.pdf>.

vivo measurements, the measured conductivity of intact skin therefore mostly reflects the conductivity of the stratum corneum. As mentioned in Section I.1.1, the stratum corneum is porous and can absorb humidity. This seemingly increases the effective penetration depth of currents in in-vivo measurements [23], since the conductivity of (non-deionized) water is around 0.05 S/m, 100 times more than the low-frequency conductivity of the stratum corneum. Wet or scraped skin thus allows the conductivity of the rest of the epidermis and the dermis to have an impact on the measurements.

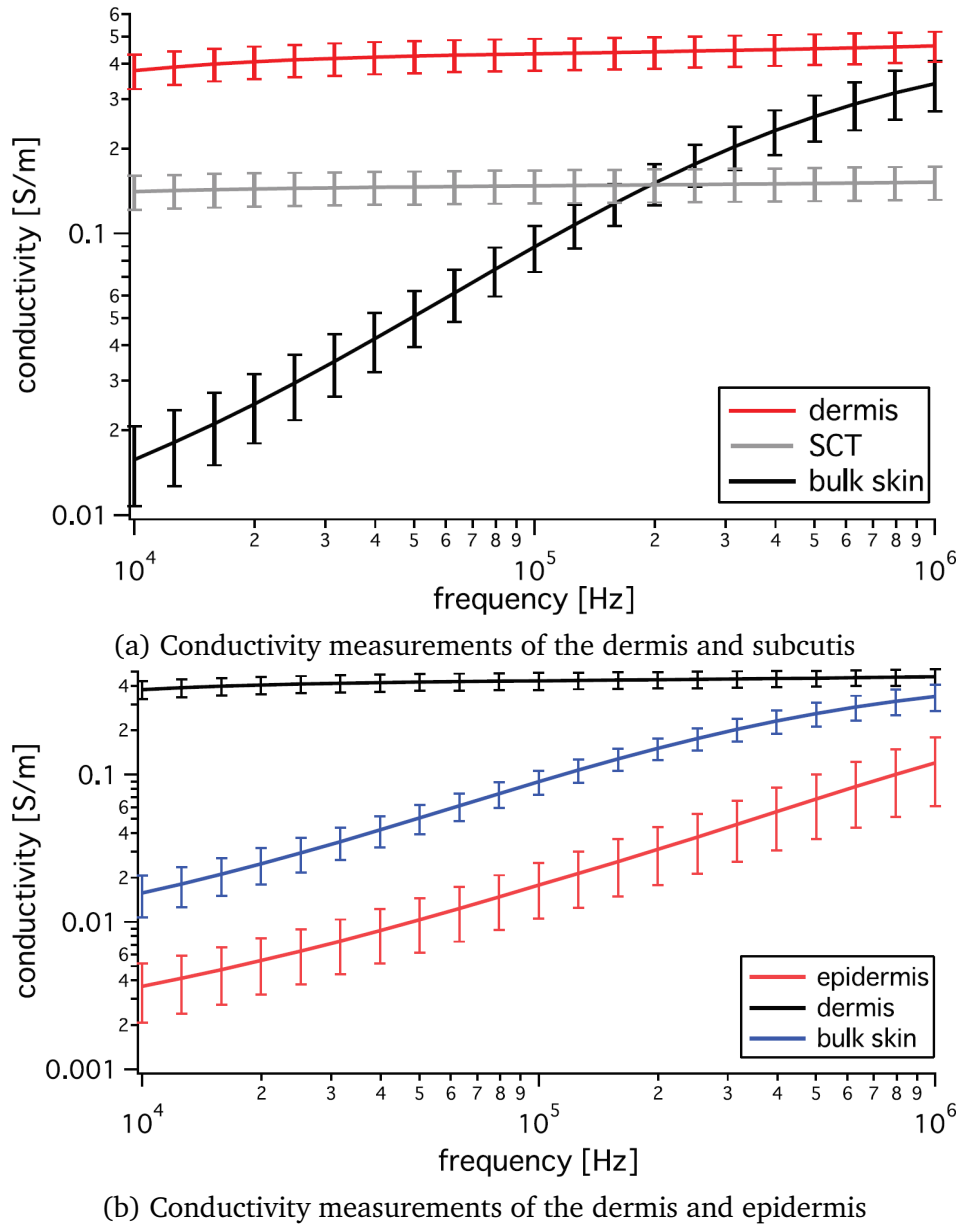


Figure I.4: Frequency dependence of the conductivity of the three main skin layers (from [20])

## I.2.4 Perturbating effects

### I.2.4.1 Change of charge carriers distribution over time

Because living tissues are electrolytic solutions, ions are free to move in solution in response to gradients of electric charges and concentration gradients. If a constant potential difference is applied between two points of the skin, positive ions will tend to migrate towards the negative potential, and vice-versa. Accumulated together, these ions will represent non-negligible electric charges and will offset any voltage measurement in their vicinity [9, 24].

### I.2.4.2 Dispersion phenomenon

In Section I.2.3.1, it was noted that, at high frequencies, living tissues underwent a significant decrease in relative permittivity, which could not be entirely explained by current penetration in the cells. This change is actually caused by a phenomenon called dielectric dispersion, which is a common occurrence in complex heterogeneous dielectric materials [25].

Dielectric dispersion occurs when the frequency of alternating currents becomes too high for the dipoles making up the material to have time to rotate and change polarity at the same frequency as the oscillations of the currents. Once the inertia of a type of dipole cannot be overcome in the time it takes for the current to change signs, the material loses its dielectric properties linked to this dipole, and its effective permittivity decreases.

Conductivity in heterogeneous materials can also be affected by frequency, as charge carriers become less likely to be trapped at interfaces when frequency increases. Indeed, when the direction of the current reverses more often, the distance traveled by charge carriers decreases [25].

Several types of dipoles provide dielectric characteristics to human tissues. First, ions of opposite charges can separate under the action of electric fields, forming macro-dipoles. Then, some charged proteins, amino acids, or other macromolecules can act as dipoles. Finally, water, which is a main component of tissues, is also famously a dipolar molecule. The typical evolution of electrical properties of living tissues because of dispersion is shown in Figure I.5.

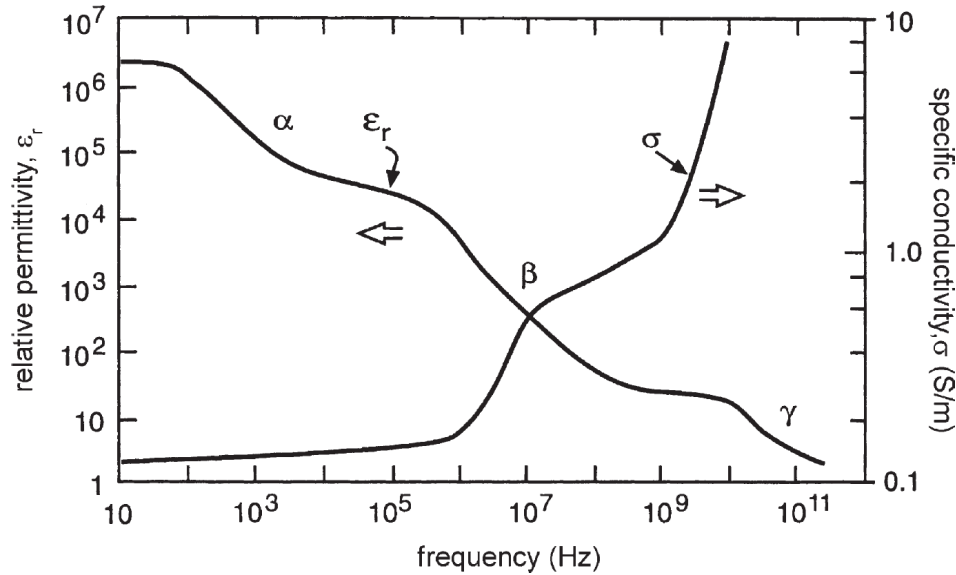


Figure I.5: Typical frequency dependence of the conductivity and permittivity of biological tissues (from [25])

The first dispersion observed in human tissues is the  $\alpha$  dispersion, generally below 1 to 10 kHz. It mostly affects the material permittivity and is attributed to the depolarization of the macro-dipoles formed by ions of opposite charges [8].

The next dispersion is the  $\beta$  dispersion, at around 10 MHz. This dispersion is caused on the one hand by depolarization of proteins and other macromolecules, but is also in large part attributed to current penetration inside of the cells when the capacitive impedance of the cell membranes becomes negligible and allows currents to pass through (Section I.2.2).

Finally, the  $\gamma$  dispersion, appearing in the GHz range, is due to the depolarization of water molecules [16].

The concept of dielectric dispersion allows us to fully explain the changes in conductivity and permittivity observed in human skin at high frequencies (Section I.2.3). It is very important to keep in mind as a confounding variable when observing impedance changes at high frequencies. Thankfully, human skin appears to be mostly unaffected by this phenomenon below 10 to 100 kHz, which allows lower frequencies to be analyzed at face value.

#### I.2.4.3 Galvanic skin response

The galvanic skin response (GSR) refers to measurable changes in skin conductivity as a result of variations in an individual's emotional state [9]. In response to a scary, stressful, or joyful environment, the activity of sweat glands situated in the dermis can increase through the action of the sympathetic nervous system [26]. Sweat will increase the moisture contents of the skin, thereby increasing its conductivity, as explained in Section I.2.3. It is therefore important to ensure that measurements are

performed when subjects are relaxed, which is a prospect that can be offered by the long-term application aimed by the Vitapatch project.

### I.3 Impacts of a wound on the electrical properties of the skin

In medical terms, an open wound is an injury involving damage to external, and potentially internal, bodily tissue. All open wounds are associated with damage, tears, or ruptures of the epidermis, although more severe wounds can reach the dermis and even underlying tissues and organs.

As mentioned in the [introduction](#), the aim of the Vitapatch project is to provide a means of monitoring chronic wounds. Chronic wounds are characterized by an abnormally slow or absent healing process, and encounter issues related to bacterial infection or necrotic tissues [\[1\]](#). Most types of chronic wounds are ulcers, which are defined as breaks or discontinuities in the skin. Ulcers generally result in a loss of the epidermis, and more severe conditions can affect the dermis and even the subcutis as well.

Knowing the electrical characteristics of each skin layer and what they are linked to physiologically, it is possible to predict the changes that would be caused by wounds and ulcers.

The first effect to consider is an increase in conductivity at the location of the wound, which would translate into a decreased measured electrical resistance. Indeed, it was established in [Section I.2.3.2](#) that the stratum corneum constitutes a barrier of low conductivity at the surface of the skin. As even the most benign wounds will result in a degradation of this layer at the injury site, the skin resistance across a wound can be expected to drop significantly. The same is true for the loss of the rest of the epidermis, to a lesser extent.

In addition to resistance changes, the capacitive and frequency-dependent properties of the skin can also be expected to change due to a wound. As a reminder, the frequency dependence of skin properties is once again largely brought by the epidermis. With shallow to moderate wounds affecting the epidermis, the change in measured impedance as a function of frequency is also expected to decrease.

Some sources [\[27, 28\]](#) also suggest that the change in capacitive properties of the skin around a wound may not be confined to the injury site itself. Indeed, in [Section I.2.2](#), cell membranes were described as an important component in the frequency dependence of conductivity and permittivity through their capacitor-like configuration. As the trauma of a wound affects the surrounding tissues, neighboring cells may undergo physiological changes due to limited nutrient supply, increased immune response, and inflammation, ... A possible result is a general decrease in cell population density on a larger spatial scale than the wound itself. This decrease would cause a reduction in capacitive elements in the tissues, and an additional decrease in reactance around the wound would be expected as a consequence.

Experimental measurements of skin impedance on and around a wound are available in different scientific publications. Figures I.6 to I.8 show impedance spectroscopy measurements of wounds from different severities of wounds and experimental setups.

Figure I.6 gives the resistance  $R$ , reactance  $X$ , and phase angle of a large leg ulcer measured via a four-point measurement (see Section II.1.1) on either side of a large pressure ulcer. Impedance measurement was performed with a 50 kHz, 800  $\mu$ A current. The phase angle is defined as  $\tan(\frac{X}{R})$ , and is a summary of both resistance and reactance measurements, giving another indication of cell vitality.

Figure I.7 gives fitted impedance spectra of different types of damaged tissues acquired using an LCR meter applying a constant 100 mV RMS voltage between 100 Hz and 1 MHz, instead of injecting a constant current.

Finally, Figure I.8 compares the impedance magnitude spectra of wounded and healthy portions of the skin using two-point measurements on the wound and a neighboring unwounded area. The impedance spectrum was performed by applying alternating currents between 10 Hz and 10 kHz.

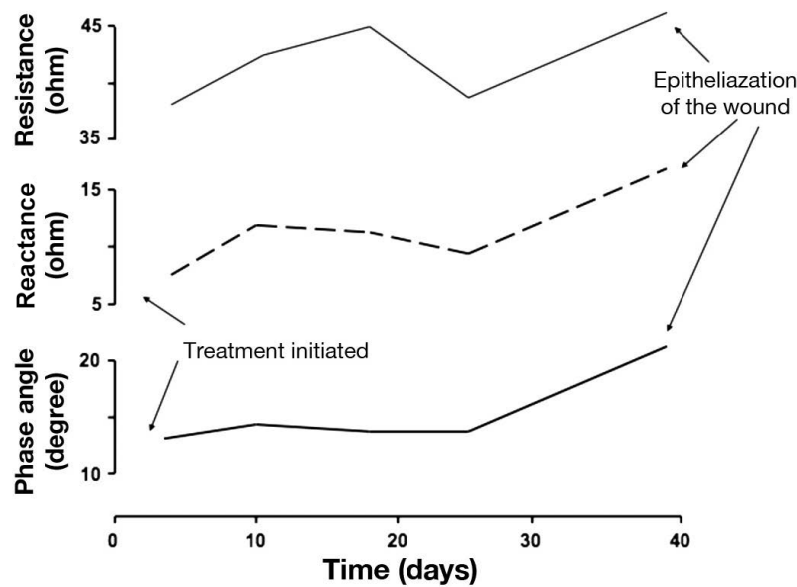


Figure I.6: Evolution of skin resistance, reactance, and phase angle around a large pressure ulcer at 50 kHz during healing, from four-point measurements (from [27], with corrected axis labels)



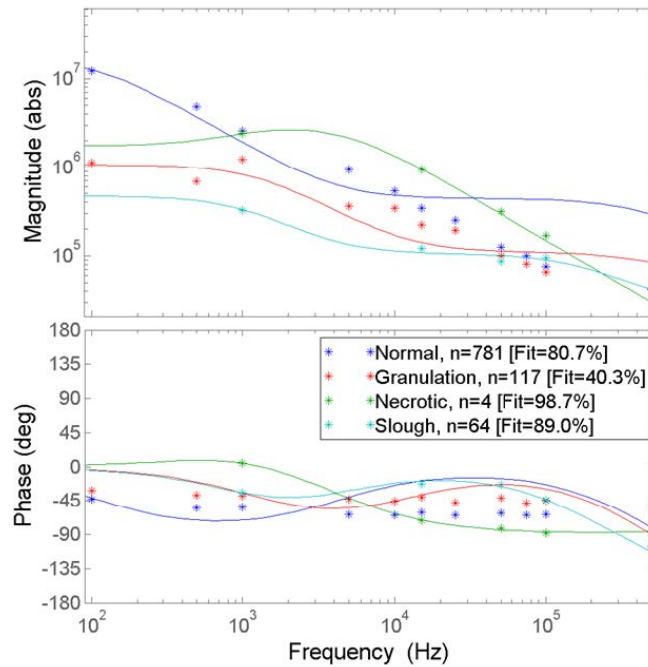


Figure I.7: Fitted magnitude and phase spectra of wounded tissues at different stages of healing (from [28])

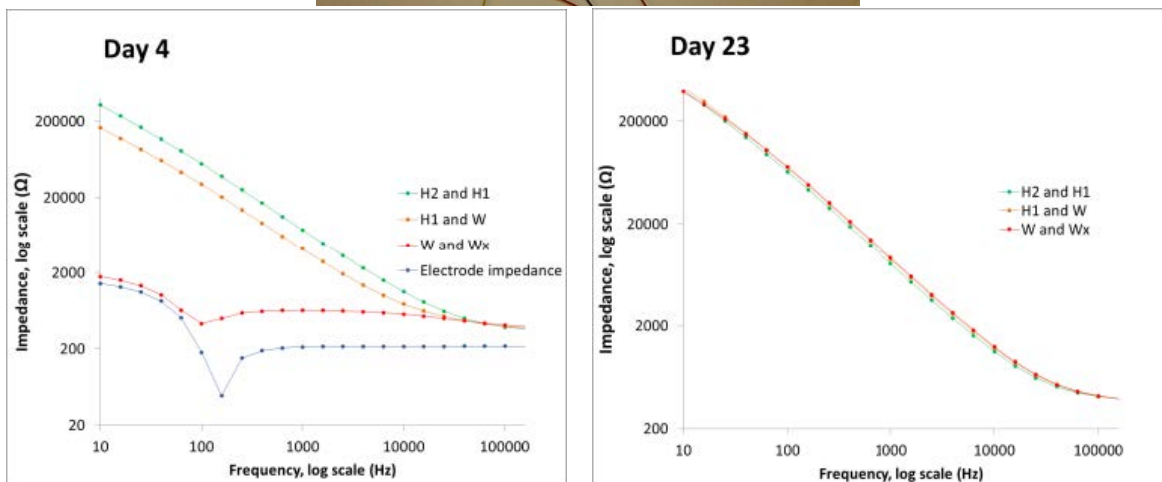
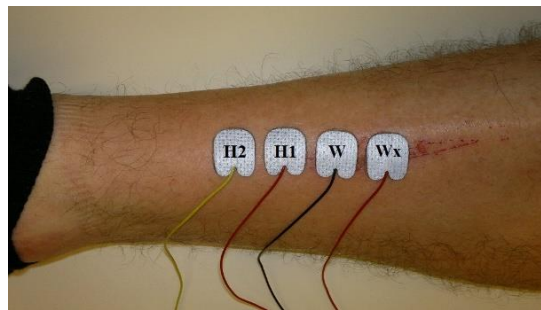


Figure I.8: Magnitude impedance spectra of healthy and superficially wounded skin before and after healing from two-point measurements (from [5])

These different publications all come to the same conclusion. As anticipated, a wounded portion of skin displays lower resistance and capacitance than a healthy one when measured non-invasively. Because these results are impedance measurements, they are difficult to compare quantitatively. Indeed, electrode contact impedance, measurement methodology, wound size, and severity all vary significantly between publications. The qualitative changes in skin impedance around a wound are nevertheless consistent between publications, and with theoretical expectations based on the properties of skin layers.

Interestingly, none of these experimental measurements are performed above 1 MHz. Going back to the results of Section I.2, limiting the exploration of skin impedance up to the 100 kHz - 1 MHz range indeed seems reasonable for wound assessment. On the one hand, low-frequency measurements, below 10 to 100 kHz are best suited to measure changes in conductivity and resistance between healthy and wounded epidermis. Increasing the frequency helps evaluate the frequency dependence of skin conductivity, which is a characteristic present in the healthy epidermis. Above 1 MHz, dielectric dispersion has led to the increase in epidermis conductivity, to the point where it does not represent a significant current barrier anymore, and currents are able to penetrate the skin down to the dermis and subcutis regardless of epidermal damage.

The permittivity of dry skin is also almost constant below 1 MHz, which facilitates the assessment of cell vitality through reactance measurements.

## Part II

# Bioimpedance measurements

Impedance measurement, or impedance spectroscopy, is probably one of the most common types of measurement in electrical engineering. As such, it is also a diverse field, with a wide variety of existing techniques and procedures.

The Vitapatch project aims at using bioimpedance measurements, or measurements of the impedance of biological tissues. This category of measurements presents several challenges. First, as discussed in Part I, the human skin is a complex material in terms of electrical properties, which complicates the analysis of its impedance spectrum compared to simple passive electrical components. Second, the context of the measurement, on a living, human being, imposes a non-negligible set of constraints on the measurement method, such as a safe current limit and the use of non-invasive electrodes. Last but not least, the objective of this project is to create a highly portable and long-lasting measurement device, which leads to the use of ultra-low-power solutions for the measurements.

In this second part, the constraints and technicalities of bioimpedance measurements are explored. Accordingly, medical device safety regulations and prospective research on suitable electrodes for the Vitapatch project are presented. Finally, state-of-the-art methods for wound assessment via bioimpedance measurements are also reviewed.

## II.1 Bioimpedance measurement setup

### II.1.1 Impedance measurement methodology

From the definition of electrical impedance, it appears obvious that to measure the impedance between two points of material, information about the current flowing between these two points and the voltage difference between them is required. This infers that one can either apply a known voltage between two points and measure the resulting current, or inject a known current and measure the resulting voltage.

These two approaches are easy to perform using voltmeters or ammeters, and current or voltage sources.

As discussed earlier, when dealing with complex impedances, it is necessary to gather information about its behavior at different frequencies. Hence, to perform impedance spectroscopy, applying a current or voltage at a single frequency is not sufficient. Suitable excitation signals and post-processing methods for impedance spectroscopy will be presented later, in Part III.

For the following, assume that a known current is injected into the impedance to be measured (the Sample Under Test (*SUT*)). To compute the value of the impedance, the voltage between either side of the SUT needs to be measured. Naively, one might proceed as in Figure II.1a, by measuring the voltage difference between both current injection leads. This is referred to as a two-point impedance measurement.

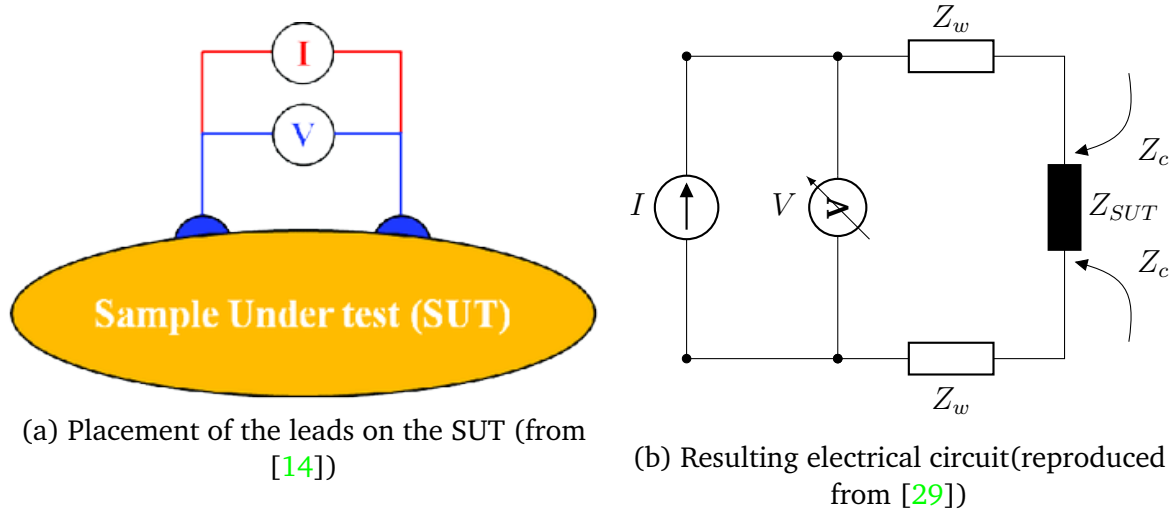


Figure II.1: Two-point impedance measurements

In many traditional cases, this is perfectly acceptable. However, this method introduces some errors that can be significant in certain cases. Indeed, the resulting circuit is the one represented in Figure II.1b. In this circuit, the impedance of the wires ( $Z_w$ ) as well as the contact impedance ( $Z_c$ ) between the leads and the SUT are considered. Strictly speaking, the measured impedance is thus given by

$$Z_{meas} = \frac{V}{I} = Z_{SUT} + 2Z_w + 2Z_c$$

This can be an issue when the wire or contact impedances are not negligible compared to the impedance of the SUT, or when they are susceptible to variations. In the case of a bioimpedance measurement, this is generally the case. Indeed, as discussed in Section I.2.3, the contact impedance between electrodes placed on the skin and the tissues of interest will very often exceed the impedance of the tissues themselves, because of the large resistivity of the stratum corneum. Moreover, the presence of

hair or sweat can make contact impedance unpredictable and variable over time. Therefore, another strategy needs to be considered for good measurements.

Instead of using the same leads to inject a current and measure the resulting voltage, four-point impedance measurements uses a pair of leads to inject a current in the SUT, and a different pair to measure the resulting voltage, as shown in Figure II.2a.

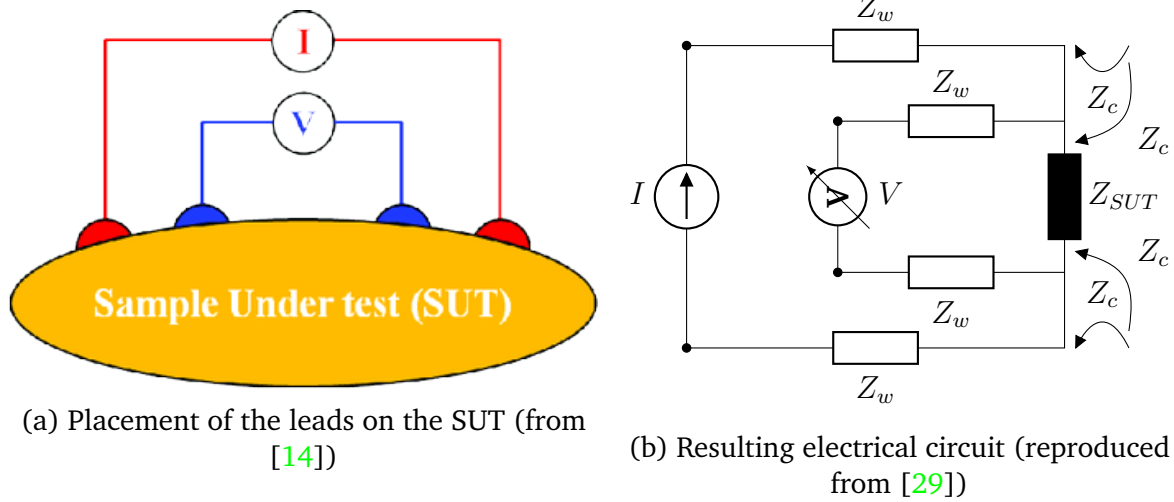


Figure II.2: Four-point impedance measurements

The resulting circuit is represented in Figure II.2b. Four-impedance measurements are capable of overcoming the parasitic wire and contact impedances thanks to a reasonable assumption: the voltage measurement device is assumed to have an infinite input impedance, which means that no current is flowing inside of the voltage measurement loop. This assumption is reasonable when the input impedance of the voltage measurement device is far greater than the rest of the impedances of the circuit, which, in our case, will be ensured by the use of an instrumentation amplifier, as discussed in Section III.1.3.2. Because of the absence of currents flowing into the contact and wire impedances present on either side of the voltage measurement device, the only voltage drop to measure is caused by the current  $I$  flowing into the SUT. Therefore, the measured impedance in that case is

$$Z_{meas} = \frac{V}{I} = Z_{SUT}$$

Hence, four-point measurements are generally preferred when measuring bioimpedances using non-invasive electrodes, because it allows for the impact of contact impedance on the measurement to be canceled.

### II.1.2 Non-invasive impedance measurement modeling

To simulate bioimpedance measurements and give meaning to experimental results, it can be useful to have simple electrical models for measurements performed on living

skin. For this, two popular models and easily implemented models are presented.

### II.1.2.1 The Cole model

The Cole model [30] is a simple electrical model widely used in the field of bioelectronics to represent current injection in the skin [31]. This model aims at fitting the experimental measurement data well, without necessarily representing the physical reality accurately. More precisely, this model does not take into account the different layers of the skin, assuming instead that the sample under test is a single lumped material [32], whose properties are mostly reminiscent of the stratum corneum since most of the current does not reach the inner layers of the skin in normal conditions.

The Cole model considers the skin as a dielectric material susceptible to dielectric dispersion. To represent conductivity changes as a function of frequency, caused by current penetration in the cell, this model defines two resistances: the low-frequency resistance  $R_0$  and the high-frequency resistance  $R_\infty$  [31]. These resistances correspond to empirical measurements at very low and very high frequencies and naturally depend on the measurement setup, such as the distance between electrodes. For the transition between these two frequency ranges, a special type of capacitive element, called Constant Phase Element (*CPE*), is also included in the model. This type of element is generally used to represent non-ideal capacitors in electrochemical systems [33], where capacitance can decrease when the frequency increases, because of dielectric dispersion.

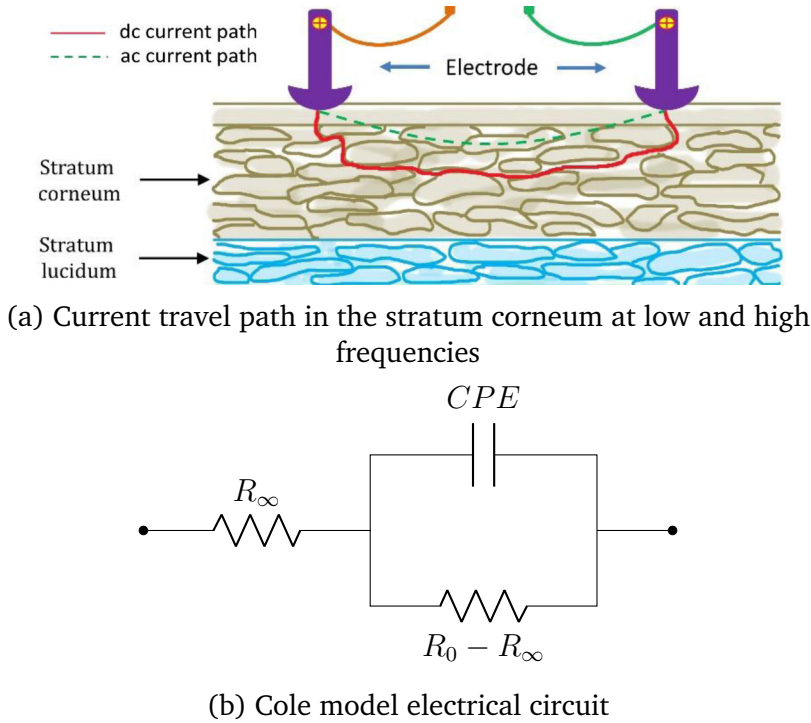


Figure II.3: Cole bioimpedance model (from [31])

The Cole bioimpedance model is represented in Figure II.3, and the mathematical expression of the impedance is given by (II.1).

$$Z_{\text{Cole}} = R_{\infty} + \frac{R_0 - R_{\infty}}{(1 + j\omega\tau)^{\alpha}} \quad (\text{II.1})$$

with the relaxation time

$$\tau = [(R_0 - R_{\infty}) C]^{\frac{1}{\alpha}}$$

This expression neatly summarizes all the behaviors modeled by the Cole model. When  $\alpha = 1$ , the CPE behaves like an ideal capacitor of capacitance  $C$ , and the model is reduced to an R - R//C dipole. At low frequencies ( $\omega \rightarrow 0$ ),  $Z_{\text{Cole}} \rightarrow R_0$ , and at high frequencies ( $\omega \rightarrow \infty$ ),  $Z_{\text{Cole}} \rightarrow R_{\infty}$ , as the CPE is shorted or shorting its parallel resistance depending on the frequency.

A value of  $\alpha \in ]0, 1[$  is used to add imperfections to the CPE. At the extreme, when  $\alpha = 0$ ,  $Z_{\text{Cole}} = R_0$ , expressing that the dielectric material is never polarized, and is actually not a dielectric material at all. Generally, the value of  $\alpha$  is set around 0.8 to describe the relaxation of ionic macro-dipoles, which makes this model most suitable for use to model current injection below 500 kHz [32].

### II.1.2.2 Electrode contact models

The Cole model is a useful and straightforward model that is generally sufficient to express the frequency dependence of skin impedance and analyze bioimpedance measurement results. However, an important part of the measurement system is omitted : the interface between the body and the measurement circuits, in the form of non-invasive electrodes. Here, traditional conductive electrodes, making direct contact with the skin, are considered (see Section II.2.2.2 for more details).

As already mentioned in Section I.2.1, current conduction in tissues occurs thanks to the motion of ions, as opposed to the one of electrons in traditional analog electrical circuits. At the interface between the electrolytic tissues and the metallic electrodes, a transfer of charge between the electrons of the electrode and the ions of the tissues therefore has to occur. When currents cross the electrode-electrolyte interface, anions flow in the same direction as the electrons, while cations move in the opposite direction, as illustrated in Figure II.4. This means that, in general, one type of charge will accumulate along the electrode-electrolyte interface, causing an electric potential, called the half-cell potential, to appear. When a current is injected between two electrodes, negative charges will accumulate at one electrode, while positive charges will gather near the other. This will lead to a DC voltage difference between the electrodes, which has to be accounted for when making measurements at the surface of the skin.

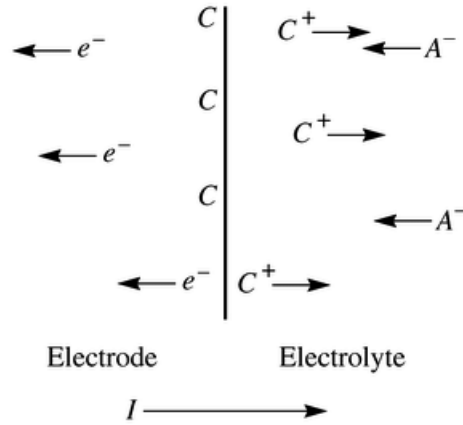


Figure II.4: Illustration of charge carrier motion at an electrode-electrolyte interface (from [34])

Figure II.5 showcases two electrical models that take the electrode-electrolyte interface into account [34]. On the left, the simplest model of the two uses an R - R//C dipole similar to the Cole model to represent the impedance of the skin. The interpretation of both resistances  $R_p$  and  $R_s$  are a bit different, as the former represents the resistance of the epidermis while the latter models the resistance of the dermis and underlying tissues. A capacitor  $C_p$  is placed in parallel with  $R_p$  to model the frequency dependence of the epidermal impedance established in Section 1.2.3.2, while the dermis and deeper layers are modeled as purely resistive. The half-cell potential is represented by a DC voltage  $E_{hc}$ , which generally takes values of around 300 mV with typical Ag/AgCl electrodes. Additionally, an alternating noise source  $v_{\text{noise}}$  is used to take into account noises such as the thermal noise generated by the electrode-skin contact resistance, which is relevant above 100 Hz.

On the right, a more complex model is considered, which sees the sweat or conductive gel used in some types of electrodes as an intermediary electrolyte, where charge transfer also takes place. The resistance of that electrolyte  $R_s$  is modeled, and the electrode is considered to have some capacitance and resistance, as is generally the case in practice. Values of  $R_d$  are usually around 50 k $\Omega$ , while  $C_d$  is generally considered to be around 50 nF. Note that both epidermal and electrode capacitances are modeled with CPEs, like in the Cole model.



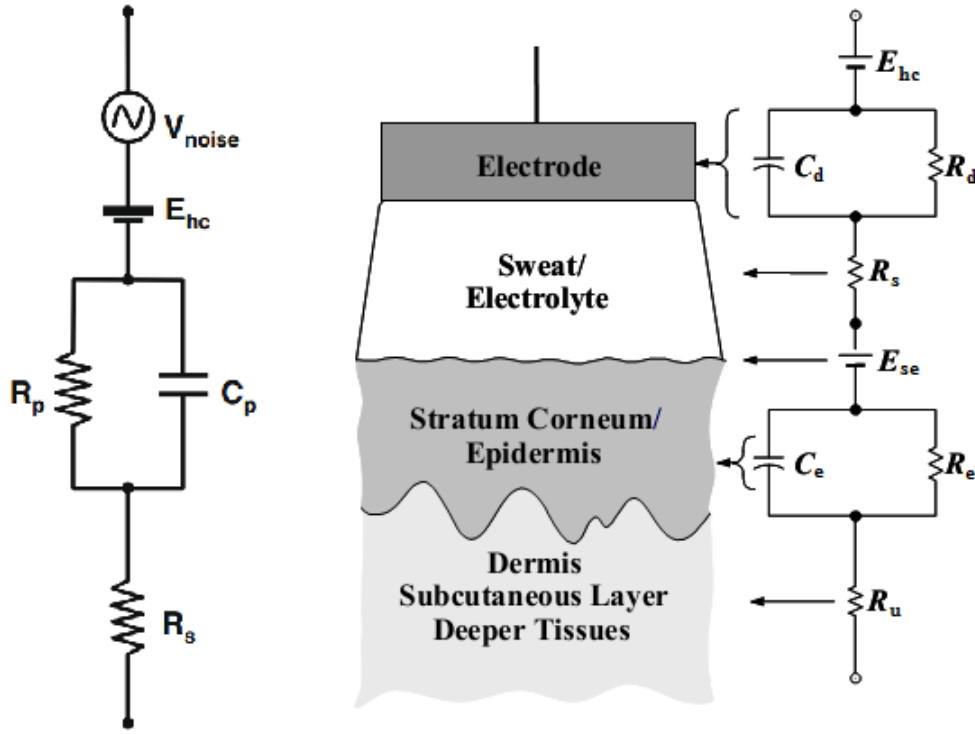


Figure II.5: Electrical models of the electrode-electrolyte interfaces at the surface of the skin (from [34])

These models will be useful later to model realistic loads for the bioimpedance measurement circuits and assess their ability to reject contact impedances and DC half-cell potentials.

### II.1.3 Electrical safety and medical standards

To perform impedance measurements on human tissues, several safety measures and medical standards have to be respected.

#### II.1.3.1 Patient auxiliary current limits

The most obvious precaution to be taken in our case concerns the current injection into the body. The most well-known danger to any material subjected to a current flow is Joule heating, caused by energy losses of moving charge carriers in a conductive material. The power dissipated by the Joule effect in a resistance  $R$  is given by  $P = RI^2$ , where  $I$  is the root-mean-square (RMS) current flowing through the resistance. Because living tissue conductivity is very low compared to a traditional conductor (metals have conductivities in the  $10^7$  S/m range), the resistance  $R$  is expected to be high, and even small currents will cause a significant tissue heating.

Capacitive heating, which refers to losses in dielectric materials due to the rotations

of dipoles, can be a concern at very high frequencies, typically in the microwave frequency range and above (starting at 1 GHz), and will therefore be ignored here.

Besides its amplitude or RMS value, the frequency of an injected current in the body also affects its effect on tissues. Indeed, lower frequency currents are considered to be more harmful than higher frequency ones due to their greater impact on charge carrier distribution. Because living tissues are electrolytic materials where currents travel through ionic movements, a continuous current or electric field is the worst-case scenario for safety. In that case, positive and negative ions can separate and accumulate near each injection electrode, completely changing the local electrical potentials and ion concentration gradients of the extracellular medium. Because many physiological processes at the cell level depend on a chemical and electrical balance between intracellular and extracellular ions, such a disruption, if lasting long enough, could have dramatic consequences, from the unexpected release of compounds to cell death.

Additionally, currents and ion movements can lead to electric stimulation of nerves and muscles, causing a variety of effects from slight discomfort, twitching or electrically induced spasms. [35]

As currents evolve from direct to alternating, the behavior of charge carriers changes: instead of migrating towards a point, ions will oscillate in space, following the oscillations of the electric field. The higher the frequency, the more often the direction of the currents changes, and the smaller distances the ions travel [32]. Hence, higher frequency currents are generally deemed safer for living tissues.

The IEC 60601-1-11:2015 [36] ISO standard defines "*the current that normally flows between parts of the applied device through the patient, which is not intended to produce a physiological effect*" as Patient Auxiliary Current (PAC). The PAC limits as a function of frequency according to this standard are given in Table II.1.

Current frequency $f$	0.1 Hz to 1 kHz	1 kHz to 100 kHz	above 100 kHz
Current limit	100 $\mu\text{A}$	100 $f$ $\mu\text{A}$	10 mA

Table II.1: Patient auxiliary current limits as a function of frequency according to the IEC 60601-1-11:2015 ISO standard (from [37])

### II.1.3.2 Biocompatibility criteria

Biocompatibility is a slightly ambiguous notion, that refers to the ability of a biomaterial to perform its function without adversely interacting with living media. Biomaterials are all materials used in a medical device that are put in contact with biological systems and tissues. The definition of biocompatibility is broad and vague, and biomaterial performances are generally assessed in the context of a specific application.

For the Vitapatch project, the main biocompatibility challenge concerns the use of skin electrodes for long-term wound monitoring. For long-term applications, placement of electrodes directly on the wound is strictly out of the question, as risks of an

immune response or infectious bacterial buildup are too great. Degradation of the electrode material under the action of exposed body fluids is also a concern, and so is leaching of particles making up the electrodes.

Moreover, placing electrodes directly on the wound would defeat the purpose of the project, which is to create a non-invasive device that would still allow access to the wound for treatments.

Electrodes placed around a wound, on undamaged skin, still have to meet some criteria to be biocompatible in the long term. The materials should be as inert as possible, should not be oxidized or degraded by sweat, and should not cause skin irritation, inflammation, or abrasions. Suitable electrode types and materials will be presented in Section II.2.2.3.

## II.2 Impedance measurements of skin and tissues

### II.2.1 Biological potentials and contact variables

A variety of parameters that can affect skin-electrode electrical contact and the resulting measurements have already been mentioned so far. These include

- The integrity and thickness of the stratum corneum and other epidermal layers
- The humidity of the skin, possibly affected by sweat gland activity
- The half-cell potential appearing at the electrode-electrolyte interfaces with tissues

Along with these effects, one can also mention the impact of hairs between the electrodes and the skin, depending on the application location and the patient. Hair will limit the contact area between the electrodes and the skin, possibly increasing the contact resistance further.

Some other sources of electric noises coming from the body can be considered as well. After all, electrodes are frequently used to record signals in applications such as electrocardiography, electromyography, and electroencephalography, ... Movements, muscle contractions, and heartbeats, ... are therefore all potential sources of noise, as action potentials travel across the body and briefly modify local potential distributions. Thankfully, the frequency range of such biopotentials is generally well defined, and the apparition of noise at certain frequencies can easily be attributed to these phenomena and filtered out if need be.

### II.2.2 Investigation of suitable electrodes for long-term applications

In the medical domain and the literature, there exists a wide variety of electrode types for non-invasive measurements of biological potentials and bioimpedance. However,

for the Vitapatch project, the choice of a specific family of electrodes needs to be considered, as the aims of the project require specific properties.

### II.2.2.1 Required electrode specifications

- First and foremost, the electrodes used should support the injection of a current into the human body, as opposed to simply being able to sense electrical potentials.
- To limit the power consumption of current sources and maximize the battery life of the device, the contact impedance between the electrodes and the skin should not be too high. Indeed, the injected currents will need to go through these impedances as well as through the skin, which requires some additional power.
- The electrodes should be suitable for long-term applications. This means that
  - The materials of the electrodes should be biocompatible: they should not cause any irritation or discomfort, chemical compounds should not leak into the skin, they should be as inert as possible, and they should not promote inflammation or bacterial growth.
  - The electrodes should be able to remain in place and maintain contact for several days or weeks to avoid movement artifacts.
  - The contact between the skin and the electrodes should not degrade over time. If the contact impedance changes in the long term, measurement drift will occur and results could be skewed.

### II.2.2.2 Electrode classification

Electrodes dedicated to medical applications can be classified into different families depending on their operating principles. Identifying the properties of these different families is useful for selecting the right type of electrodes for this project.

**a) Conductive and capacitive electrodes** The first distinction between families of electrodes can be made based on the way an electrical connection is established with the skin. The most common modality is through direct contact with the skin. These electrodes are made of metallic materials, and a conductive gel is eventually added for better contact with the skin.

Alternatively, an electrical connection between the skin and the electrodes can be established without any direct physical contact. This is the principle of operation of capacitive electrodes. These consist of a conductive plate separated from the skin by a dielectric material [38]. Considering the human skin as a conductive material, this arrangement creates a parallel plate capacitor, which can conduct alternating currents. A schematic of capacitive electrodes is presented in Figure II.6.

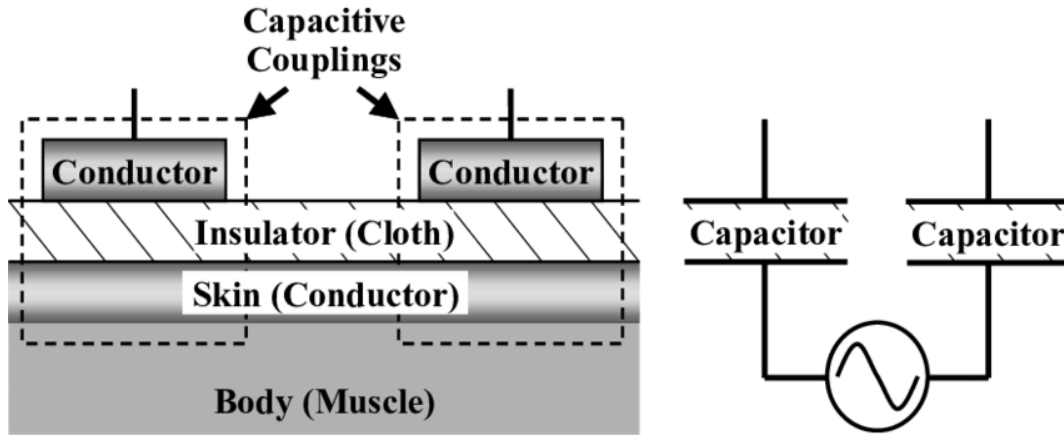


Figure II.6: Principle of operation of capacitive electrodes (from [38])

Capacitive electrodes appear as a promising alternative to their traditional conductive counterpart, especially for wound imaging, as they could enable long-term, contactless measurements with electrodes placed directly over a wound without any risk of galvanic corrosion or other reaction between metals and body fluids.

However, capacitive measurements present a few drawbacks that would make them unpractical in the framework of this project.

First, a mainly capacitive contact impedance implies that current injection at lower frequencies could be compromised. Indeed, a capacitive impedance  $Z_C$  is an inverse function of frequency  $f$

$$Z_C = \frac{1}{2\pi fC}$$

In Part I, it was established that low-frequency components of skin impedance were an important factor in determining the status of a wound. It would therefore be ill-advised to compromise the measurement of the low-frequency part of the impedance spectrum, as it would impoverish the resulting data.

Second, as will be discussed in Part V, image reconstruction algorithms that will be used in this project are incompatible with capacitive electrodes. Indeed, these algorithms rely on boundary conditions for current injection, that are easily defined with contact electrodes. Capacitive coupling between conductors is more unpredictable, as the area of the skin defining the second plate of each capacitive electrode cannot be easily assumed.

Depending on the physical design of the electrode patch, capacitive electrodes could also be much more sensitive to motion artifacts [39], as they do not remain physically attached to the same part of the skin at all times and could be free to move relative to the wound.

Finally, capacitive measurements are not as easy to perform as conductive ones, as they require the use of special circuits like charge amplifiers to obtain good measurements.

For these reasons, as well as the added complexity in creating an experimental

setup using capacitive electrodes, they will not be considered in this project, although they remain an interesting prospect.

**b) Wet and dry electrodes** As mentioned above, contact electrodes can be further separated into two categories: wet and dry electrodes [40].

For instantaneous or short-term measurements, wet electrodes are widely used in the medical field. These electrodes use a conductive gel to greatly improve contact between the skin and the electrodes, filling any gaps. Moreover, when coupled with light skin abrasion and cleaning, gels can mitigate the impact of dead skin, oils, grease, and hair over the measurement period.

Ag/AgCl electrodes coupled with a gel are the most widely used type of external electrodes in the medical field, as they have the lowest contact impedance of any type of electrodes (typically in the  $k\Omega$  range). Some studies also suggest that, coupled with the right conductive gel, they can be used for bioimpedance spectroscopy and tomography over longer periods of a few hours [40].

The major downsides [39, 40, 41] of such electrodes for long-term monitoring are that

- their contact impedance increases over time, as the gel dries out and,
- they are not biocompatible for long periods, as they cause skin irritation and discomfort.

Dry electrodes, as opposed to wet ones, do not rely on the use of gel as an intermediate between the conducting material and the skin. Capacitive electrodes are de facto dry electrodes, but this section will only focus on conductive electrodes. Due to their application method, dry electrodes should be somewhat flexible to conform to the skin, and the materials used should be biocompatible because of the direct contact. Traditionally, dry electrodes are therefore made of thin metallic films or conductive polymers (intrinsic or composite) [41].

One obvious disadvantage of dry electrodes, which limits their usage to certain use cases in the medical field, is their higher contact impedance due to the absence of conductive gel to increase the contact surface. Generally, polymer electrodes have a contact impedance of 1 or 2 orders of magnitude higher than wet electrodes. Different sources report different metrics, but some mention impedances up to the  $M\Omega$  range [41].

On the other hand, it is possible to take advantage of their direct contact with the skin to create viable solutions for long-term applications. Indeed, the use of the right materials can give the electrodes flexibility, biocompatibility, and skin adhesivity. Generally, such electrodes will not be made of metal films, as they are not stretchable nor adhesive. Intrinsically conductive polymers are a solution to obtain flexible and stretchable electrodes, but they are not usually adhesive to the skin. The last possibility is composite polymers, which can be made as a perfect mix of all these properties, at the cost of a higher contact impedance as the conductive nanofillers will be a minority within the polymer matrix.

### II.2.2.3 Selection of plausible solutions

After some literature research, some novel types of dry electrodes emerged as plausible candidates to be used in the Vitapatch project. Two different examples are presented here: one is a gold-based electrode manufactured directly on physiological tape, and the other is a conductive polymer film.

In “Assessment of Dry Epidermal Electrodes for Long-Term Electromyography Measurements” [41], the authors present thin and flexible gold electrodes embedded into a medical-grade tape. These electrodes are manufactured by depositing gold foil onto a PET substrate, for minimal gold usage and ease of manufacturing of complex shapes. Gold is a good conductor and regarded as biocompatible and corrosion-resistant for prolonged periods of time, which makes this system well-suited for long-term measurements.

Such integration of electrodes into medical tape is very interesting for the Vitapatch project, as it could lead to a very natural solution in the clinical field, well-suited for use around wounds. The authors also mention that the tape would guarantee consistent contact between the electrodes and the skin while remaining flexible and supporting skin health. According to the results of this article, this kind of electrodes display comparable signal quality and signal-to-noise ratio as Ag/AgCl electrodes for electromyography applications.

Figure II.7 shows an example of these electrodes manufactured into a commercially available physiological tape.



Figure II.7: Gold electrodes on a PET substrate embedded into medical tape (from [41])

In “Fully organic compliant dry electrodes self-adhesive to skin for long-term motion-robust epidermal biopotential monitoring” [39], an even more novel solution is presented. The authors managed to fabricate biocompatible, self-adhesive, and stretchable dry electrodes with high conductivity by blending several polymers together :

- PEDOT:PSS, an intrinsically conductive polymer that provides high effective contact area, high conductivity biocompatibility and flexibility,



- Waterborne polyurethane, which improves stretchability and skin conformation, and
- D-sorbitol, that further improves stretchability and provides adhesiveness to the skin.

These electrodes can be produced by pouring a solution into molds of any desired shape, and take the form of thin adhesive films that can be interfaced with a piece of copper sheet. The authors claim comparable or better performance in the long term than Ag/AgCl electrodes for EEG, ECG, and EMG measurements, with far less motion artifacts and, in some cases, a lower contact impedance. After 16 hours, the electrodes were still fully adhered to the skin of the test subjects and did not produce any irritation or discomfort.

This type of polymer film electrodes could conceivably be manufactured into an adhesive patch to be placed around a wound, and would certainly provide excellent motion artifact elimination and low contact impedance in a very slim and comfortable configuration, which is another interesting perspective for the Vitapatch project. Different shapes and illustrations of practical applications of these electrodes are shown in Figure II.8.

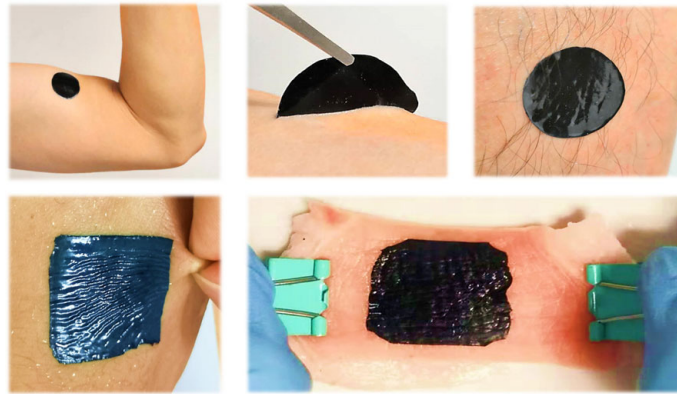


Figure II.8: Self-adhesive conductive polymer film electrodes (from [39])

### II.2.3 State-of-the-art wound assessment via bioimpedance spectroscopy

To conclude this part about bioimpedance spectroscopy, it is interesting to take a look at some existing methods for wound assessment via the measurement of bioimpedance and to discuss in what ways the Vitapatch project can improve on them.

The first and simplest wound assessment method via impedance measurement that can be of interest comes from “Bioelectrical Impedance Assessment of Wound Healing” [27]. In this article, the results of four-point impedance measurements performed from outside of a large pressure ulcer are presented. The measurement setup is illustrated in Figure II.9 The results of this article have already been presented in



Figure I.6: as the wound heals, the measured resistance, reactance, and phase angle increases, indicating re-epithelialization and increase in cell vitality around the wound.

This method seems perfectly suitable for long-term monitoring, as electrodes are placed outside of the wound and do not represent an obstacle or a biocompatibility concern. However, the data obtained with this method is very simple, with only three values summarizing the state of an entire ulcer. For chronic wound monitoring, a more comprehensive spatial assessment of wound status and healing is preferable, to potentially detect necrotic tissue, infection, or areas where healing is complicated.

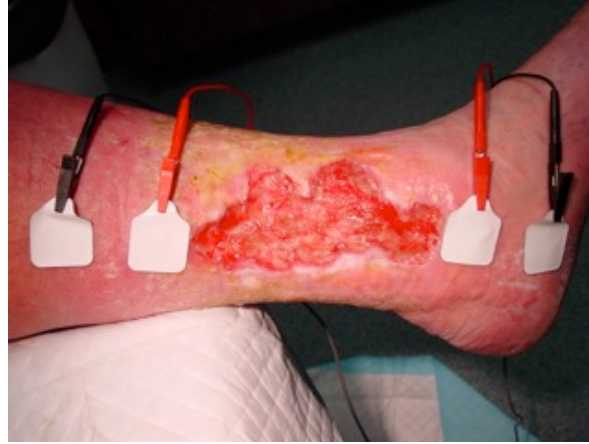


Figure II.9: Four-point bioimpedance measurement around a pressure ulcer (from [27])

A much more recent, state-of-the-art wound monitoring device is presented in “Bioimpedance method for monitoring venous ulcers: Clinical proof-of-concept study” [6]. It is the result of the evolution of the research of Kekonen et al. [5], already presented in Figure I.8. The measurement device, shown in Figure II.10a, consists of a flexible electrode array on a PET substrate placed directly on the wound for two-point impedance measurements between each electrode of the array and 4 reference electrodes on the edges of the patch. Impedance magnitude measurements are performed at 5 different frequencies between 150 Hz and 10 kHz, and a variable called *wound status parameter* is defined. To compute this parameter, impedance measurements between the reference electrodes (on healthy tissues) are performed at each frequency. The impedances measured at each wound electrode are normalized with regard to these reference measurements, and measurements at all frequencies are averaged for each electrode. The formula for this wound status parameter is given in (II.2), for clarity.

$$\text{Wound status parameter } (\%) = \left\{ \frac{\frac{Z(f_1)_W}{Z(f_1)_R} + \frac{Z(f_2)_W}{Z(f_2)_R} + \dots + \frac{Z(f_n)_W}{Z(f_n)_R}}{n} \right\} \times 100\% \quad (\text{II.2})$$

To create visual images of the wound, the values of the wound status parameter for each electrode are attributed to points in space corresponding to the electrode locations, and a 2D interpolation is performed. The results of this procedure for a small ulcer are shown in Figure II.10b.

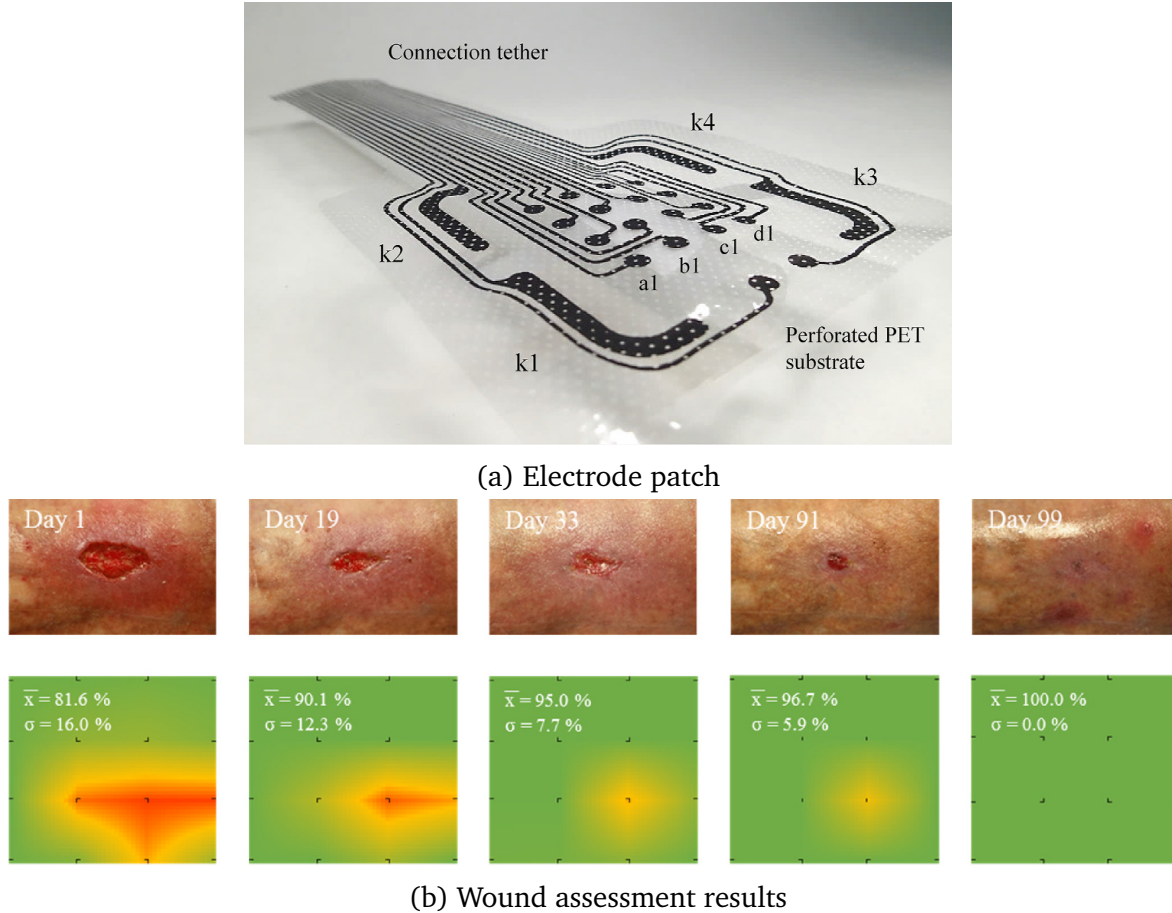


Figure II.10: Clinical proof-of-concept of a bioimpedance method for monitoring ulcers by Kekonen et al. [6]

This wound assessment methodology is promising, as it provides an estimation of the status of a wound in two dimensions, recreating an image that helps visually monitor its healing without removing wound dressings. However, it still shows some limitations for long-term monitoring. The main weakness of this method is the application of an electrode patch directly on the wound. Even if the materials used are perfectly biocompatible, keeping a foreign body on a wound for an extended period is not advisable, as it can complicate tissue regeneration, and may provide a location for bacteria to colonize. Moreover, it prevents the regular application of antibiotic or anti-inflammatory ointments, disinfecting treatments, and easy removal of necrotic tissues by obstructing the wound, and would need to be removed every time treatment is necessary.

In contrast with this solution, Vitapatch electrodes would be placed around the wound,

leaving the traumatized tissue completely unobstructed while still providing an image and a bioelectrical assessment of the wound status.

Finally, the work described in “Development of an Electrical Impedance Tomography Spectroscopy for Pressure Ulcer Monitoring Tool: Preliminary study”[7] also deserves a mention, as the project of the authors is extremely similar to the Vitapatch project. This article also mentions the use of a non-invasive ring of electrodes to place around a wound to perform bioimpedance measurements and assess wound healing by transmitting data to a smartphone. The similarities however end here, as they took a completely different path towards image reconstruction than what is planned in this project. Indeed, the authors are using a combination of computed tomography algorithms to create images of the conductivity distribution based on impedance measurements, and a machine learning classification algorithm to create a map of pixels supposedly indicating the probability of wounded tissue at each pixel. The key differences between computed tomography and why it was chosen to use electrical impedance tomography for this project are discussed in Part V. Unfortunately, the article lacks images and examples of reconstructed wound images, but the work of Kang et al. will be interesting to follow in parallel to the Vitapatch project to compare the performances of the two image reconstruction approaches.

## Part III

# Proposed spectroscopy method and circuit

After gathering information about the electrical properties of human skin and the impedance changes caused by a wound, and laying the foundations for a good bioimpedance measurement, focus can now be put on an electronic circuit for bioimpedance spectroscopy.

Many design choices have to be made when designing a circuit. For the Vitapatch project, circuit design was the responsibility of a research engineer working for Microsys. Understanding and analyzing his choices is important to be able to critically analyze the data acquired using this circuit.

In this third part, the components of the first prototype Vitapatch bioimpedance measurement PCB designed by Microsys that are relevant for data processing are described. Then, using a virtual model and simulations, the behavior of the measurement circuit is analyzed in silico, to identify the necessary signal processing steps for the use of this circuit.

### III.1 Prototype PCB description

For the Vitapatch research project, a bioimpedance measurement PCB was designed by Ir. Morgan Diepart of Microsys. The goal for this PCB is to create a measurement solution that would be aggressively miniaturizable and extremely power efficient, to integrate it into an easily deployable patch able to perform measurements and use the Internet of Things (*IoT*) protocols to send data to a gateway like a smartphone and process the measurements on that device. A picture of the prototype PCB is shown in Figure III.1.

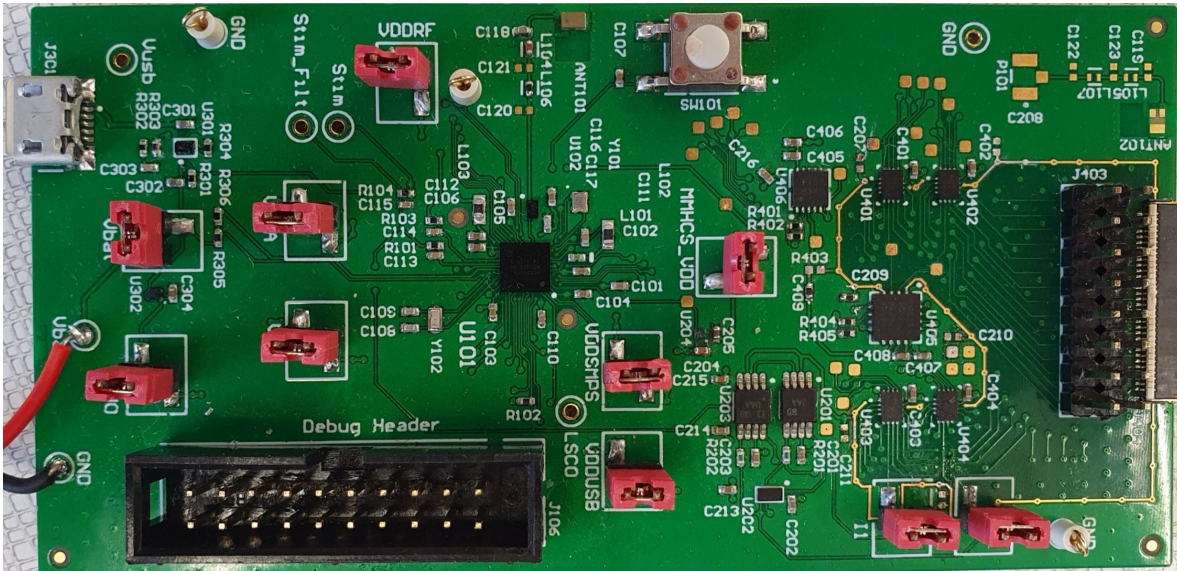


Figure III.1: Prototype Vitapatch bioimpedance measurement PCB manufactured by Microsys

### III.1.1 Microcontroller

At the heart of the Vitapatch PCB designed by Microsys lies a STM32WB55 32-bit ARM-based Cortex M4 microcontroller [42]. This MCU is responsible for some of the main functionalities of the circuit such as

- Generating a stimulation signal for current injection and commanding a controlled current source,
- Sampling and performing analog-to-digital conversions of the required signals (see section III.1.5),
- Establishing a Bluetooth Low Energy communication with a computer or smartphone, to receive measurement instructions and respond with the corresponding data,
- Controlling multiplexers (see section III.1.4) for using the right electrodes for current injection and voltage sensing, and
- Managing the power of the entire PCB to ensure maximum autonomy of the device, for example by powering down the measurement circuits when not needed, and monitoring the battery charge.

### III.1.2 Excitation signal

The choice of an excitation signal was of prime importance for the project, as it directly determines the amount of information available for the impedance spectroscopy, but can also greatly impact the power consumption of the device depending on the required measurement duration.



From this point on, only the magnitudes of the frequency domain signals and quantities are considered. For impedance spectroscopy, information about the phase is redundant and unintuitive. Moreover, circuit components such as operational amplifiers can have some effects on the phases of the signals which are not necessarily well documented and easy to analyze. As the magnitude  $|Z|$  of an impedance is sufficient to evaluate its corresponding resistance and reactance, phase is disregarded in the rest of this work.

**a) Sinusoidal signal** Conceptually, the simplest signal that could have been chosen for excitation is a sine wave. An ideal sinusoidal signal  $A \sin(\omega t)$  of constant amplitude  $A$  and angular frequency  $\omega$  only contains a single component in the frequency domain. This means that, ideally, for any given excitation frequency, the amplitude of the measured impedance at that frequency can simply be obtained as the ratio between the amplitudes of the excitation signal and the measured response, as per Ohm's law.

Despite the apparent simplicity of processing an impedance measurement performed with a sine wave, this type of signal presents several practical disadvantages that easily disqualify it for this project.

First, because of the spectral nature of a sine wave, each measurement provides information about a single frequency, a single point in the spectrum of the measured impedance. This implies that to obtain a somewhat rich spectrum up to 1 MHz, hundreds if not thousands of consecutive measurements at different frequencies would be required. Such a procedure would increase the amount of data to be collected and transferred and would multiply the time required to perform a measurement by several orders of magnitude, not only because each current injection and voltage measurement would require some time, but also because of the unavoidable overhead for signal conversion, storage, transfer, ... between each measurement.

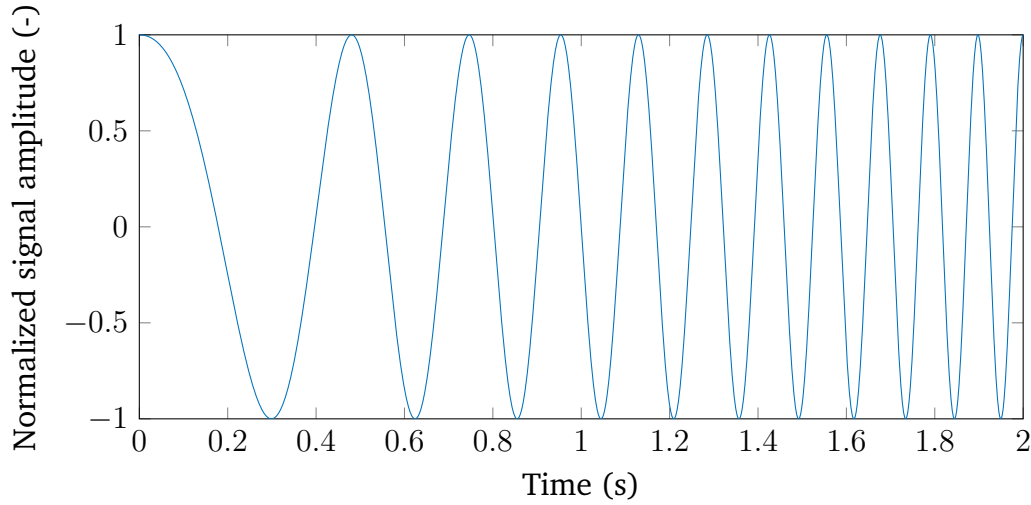
Second, generating a sine wave generated with digital components is no easy task and does not produce ideal results. Indeed, even a complicated combination of potentially filtered digital signals can do no better than crudely approximating a sine wave, and cannot be expected to have a pure and straightforward spectral representation. A solution to this problem would be the use of digital-to-analog converters (DAC), but adding these components to the circuit would be a burden in terms of size and power consumption, which goes against the objectives of the Vitapatch project.

**b) Chirp signal** A standard type of excitation signal in spectroscopy, that maintains many advantages of a sine wave while overcoming some of its practical flaws is the chirp signal. By definition [43], this type of signal is a pseudo-periodic signal, modulated in frequency around a carrier  $a$  and amplitude by an envelope that varies slowly compared to the oscillations of the phase  $\phi$ :

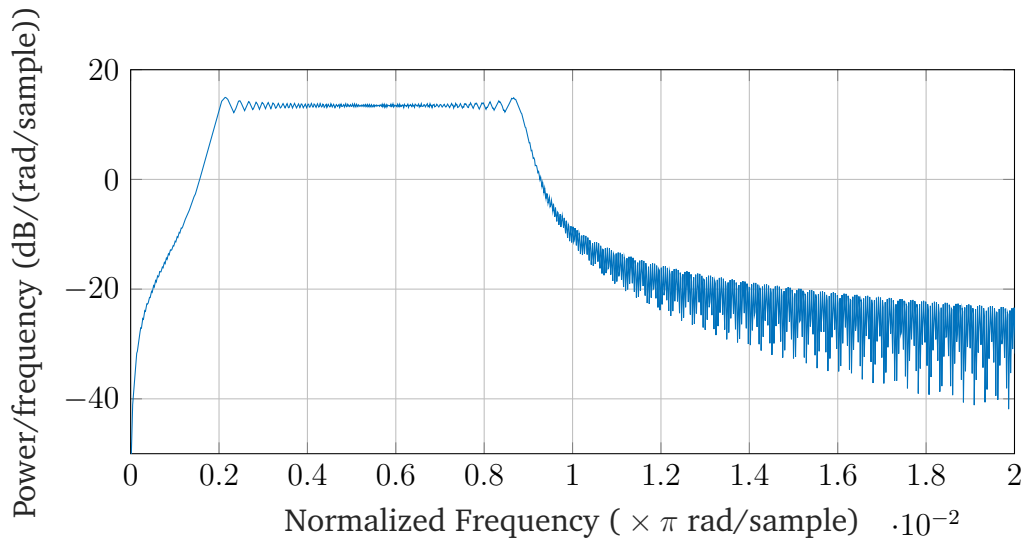
$$c(t) = a(t)e^{i\phi(t)}$$

It is more common to consider a linear chirp, characterized by a constant amplitude envelope and a linearly increasing frequency. Such a signal takes the shape of a

sine wave of gradually increasing frequency, as shown in Figure III.2a. As expected, this signal is much richer in terms of frequency contents than a simple sine wave, as illustrated by its power spectral density represented in Figure III.2b.



(a) 2-second linear chirp signal varying from 1 to 10 Hz



(b) Chirp power spectral density for a 50-second chirp sampled at 10 kHz, varying from 5 to 45 Hz

Figure III.2: Illustration of a chirp signal in time and frequency domains

It is easy to understand why this kind of signal is popular for spectroscopy: through a single excitation, information about an entire frequency band can be obtained. Compared to a succession of sine wave excitations, the use of a linear chirp reduces the signal generation and acquisition times, and the quantity of data to store, process, and transfer. It also provides continuous spectral information over its frequency band, as opposed to discrete measurements with sinusoidal signals.

Unfortunately, this solution could not be retained for the project, once again because of the need for a DAC to generate this kind of signal properly.

**c) Pseudo-random binary sequence** The final choice of excitation signal to be used for the Vitapatch project is a pseudo-random binary sequence. Such a signal is a sequence of bits generated by a deterministic algorithm, but that still possesses statistical characteristics of a truly random sequence. A signal generated from a pseudo-random sequence of bits is a rectangular-looking signal, with a constantly varying period. The order  $n$  of a PRBS sequence defines the maximum period length of the signal as  $2^n - 1$  [44]. An example of a pseudo-random binary sequence is given in Figure III.3a.

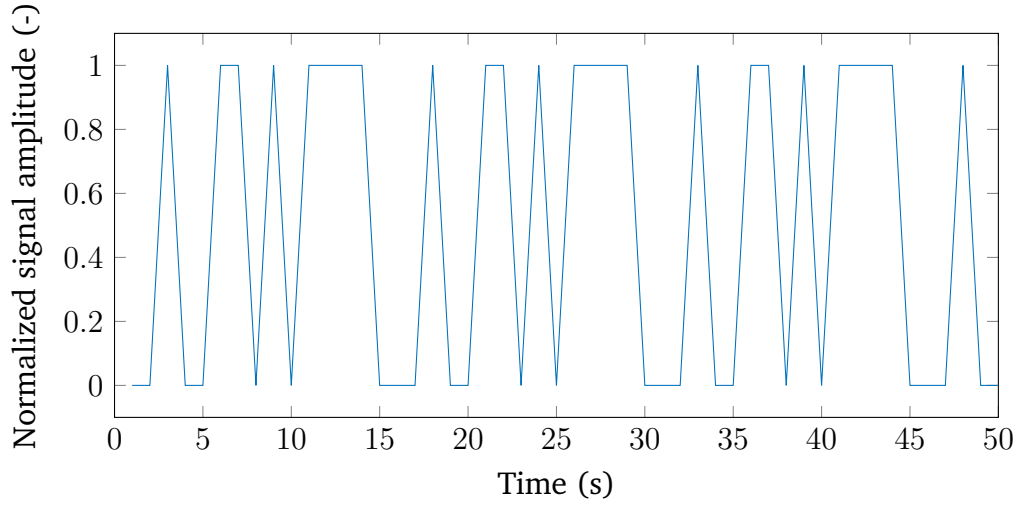
The choice of such a signal for impedance spectroscopy is not arbitrary. Indeed, despite being most commonly used in telecommunication, applications of this signal for impedance measurement of batteries, which exhibit a strong frequency dependence due to capacitive effects, exist in the literature [45].

The amplitude spectrum of an ideal rectangular wave exhibits frequency components at every odd multiple of its natural frequency. These components decrease in amplitude by a factor  $2n + 1$  at each harmonic  $n$ .

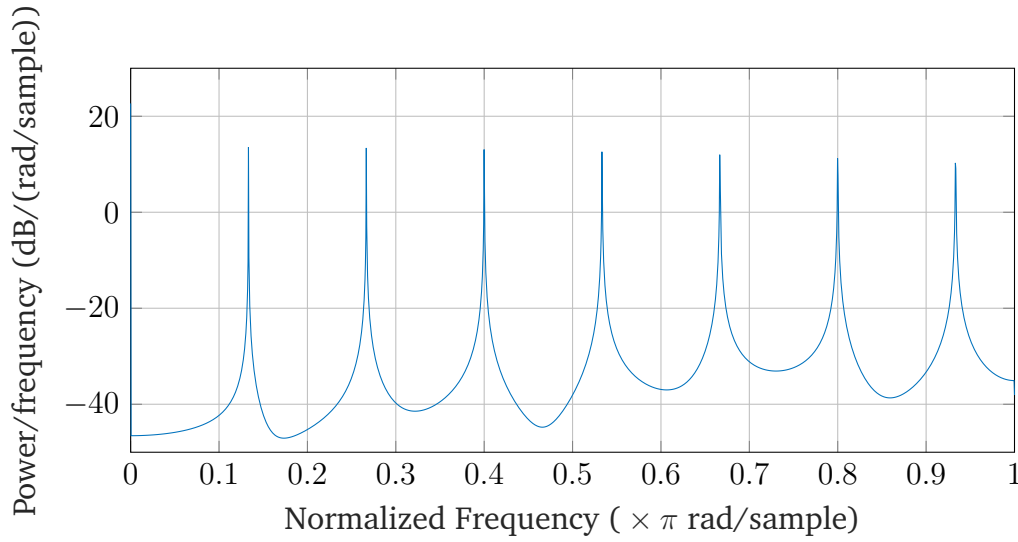
As a pseudo-random binary signal is essentially a superposition of a multitude of rectangular signals, it is easily conceivable that, like the chirp signal, a short pseudo-random sequence has a rich amplitude spectrum and allows the exploration of a wide range of frequencies in little time. To illustrate this, the power spectral densities of two pseudorandom binary sequences are given in Figures III.3b and III.3c. These two graphs show that as the order of the sequence is increased, the power of the signal is spread more and more evenly across the entire frequency spectrum.

The use of this signal also solves the main weakness of the previously explored options: as it is a purely binary signal, the need for a DAC is eliminated, and the excitation signal can be directly generated by a microcontroller.

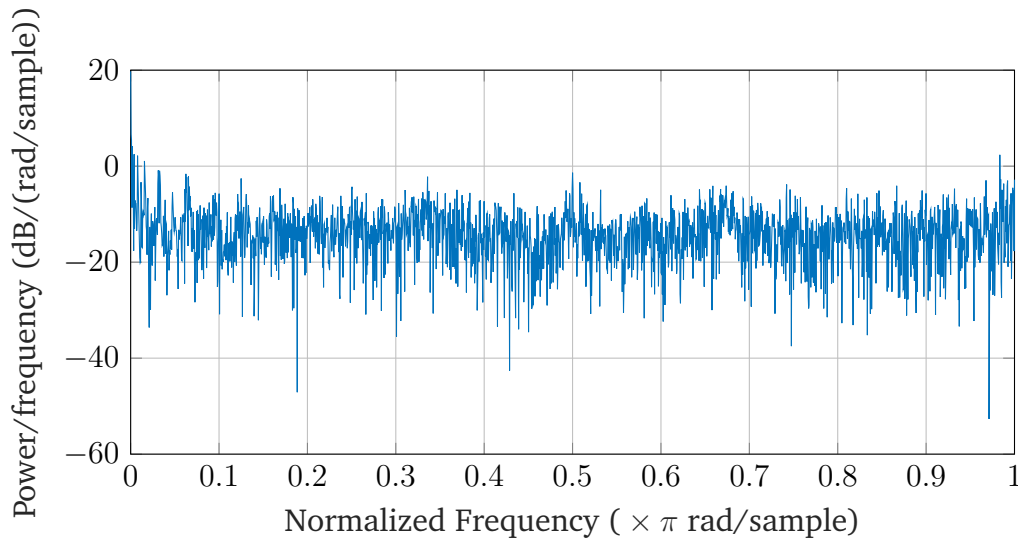




(a) 50-second fourth-order pseudo-random binary sequence with a 1 Hz rate of change



(b) Power spectral density of a fourth-order pseudo-random binary sequence



(c) Power spectral density of a 64<sup>th</sup>-order pseudo-random binary sequence

Figure III.3: Illustration of a pseudo-random binary sequence in time and frequency domains

Despite the attractiveness of this signal, exploiting measurements acquired with a pseudo-random binary excitation leads to some challenges on the processing side that were absent with previous solutions.

First, measuring and sampling the excitation itself in a similar fashion to the response is almost necessary for deducing an impedance spectrum from any measurement. Indeed, because of the pseudo-random nature of the excitation spectrum, it is not possible to assume its shape in advance and deduce the impedance spectrum from the response using a predetermined excitation spectrum. The pseudo-random sequence can be fully determined by knowing the seed used for generating it, but knowing the precise instants at which sampling was performed would be necessary to correctly determine the stimulation spectrum.

Moreover, because filters are applied to the pseudo-random binary sequence after it has been generated and before it is translated into a current, as will be discussed later, it is wiser to sample the signal after it has been filtered, rather than trying to infer the effect of the filters on the sequence. This reasoning can be brought even further by considering the possibilities for noise or issues in the signal generation. By sampling the stimulation corresponding to each response, one does not need to rely on the hypothesis that signal generation went as expected and that noise was not introduced by interference pickup or other phenomena.

Second, the theoretically infinite number of harmonics of a rectangular signal raises some concerns in digital signal processing. A well-known phenomenon in this field is aliasing: any frequency component in a sampled signal found at a frequency greater than half the sampling frequency (a.k.a. the Nyquist frequency) will be "folded" into the signal spectrum obtained via a discrete Fourier transform [46]. Common practice therefore demands that the sampling frequency be chosen larger than twice the largest frequency component of the signal to measure to avoid errors in the obtained spectrum. However, using a pseudo-random binary sequence makes it theoretically impossible to determine a maximal frequency, as rectangular signals possess an infinite number of harmonics. Moreover, the random nature of the signal also makes it difficult to predict at which frequencies the folding phenomenon will become negligible. As will be explored later, mitigating the effects of aliasing is possible, but requires some planning in terms of filtering and signal processing.

### III.1.3 Analog circuit components

#### III.1.3.1 Mirrored Modified Howland current source

One of the principal components of the analog circuit of the Vitapatch PCB is a mirrored modified Howland current source. Its purpose is to take the pseudo-random excitation signal in the form of a voltage as its input and convert it into a current with a constant voltage-to-current gain and, ideally, no distortion. The current generated by this Howland source is then injected into the body whose impedance is to be measured.

To correctly serve its purpose, this current source should provide a constant and

direct voltage-to-current conversion in the entire frequency range of interest. Because the generated current is to be injected into the body, its amplitude should be limited to a value that respects medical safety standards (Table II.1), and its gain should therefore be selected accordingly. Another factor to take into consideration when selecting this gain is energy consumption. The injected current should indeed be as small as possible to maximize the battery life of the device.

The schematic of this circuit is shown in Figure III.4. Its principle of operation revolves around two operational amplifiers of wide bandwidth, in a symmetrical configuration. The purpose of this mirrored arrangement is to perform impedance measurement on a floating load. Analytical expressions for the voltage-to-current gain are developed in [47].

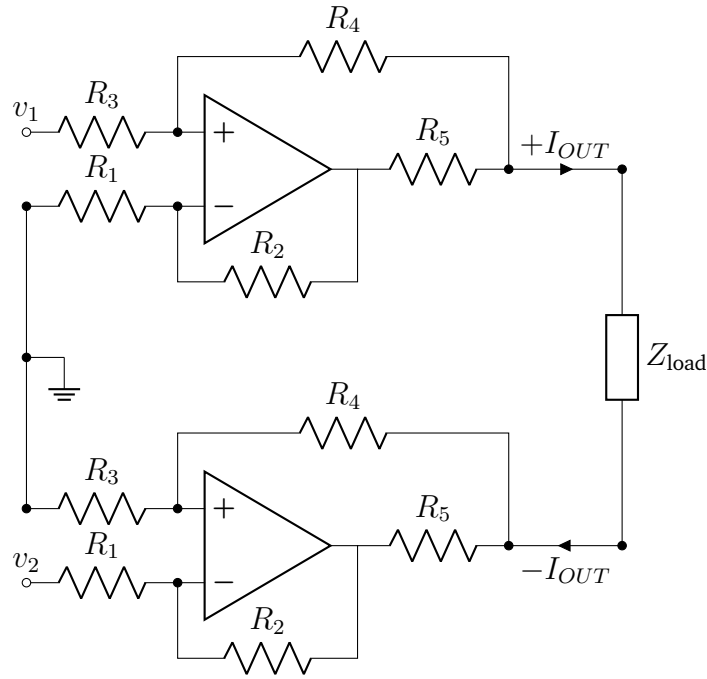


Figure III.4: Mirrored Modified Howland current source schematic (reproduced from [47])

Knowing that the amplitude of the pseudo-random signal generated by the microcontroller is 3 V, resistances were selected such that the voltage-to-current gain within the operation bandwidth takes a value of  $k_{IV} = 6.666 \times 10^{-6} \text{ A/V}$ . This gain provides a safe and energy-efficient maximal injected peak current of  $\pm 10 \mu\text{A}$ . This value is an order of magnitude lower than the low-frequency safety limit specified in Table II.1 and allows for efficient measurements only drawing very small amounts of power.

Because this circuit is based on operational amplifiers, important remarks regarding bandwidth and output limits have to be brought up. All real-life operational amplifiers have several non-ideal characteristics, one of which

is a finite bandwidth. This means that, for any of these components, there is a maximal frequency for the input signals above which the operational amplifier is not able to change its output fast enough to reflect input changes. In the case of the INA159 amplifiers used on the PCB, the bandwidth is 1.5 MHz [48], which is comfortably above the frequency range targeted for this project.

A second limitation of operational amplifiers is that they naturally cannot produce a greater voltage at their output than the voltage they are powered with. In the case of the Vitapatch PCB, the amplifiers are powered with 3 V. In practice, this means that the load impedance will be limited since the voltage difference that needs to be applied at either end to produce a constant current will increase with the value of that impedance. A quick calculation shows that the current source should not struggle to drive impedances lower than a few M $\Omega$ s, as a 1 M $\Omega$  impedance would require 1 V at its ends to be traversed by the target 10  $\mu$ A current. This limitation is therefore rather unlikely to be an issue in practice, thanks to the very small injected currents.

### III.1.3.2 Filtering and amplification stages

The response of the tested impedance is measured as a voltage via two electrodes, that differ from the current injection pair, as per the protocol of four-point impedance measurements (Section II.1.1). However, the resulting voltage from a stimulation of 10  $\mu$ A is generally too small to be measured directly. Assuming the measurement of a 1 k $\Omega$  resistor, the resulting peak voltage would indeed only be 1 mV, which could easily be drowned in DC voltage offsets, noises, and EMI pickup.

To perform a good analog-to-digital conversion of this response, an amplification stage is therefore present after the voltage measurement electrodes. To limit the effects of potential electromagnetic interference and signal harmonics outside of the frequency range of interest, some filters are also present at this stage.

**a) Instrumentation amplifier** The voltage measurement electrodes are directly connected to the input of an instrumentation amplifier<sup>1</sup>. This practice is extremely common for the measurement of analog floating signals, as an instrumentation amplifier provides a differential measurement with a high common-mode rejection, and a decent signal amplification with low added noise when the components are selected properly.

The amplifier used on the Vitapatch PCB is a AD8231 instrumentation amplifier. It features a programmable gain of 1, 2, 4, 8, 16, 32, 64, or 128 V/V, and a bandwidth of 2.7 MHz when the gain is set to 1 [50]. In Section III.1.3.1, the limited bandwidth of operational amplifiers was mentioned. Actually, the reality of things is more complex when a variable gain is involved, and the bandwidth of an amplifier decreases when its gain increases. This characteristic is often specified as a constant gain-bandwidth (GBW) product. For the AD8231, the GBW is 7 MHz for gains of 4 and up. This means that, for a gain of 4 V/V, the bandwidth decreases from 2.7 MHz to  $\frac{7 \text{ MHz}}{4} = 1.75 \text{ MHz}$ ,

<sup>1</sup>All About Circuits. *The Instrumentation Amplifier*. URL: <https://www.allaboutcircuits.com/textbook/semiconductors/chpt-8/the-instrumentation-amplifier/> (visited on 08/20/2022).

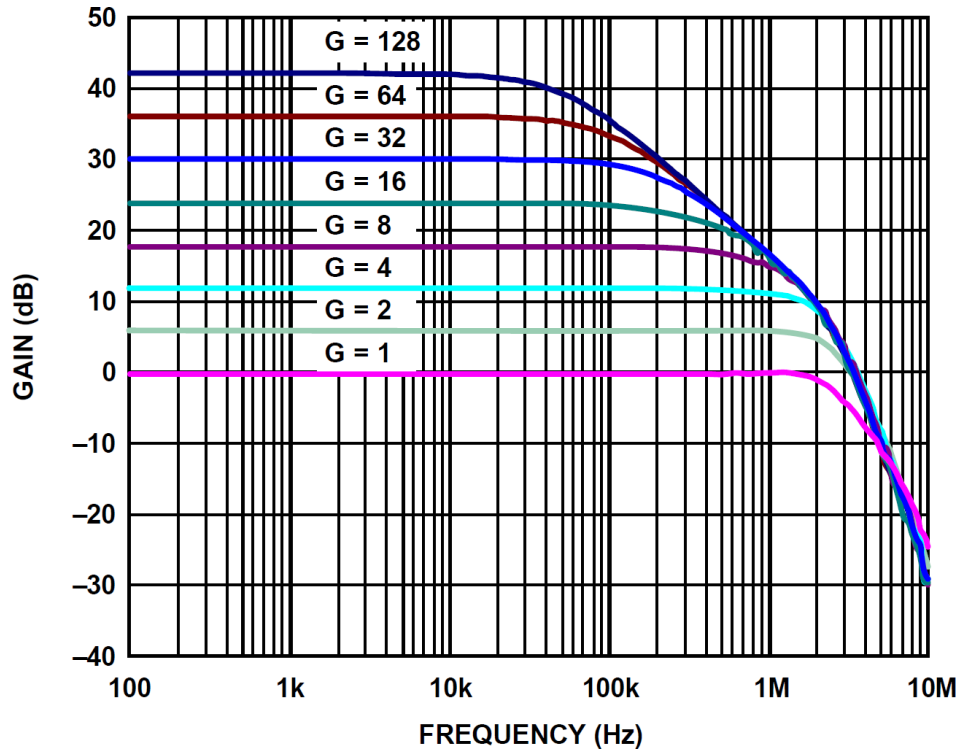


Figure III.5: Frequency response of the AD8231 instrumentation amplifier for different gains (from [50])

and so on for higher gains. Above the bandwidth limit, the gain of the amplifier progressively drops, as shown in Figure III.5.

After experimenting, the gain of the amplifier was set to 16, which led to a bandwidth of  $\frac{7\text{MHz}}{16} = 437.5\text{kHz}$ . This frequency is slightly below the Nyquist frequency of 500 kHz, which means that a few frequencies towards the end of the measured impedance spectra will need to be ignored. This is a favorable tradeoff towards aliasing reduction, as a gain of 8 would have led to a bandwidth of 875 kHz, meaning that parts of the spectrum above the Nyquist frequency, which we would like to reduce, would have been amplified instead of naturally rejected by the amplifier.

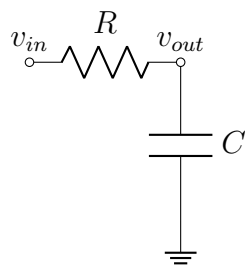
**b) Non-inverting amplifier** A second amplification of the measured differential response is provided by a non-inverting amplifier, placed after the output of the instrumentation amplifier. Because the gain of the instrumentation amplifier is limited due to its gain-bandwidth product and the need to preserve frequencies of interest, this amplifier is present to provide an additional boost in signal amplitude before sampling. An ADA4805 operational amplifier is used in a non-inverting configuration<sup>2</sup>, providing an additional gain of 4 V/V with a bandwidth of 105 MHz [52]. Ignoring filtering, this brings the total signal amplification to 64 V/V.

<sup>2</sup>ElectronicsTutorials. *Non-inverting Operational Amplifier*. URL: [https://www.electronicstutorials.ws/opamp/opamp\\_3.html](https://www.electronicstutorials.ws/opamp/opamp_3.html) (visited on 08/20/2022).

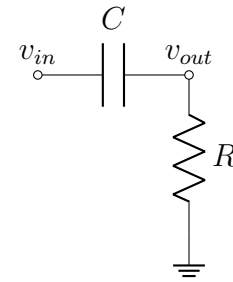
Note that, when placing several amplification stages in series in an electronic circuit, good practice demands that the first amplification stage have the lowest noise characteristics and the highest possible gain, to avoid amplifying noise. This rule is indeed respected here.

**c) Filters** Aside from the two amplifiers, the measurement stage of the circuit also contains some filters, as mentioned already. These filters are all passive first-order RC filters, with a cutoff frequency given by

$$f_c = \frac{1}{2\pi RC}$$



(a) Low-pass filter



(b) High-pass filter

Figure III.6: First order RC filters

**i. High-pass filter** The first filter used to remove unwanted signal components is a high-pass filter, placed between the output of the instrumentation amplifier and the input of the non-inverting amplifier. Its purpose is to attenuate low-frequency components resulting from electromagnetic interference picked up by the circuit, and remove any DC offsets that might have been introduced by electrode imbalance. Its cutoff frequency is set at 159 Hz, which allows it to remove the first 3 harmonics of 50 Hz power-line interference, and any DC offset. Removing this offset is particularly important for the analog-to-digital conversion of the signal, as it would cause a mismatch between the references of the signal and the ADC otherwise.

**ii. Low-pass filter** Finally, low-pass filters are present in various places on the PCB. The purpose of these filters, with a cutoff frequency set at 200kHz, is to limit the magnitude of frequency components of the signal above the Nyquist frequency (500 kHz). This way, aliasing, which was a concern linked to the use of a pseudo-random binary signal, should be limited thanks to the attenuation of high frequencies. Such filters are placed at the inputs of the analog-to-digital converter, and the output of the stimulation generator.

The choice of cutoff frequency is a tradeoff between strong attenuation of the components above the Nyquist frequency and attenuation within the frequencies of interest. Indeed, these filters attenuate frequencies above 200 kHz, which is below

the Nyquist frequency. Strictly speaking, this means that the measurement results between 200 and 500 kHz will be invalidated. However, this is a very favorable tradeoff, as the attenuation of frequencies above 500 kHz will reach  $-8.6$  dB and more, as opposed to only  $-3$  dB if the cutoff frequency was set exactly at 500 kHz. Moreover, this frequency range affected by the filter only represents a very small part of the useful spectrum on a logarithmic scale that can be ignored in the data analysis without much concern. Adding to that is the fact that the measured impedance will always feature a capacitive part, which will naturally bring the magnitude of the impedance to low values at such high frequencies.

### III.1.4 Electrode multiplexing

To perform a detailed assessment of a wound through bioimpedance spectroscopy or impedance tomography, several impedance measurements at different points in space are required. This is achieved by using an array of electrodes positioned in a known configuration and using them successively as current injection or as voltage measurement electrodes.

This dual purpose of each electrode requires a way of connecting them either to the output of the Howland current source or to the input of the instrumentation amplifier at will, using the microcontroller to orchestrate this switching.

To that end, the PCB features four multiplexers<sup>3</sup>, each of them connected to half of the electrodes used for bioimpedance spectroscopy. Two are used for connecting electrodes to the output of the Howland current source, while the others are used for voltage measurements.

The choice of using two multiplexers has some consequences, as it means that not all configurations of current and voltage electrode pairs are achievable on command in practice. Only electrodes connected to different multiplexers can be used together for a current injection or a voltage reading. This requires current injection patterns to be carefully studied in advance, to connect the electrodes in a way that makes the desired strategy possible. These considerations are studied later, in Parts V and VI.

### III.1.5 Sampling and analog-to-digital conversion

Last but not least, the impedance spectroscopy workflow relies on analog-to-digital conversion for data transmission and signal processing. This conversion is performed by the analog-to-digital converter built into the STM32WB55 microcontroller. This ADC has a resolution of 12 bits and is capable of acquiring 4.26 Msps (millions of samples per second).

For each measurement sequence, two signals are sampled and converted: the amplified and filtered voltage response measurement, as expected; but also the stimulation signal generated by the MCU, at the input of the Howland current source.

<sup>3</sup>Wikipedia. *Multiplexer*. URL: <https://en.wikipedia.org/wiki/Multiplexer> (visited on 08/20/2022).

Sampling the stimulation signal is crucial for signal processing when using a pseudo-random binary sequence for current injection, as its frequency spectrum cannot be predetermined due to the random nature of the signal. Measuring the stimulation signal and knowing the voltage-to-current gain of the Mirrored Modified Howland current source will allow the device performing the signal processing to compute the spectrum of the stimulation current corresponding to each voltage response, and unequivocally deduce the correct impedance spectrum from the measurements.

Both of these signals are sampled at a frequency of  $f_s = 1$  MHz, and 4096 samples are taken for a measurement time of less than 5 ms.

## III.2 Circuit modeling and measurement simulations

To investigate the expected behavior of the measurement circuit before its assembly and prepare signal processing routines, a Simulink model was built and simulated. From simulated measurements, the behavior of the circuit can be compared against theoretical expectations, and attention can be drawn to potentially unexpected phenomena.

### III.2.1 Simulink model

The Simulink model used for this part of the project features all the necessary components to simulate an impedance spectroscopy measurement on a given load. It leverages the physical signal simulation capabilities of Simscape to model the analog circuit components and quantities, and converts these quantities into digital data for processing on MATLAB, emulating the analog-to-digital conversions taking place in the microcontroller of the Vitapatch PCB.

The full Simulink model used in this section is represented in Appendix A.

#### III.2.1.1 Clock signal

In the circuit, the clock signal is used to generate the pseudo-random binary sequence and to drive the sample-and-hold circuits of the analog-to-digital converters. This behavior is simulated in the model via a 1 MHz clock source.

A crucial parameter for the realism of the simulation is the clock aperture jitter. This parameter, which can be set to one's preference in Simulink, represents uncertainty in the timing of the edges of a digital clock, which leads to differences in signal sampling times between each sample in the context of analog-to-digital conversion. More precisely, aperture delay is defined as the delay between an ideal sampling clock signal and the instant where a sample is actually taken. Aperture jitter is the standard deviation of the aperture delay. [54].

This value needs to be chosen wisely for meaningful simulations, as real measurements will undoubtedly suffer from clock jitter, whose impact will be shown in the simulations. Practical causes for clock jitter include non-idealities in the oscillating



frequency of the quartz crystal used for generating the clock signals, or the use of several phase-locked loops<sup>4</sup> in series to multiply and divide the clock frequency to the desired value.

### III.2.1.2 Operational amplifiers

The measurement circuit includes several operational amplifiers: in the Modified Mirrored Howland current source, in the instrumentation amplifier, and another in the non-inverting amplifier circuit. Simulink gives the opportunity of modeling these amplifiers as band-limited, non-ideal op-amps to mimic the real-life behavior of these components. More precisely, the DC gain, input and output resistances, slew rate, and bandwidth can be specified for simulations.

These parameters have been set according to reference values found in the datasheets of each component [48, 50, 52].

### III.2.1.3 Signal sampling

In Simulink, the analog-to-digital conversion is simulated by the following workflow. First, the physical Simscape voltage signal is converted into a Simulink signal at each simulation step. This signal is then passed through a sample-and-hold block controlled by the 1 MHz clock. The sampled value is then converted into a sequence of 12 bits by a quantizer block, before being held by a zero-order hold block for one clock cycle and sent to the MATLAB workspace.

### III.2.1.4 Passive components

Resistors and capacitors are used in several parts of the circuit, such as op-amp circuits and filters. To add a layer of realism to the simulation, Simscape allows for tolerances on the nominal values of the components to be specified, to add non-idealities present in real-life. Thermal noise (white noise produced by all resistors and proportional to their resistance value) can also be added to the simulations. For these first simulations, components were kept ideal, although the possibility of adding realistic imperfections is an interesting prospect for the future.

## III.2.2 Frequency response of circuit components

Thanks to Simulink's open-loop frequency response analyzer, the response of the circuit as a function of frequency can be simulated, to obtain empirical Bode plots of the frequency and phase response of the different components. These plots can also be compared to the expected theoretical response and transfer functions of these components. As previously, the circuit will be broken down into two parts: the stimulation generation and the response amplification and measurement stage.

---

<sup>4</sup>Wikipedia. *Phase-locked loop*. URL: [https://en.wikipedia.org/wiki/Phase-locked\\_loop](https://en.wikipedia.org/wiki/Phase-locked_loop) (visited on 08/20/2022).

To ensure the correctness of the simulations, the full simulated inputs and outputs of each circuit stage were obtained from Simulink, and the correlation between them was tested. In both cases, the correlation peak was at 0, meaning that the inputs and outputs were correlated and that no unwanted delay was added by the simulations.

### III.2.2.1 Response of the current stimulation generation stage

The current generation stage of the circuit is comprised of the Howland current source and its input low-pass filter.

The transfer function of a first-order low-pass filter is given by

$$H_{LP}(s) = \frac{1}{R_L C_L} \frac{1}{s + \frac{1}{R_L C_L}} \quad (\text{III.1})$$

which has a pole  $p_{LP} = \frac{-1}{R_L C_L}$ .

The bandwidth of an operational amplifier can be translated as a pole in its transfer function. With the Howland current source having a gain  $k_{IV}$  and a bandwidth of 1.5 MHz, its voltage to current transfer function can be written as

$$H_{\text{Howland}}(s) = k_{IV} \frac{1}{s + p_H} \quad (\text{III.2})$$

with  $p_H = -2\pi \times 1.5 \text{ MHz}$ .

The expected transfer function of the current stimulation generation stage is given by the product of (III.1) and (III.2) since the transfer function of the association of two systems in series is the product of their transfer functions :

$$H_{\text{stim}}(s) = k_{IV} \frac{1}{R_L C_L} \frac{1}{(s + p_H)(s + \frac{1}{R_L C_L})} \quad (\text{III.3})$$

Analyzing the response of the Howland source in conjunction with the low-pass filter is somewhat irrelevant, as the stimulation signal is sampled after the filter. Therefore, to simulate the frequency response of this stage, only the Howland source was considered. The Bode plot of its simulated frequency response is given in Figure III.7. It matches the expected frequency response of the Howland current source. From DC to around 1 MHz, the magnitude response is at a steady  $-103 \text{ dB}$ , which corresponds to the  $6.666 \times 10^{-6} \text{ A/V}$  gain of the Howland current source, as  $20 \log(6.666 \times 10^{-6}) = -103 \text{ dB}$ .

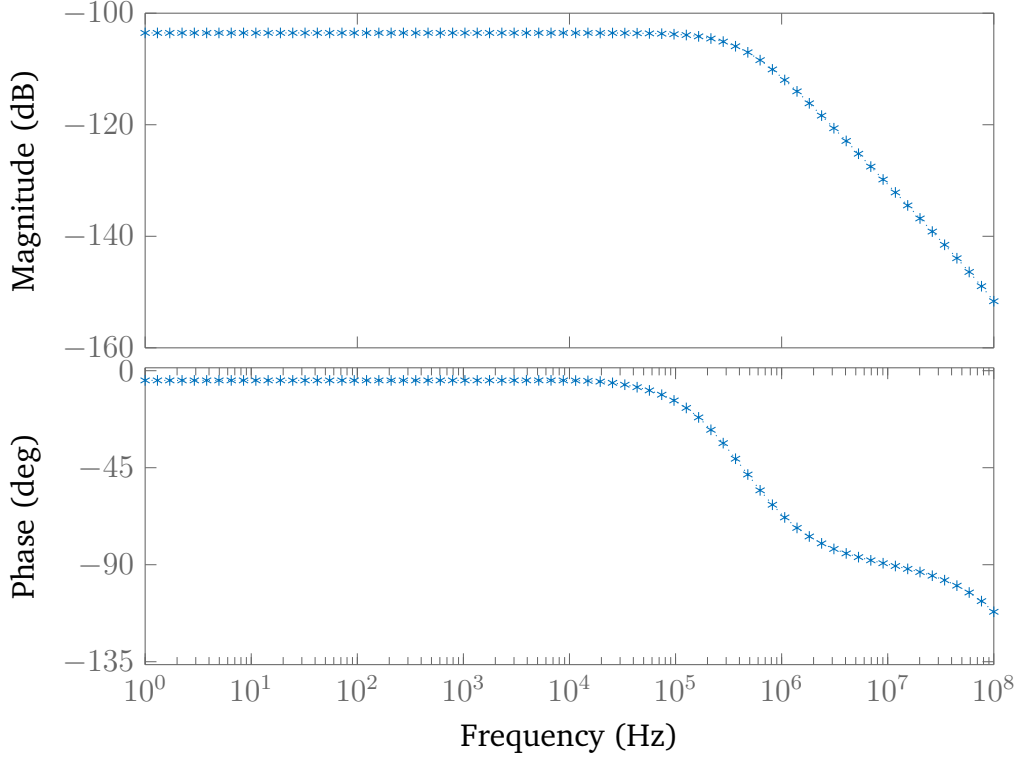


Figure III.7: Bode plot of the mirrored modified Howland current source

### III.2.2.2 Response of the voltage amplification and filtering stage

Similarly to the Howland current source, the instrumentation amplifier and the non-inverting amplifiers can be considered as having a one-pole transfer function similar to (III.2), with gains  $k_{\text{instr}} = 16$  and  $k_{NI} = 4$ , and poles at  $p_{\text{instr}} = -2\pi \times 437.5$  kHz and  $p_{NI} = -2\pi \times 105$  MHz respectively.

The transfer function of a first-order high-pass filter looks like the one of a low-pass filter, the main difference being the presence of a zero at  $s = 0$  :

$$H_{\text{HP}}(s) = \frac{s}{s + \frac{1}{R_H C_H}} \quad (\text{III.4})$$

The expected transfer function of the voltage amplification and filtering stage is therefore the product of the transfer functions of the two amplifiers, the low-pass, and the high-pass filters :

$$H_{\text{resp}}(s) = k_{\text{instr}} k_{NI} \frac{1}{R_L C_L} \frac{s}{(s + p_{\text{instr}})(s + p_{NI})(s + \frac{1}{R_L C_L})(s + \frac{1}{R_H C_H})} \quad (\text{III.5})$$

The Bode plot of the simulated frequency response of this stage of the circuit is given in Figure III.8. Once again, it globally corresponds to the expected frequency

response of the operational amplifiers and filters. The effect of the high-pass filter is showcased by the attenuation of low frequencies. However, low-frequency attenuation is much stronger than expected for some unclear reason. In theory, the magnitude response at 10 Hz should still be around 12 dB but reaches an astounding  $-60$  dB according to these simulations. By around 1 kHz, the magnitude response has reached the expected 36 dB corresponding to the voltage of 64 provided by the two amplifiers ( $20 \log(64) = 36$  dB). Unlike low frequencies, the high-frequency response of this stage is as expected: starting at 200 kHz, the magnitude response starts to drop thanks to the low-pass filter, with the pole of the instrumentation amplifier providing even more attenuation.

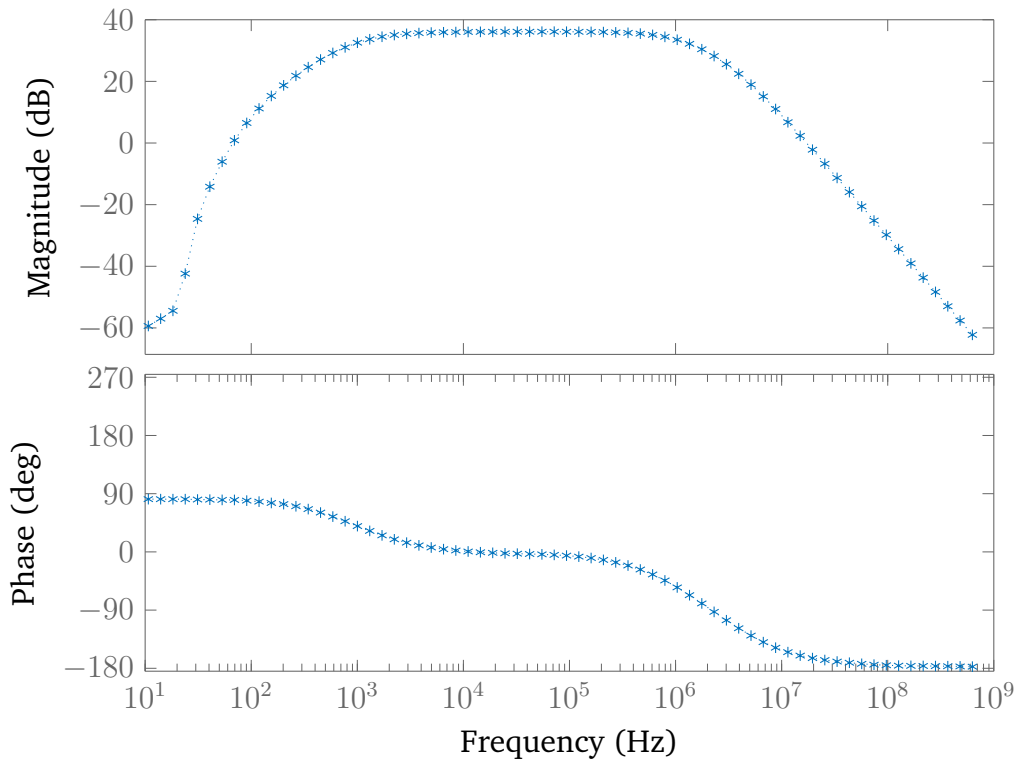


Figure III.8: Bode plot of the voltage amplification and filtering stage

### III.2.3 Electrode modeling

To validate the ability of the circuit to properly inject voltages and measure currents using skin electrodes, an electrode model was added between the test impedances and each current and voltage lead. The electrode model used was the more complete electrode model with half-cell potential shown in Figure II.5.

To ensure that variable contact impedances and DC half-cell potentials had no impact on the measurements, imbalances between the models of the four electrodes were introduced: the values of the electrode resistance and capacitance, and the half-cell potential were changed between each of the four leads. Changes were intro-

duced one at a time, and no variation in the amplified response output was observed between simulations.

This robustness to electrode imbalance can be attributed in part to the four-point electrode measurements. As explained in Section II.1.1, using different leads for current injection and voltage measurement ensures that contact impedances will not affect the measurement, even if they are not balanced. As for the half-cell potentials, the use of a differential measurement and the introduction of a high-pass filter in the amplification stage helps reject such DC voltages.

### III.2.4 Simulation results for a basic load

To get a taste of the signals created by this circuit, a very basic simulation for the measurement of a resistor can be performed.

To plot a very simple graph of the measured impedance, the sampled voltage response can be divided by the voltage gain of 64, while the sampled stimulation can be multiplied by the  $6.666 \times 10^{-6}$  A/V gain of the Howland current source. This way, the voltage measured at the ends of the resistor and the current injected into it can be divided to obtain a resistance value. Of course, filters and limited bandwidths make things more complicated than that in practice, but this will be discussed later. The goal, for now, is just to observe what the signals look like. The ratio of the sampled voltage and current for a simulation on a  $200\ \Omega$  resistor is shown in Figure III.9.

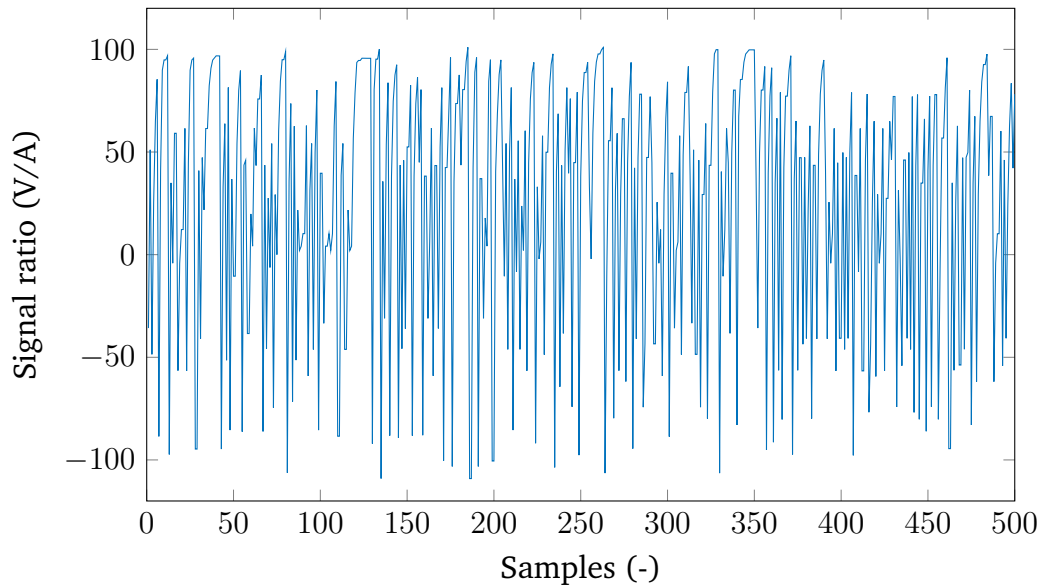


Figure III.9: Part of the simulated voltage by current ratio sampled for measurement of a  $200\ \Omega$  resistor

Clearly, obtaining a resistance value is not as simple as just dividing the measured voltage by the injected current. The use of a PRBS signal is making things more

complicated. Nevertheless, this simulation is somewhat reassuring, as one can see that the peak-to-peak amplitude of the signal ratio is  $200\ \Omega$ .

If all the loads were purely resistive, impedance measurement would be straightforward. But, adding a capacitance in parallel to the resistor to add some frequency-dependent behavior to the measured impedance clearly complicates things, as shown in Figure III.10.

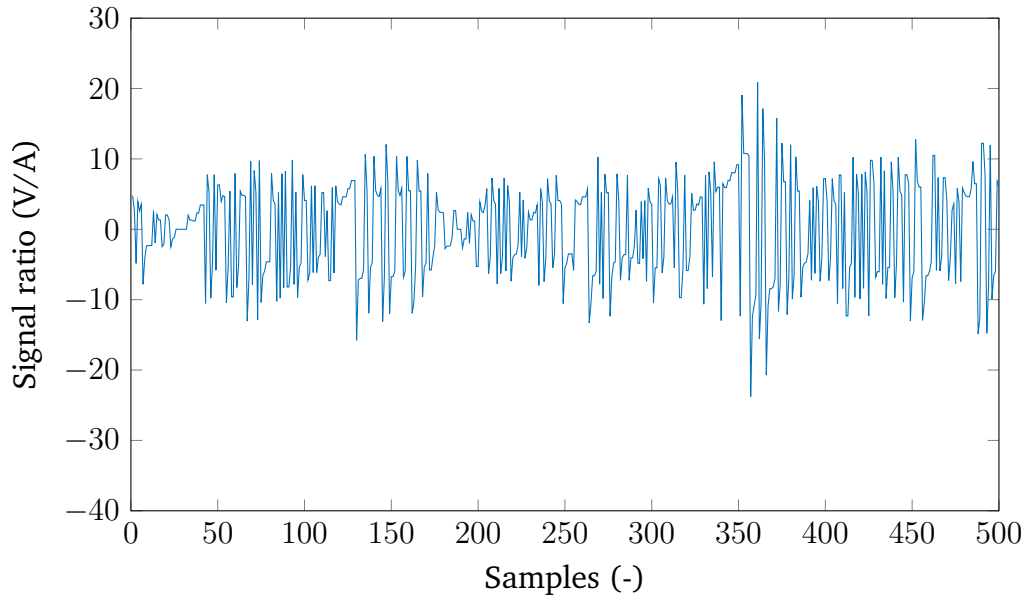


Figure III.10: Part of the simulated voltage by current ratio sampled for measurement of a  $200\ \Omega // 1\ \mu\text{F}$  R//C dipole

With a complex load, it is impossible to easily make out the value of the measured impedance by using time-domain signals. This is why, in the next part, Fourier analysis will be introduced to make sense of these signals in the frequency domain, and achieve impedance spectroscopy.

## Part IV

# Signal processing for low-power PRBS spectroscopy

The first simulated measurements with a model of the bioimpedance measurement circuit have shown the need for signal processing to complete the bioimpedance spectroscopy process.

On the one hand, complex impedances are difficult, if not impossible to analyze in the time domain. Using one of the most powerful tools of modern engineering, the frequency representation of signals and the Fourier transform, the acquired signals have to be manipulated and turned into an impedance spectrum.

On the other hand, as discussed and shown in Part III, the use of a pseudo-random binary sequence (*PBRS*) for current stimulation in bioimpedance spectroscopy is a promising way of generating a signal rich in frequency contents in a minimal amount of time, thus allowing for an energy-efficient data acquisition for spectroscopy in a wide frequency range. However, the methods used for generating and sampling this signal and the corresponding response are not without non-idealities, and a significant amount of noise and uncertainty is mixed with the useful information.

In this fourth part, the required Fourier analysis steps to obtain an impedance spectrum from the sampled stimulation and response signals are described. Then, to combat the high noise levels in the resulting data, a signal processing approach inspired by data science and machine learning is presented. Finally, experimental measurements are carried out to validate simulation results, and multiple steps taken to improve the obtained results by modifying the PCB are presented.

## IV.1 Fourier analysis for impedance spectroscopy

**a) Available signals** As a reminder, the measurement data to be exploited for impedance spectroscopy is obtained either via a Bluetooth or UART connection with

the PCB's microcontroller or through Simulink simulations. This data consists of two sets of 4096 voltage samples acquired by analog-to-digital converters at a sampling rate of  $f_s = 1$  MHz. One set of samples represents the stimulation signal, at the input of the Howland current source, while the other is the amplified and filtered voltage response of the load.

In the following,  $v_{\text{stim}}[n]$  refers to the sampled stimulation signal and  $v_{\text{resp, A}}[n]$  the sampled amplified response to the injected current ( $n \in [0, 4096]$ ). Square brackets indicate a discrete signal, and capital letters are used to refer to quantities in the frequency domain. Ideally, response and stimulation samples are taken at the same time, but clock jitter might affect the sampling and cause slight mismatches.

In Section III.2.2, the behavior of the Howland current source was analyzed through simulations, and it was established that, below 1 MHz, this part of the circuit could be considered as an ideal voltage-to-current converter with a gain  $K_{vi} = 6.666 \times 10^{-6}$  A/V. Therefore, the current injected into the load at any time can simply be obtained as  $i_{\text{stim}}[n] = v_{\text{stim}}[n]K_{vi}$ .

Meanwhile, obtaining the voltage difference between the two poles of the load is not as straightforward. Indeed, the frequency response of the entire amplification and filtering stage, which separates the voltage measurement leads and the voltage sampler, is more complex than a constant gain, as shown again in Section III.2.2. This is because the filters present in the path of the signal are actively affecting the frequency band of interest. Therefore, a constant gain cannot be defined in the time domain. The solution will be discussed later, but for now, assume that  $v_{\text{resp}}[n] = \frac{v_{\text{resp, A}}[n]}{64}$ .

**b) Fourier transform** In an ideal world, with a purely resistive load, ideal components with an instantaneous response time and no noise, the value of the impedance would simply be obtained as  $\frac{v_{\text{resp}}[n]}{i_{\text{stim}}[n]} \forall n$ . However, this does not hold anymore for a complex impedance with a capacitive part as was clearly shown in Figure III.10, hence the necessity for a Fourier analysis. In the frequency domain, the relationship

$$Z[s] = \frac{V_{\text{resp}}[s]}{I_{\text{stim}}[s]} \quad (\text{IV.1})$$

is valid as long as both signals have been sampled at the same time.

To compute the Fourier transforms of the stimulation and response sampled signals, the Fast Fourier Transform (FFT) can be used. In MATLAB, the `fft()` function implements this algorithm.

This function returns as many frequency points as there were samples in the given signals. These frequency points are placed on a double-sided spectrum, where positive and negative frequencies are mirrored on either side of the origin. To obtain a single-sided spectrum, it is necessary to "fold" it across the zero frequency. To do so, the negative half of the spectrum (a.k.a. the 2047 first points returned by the FFT) can be discarded, and the values of all remaining points except for the zero frequency



can be doubled to compensate for the power of the negative half of the spectrum [46].

**c) Response attenuation compensation** Via the aforementioned procedure,  $V_{\text{resp,A}}[s]$  and  $I_{\text{stim}}[s]$  can be obtained, and  $Z[s]$  can be computed via (IV.1) after computing  $V_{\text{resp}}[s]$  from  $V_{\text{resp,A}}[s]$ . To do so, the complete frequency response of the amplification and filtering stage needs to be considered, as the filters and limited component bandwidths will attenuate some parts of the spectrum of the voltage response. The theoretical transfer function of this circuit stage was given in (III.5). Using MATLAB's `freqresp` function, the value of the magnitude and phase response corresponding to this transfer function can be computed for any desired frequency. To compensate for attenuations of the response in the frequency range of interest (between 0 and the 500 kHz Nyquist frequency), the single-sided spectrum  $V_{\text{resp,A}}[s]$  can be divided by the frequency response corresponding to (III.5) at each frequency point. This way of compensating for filter attenuation allows to artificially cancel out the effects of the filters in the frequency range of interest while keeping their benefits outside of that range.

**d) Signal windowing** In practice, it is often necessary to apply a window to a signal before computing the FFT [46]. In theory, the exact frequency domain representation of a signal can only be obtained for an infinite sequence, defined for  $n \in ]-\infty, \infty[$ . Sampling a signal for a finite amount of time is equivalent to multiplying it by a rectangular window. Let  $x[n]$  be the infinite discrete signal being sampled,  $\hat{x}[n]$  the sampled version of that signal, and  $L$  the number of samples. In that case, the rectangular window can be defined as

$$w[n] = \begin{cases} 1, & n \in [0, L[ \\ 0 & \text{otherwise} \end{cases}$$

and  $\hat{x}[n] = w[n]x[n]$ .

The issue with this rectangular window is that it can cause phenomena called spectral smearing and power leakage. In fact, the Fourier transform of this window is given by a sinc function  $\frac{\sin(s)}{s}$ . The consequence is that all frequency components of the windowed signal end up multiplied by this sinc function illustrated in Figure IV.1a. The width of this function causes spectral smearing, a loss of resolution between the different frequency components, and the ripples around its main lobe lead to power leakage, making high power frequency components lose power to surrounding frequencies.

To reduce leakage and smearing, good practice in signal processing is to apply another non-rectangular window with a more desirable frequency spectrum to time-domain signals before performing a Fourier transform. A popular choice of window is a Hamming window, represented in Figure IV.1b. The impact of a Hamming window on the impedance spectra will be explored later.

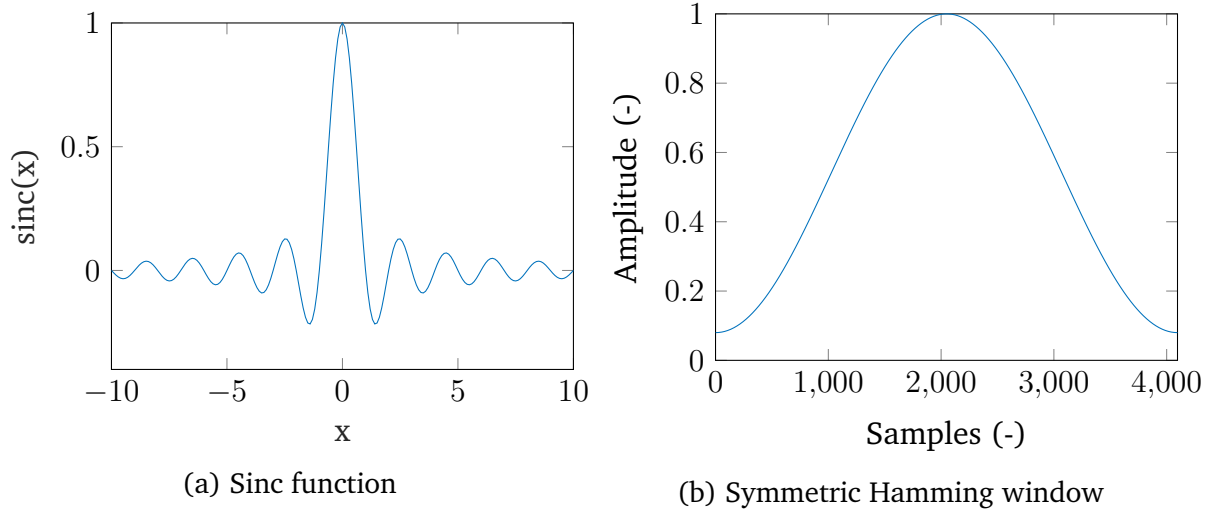
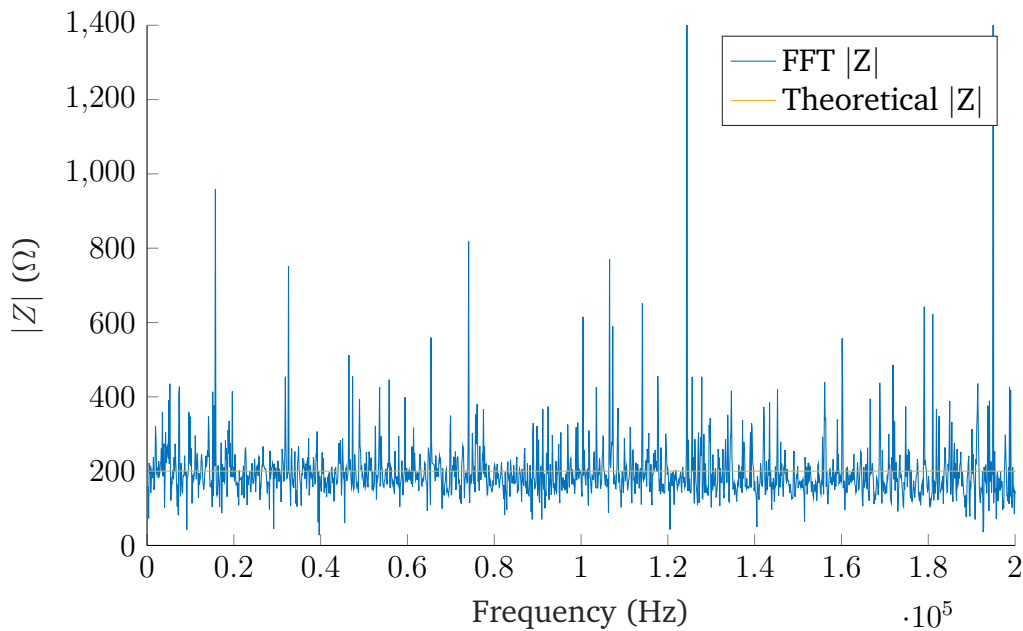


Figure IV.1: Illustrations of a sinc function and Hamming window

**e) Frequency scale and resolution** To determine the frequency scale of a spectrum computed via FFT, the number of samples  $L$  and the sampling frequency  $f_s$  are required. Each frequency point returned by the FFT algorithm is separated by  $df = \frac{f_s}{L} = 244.14$  Hz, and the resulting (single-sided) spectrum goes from 0 Hz to the Nyquist frequency  $f_N = \frac{f_s}{2} = 500$  kHz.

**f) Results** Results of the Fourier analysis described above for simulated measurements of a purely resistive and an R//C impedance are presented in Figures IV.2 and IV.3.

Figure IV.2: Simulated magnitude spectrum of a 200  $\Omega$  resistive load

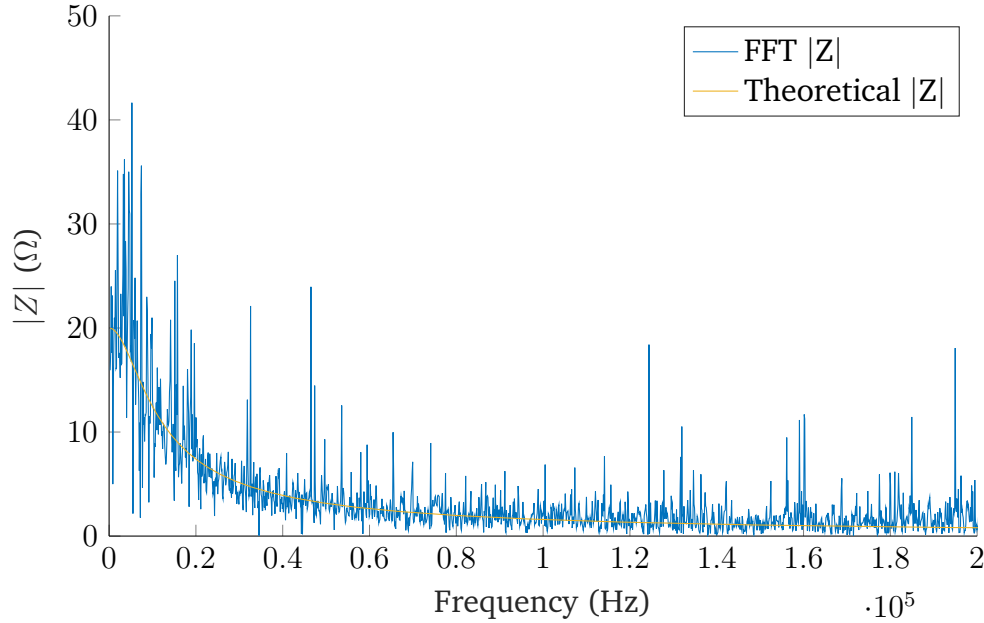


Figure IV.3: Simulated magnitude spectrum of a  $20\ \Omega//1\ \mu\text{F}$  R//C load

Looking at these simulations and the obtained impedance spectra via Fourier analysis, it is clear that this circuit will be unusable for impedance spectroscopy without some additional data processing to remove the noise likely caused by aperture jitter. In the next section, an approach to mitigating this noise, inspired by data science and machine learning, is explored.

## IV.2 Machine learning-inspired spectrum de-noising

In general, processing and filtering an electrical signal aims at getting rid of the effects of parasitic signals at given frequencies or some known artifacts caused by the signal conversion. Here, however, the noise appearing in the obtained impedance spectra is likely the result of a random phenomenon, clock jitter. As a consequence, the noise itself appears to be random and affects all frequencies. This means that traditional processing approaches are difficult to apply to this case.

It is useful to superimpose the theoretical spectrum of the measured impedances onto the simulated Fourier analysis results to try to find a solution to this problem. Looking at Figures IV.2 and IV.3, something interesting can be observed: despite the overwhelming amount of noise, the spectrum still follows a general trend, and the theoretical spectrum can be guessed throughout all the random variations. For a human, it could be possible to see and draw this trend and obtain a curve reasonably close to the theoretical one. However, the majority of traditional curve fitting algorithms cannot cope with the amount of noise present in the data and fail to give any good results. In MATLAB, the curve fitting toolbox provides several options to choose from, but even specifying the correct theoretical equation and letting the algorithms

try to find the resistance and capacitance values does not lead to any results. This is because traditional curve fitting routines are not meant to operate under such a heavy amount of noise, and give too much importance to the value of points that can be considered as outliers.

Thankfully, extracting trends from noisy data in a similar manner to what a human could be capable of is a task that data scientists have been obsessed with for a few decades now. Nowadays, a wide variety of machine learning algorithms are readily available and able to fit regression models on uncertain data. These methods all rely on a careful tradeoff between fitting the data used for creating models exactly and allowing some errors for better generality.

In the following, signal windowing is evaluated to make sure it does not affect the data used for recovering the impedance spectra. Then, a simple approach for mitigating noise is explored, before moving to machine learning itself.

### IV.2.1 Impact of signal windowing

In Section IV.1, the importance of using a window on sampled time domain signals was explained. However, as these windows are known to affect the frequency domain representation of these signals, it is important to identify their effects before attempting to fit a curve to the impedance spectra using regression algorithms. Indeed, if the magnitude spectrum is altered by the windows used on the signal in a certain frequency band, the affected data points should be treated with caution as they will lead to misleading results. To that end, the magnitude spectrum of the Hamming window applied to the stimulation and response signals is represented in Figure IV.4.

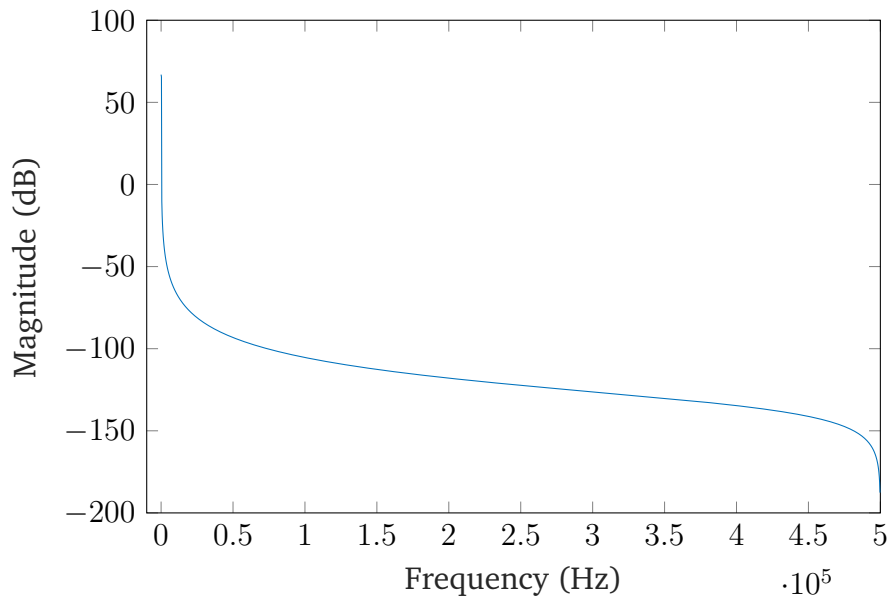


Figure IV.4: Single-sided magnitude response of the Hamming window applied to the signals

The Hamming window has a globally attenuating effect on the frequency spectra of the signals onto which it is applied. In the case where the stimulation or response signals were studied directly, this effect should be taken into account. However, as the ratio of these two signals is computed to obtain an impedance spectrum, the effect of the window on both signals is canceled out.

Nevertheless, it is important to notice that the very low frequencies are being amplified by the window. In practice, this has some adverse effects on the resulting spectra because of the high noise levels. Comparing the magnitude spectra for windowed and non-windowed signals, it became apparent that the zero frequency and the first nonzero frequency point, at 244.14 Hz, were affected by the windowing operation and strongly deviated from the theoretical spectra. A possible explanation is that the noise amplitudes in the stimulation and the response differ, which causes the amplification effect of the window to not be canceled out completely. The easiest way of avoiding this effect for the rest of the signal processing procedure is simply to ignore these two frequency points.

### IV.2.2 Hampel filtering

Before moving on to regression models, it is still worth trying to attenuate the noise present in the spectra to facilitate the work of the machine learning algorithms. Keeping the theme of data science, a method that can reduce random noise by averaging it out could be interesting.

A promising candidate is the Hampel filter. This filter computes a moving average of consecutive data points and replaces any of these points if it is too distant from its neighbors.

Applied to a magnitude spectrum obtained by FFT, such filter considers, for each discrete frequency, a window comprising that frequency and the  $k$  neighboring frequencies on the spectrum. The median of the magnitudes in that window is computed and replaces the magnitude at the current frequency if they differ by more than  $n$  standard deviations of the magnitudes in the window. This filter can be tuned using the number of neighbors  $k$  and the number of standard deviations  $n$ . The former will affect how much the spectrum will be flattened and uniformized, while the latter will dictate what level of noise will be tolerated.

The window size  $k$  was chosen equal to 3, to keep it very narrow and avoid over-averaging different parts of the spectrum and losing details, such as the inflection points and the slope of R//C spectra.  $n$  was kept to its default value of 3, as it seemed to lead to good attenuation of the largest noise peaks while keeping the details of the spectra as well. Results obtained with this filter for purely resistive and R//C loads are shown in Figures IV.5 and IV.6

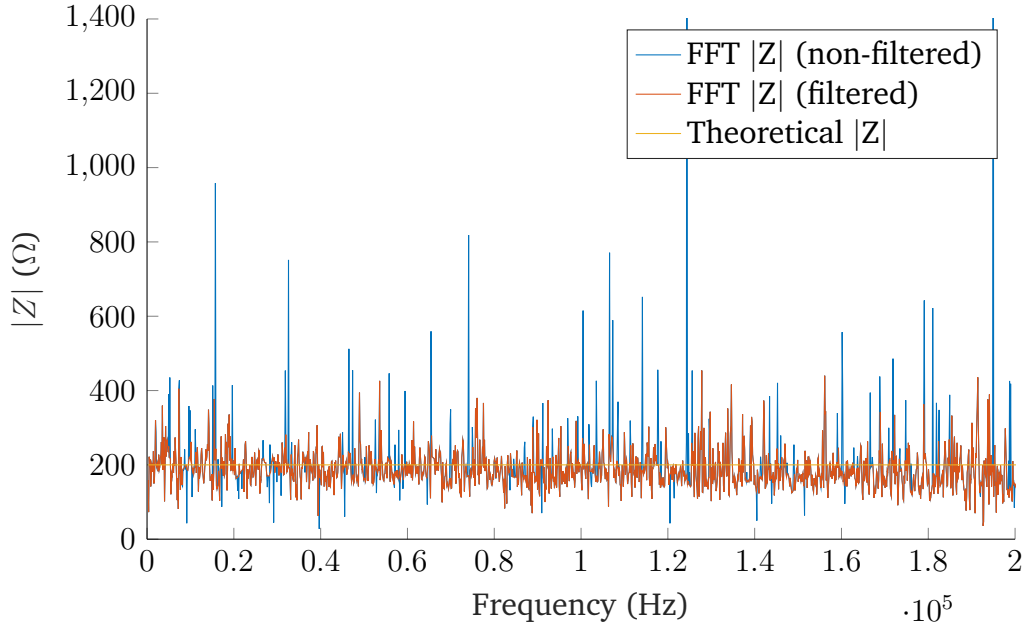


Figure IV.5: Effect of a Hampel filter on the simulated magnitude spectrum of a 200  $\Omega$  resistive load

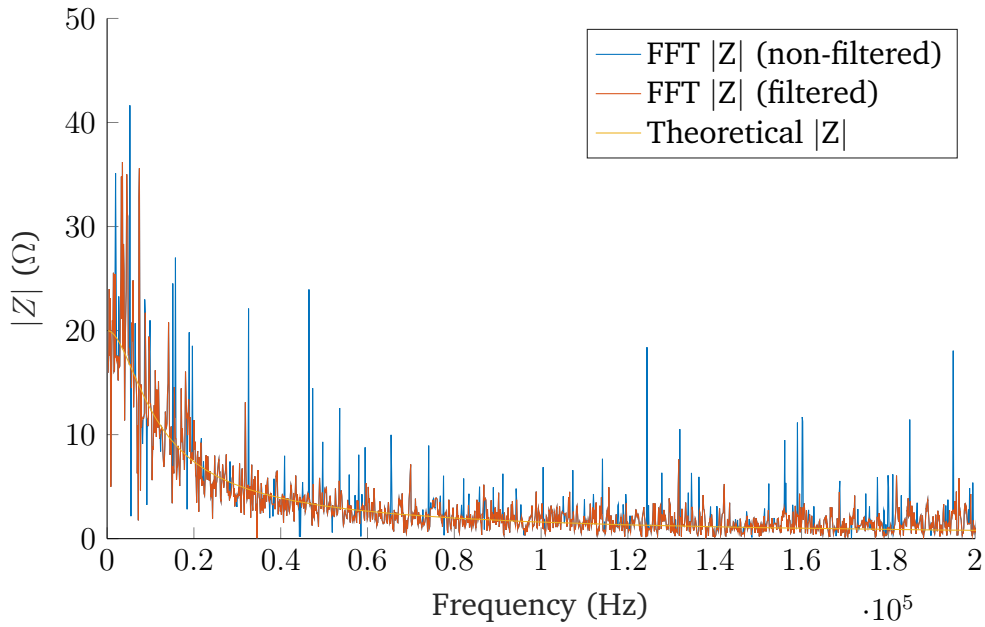


Figure IV.6: Effect of a Hampel filter on the simulated magnitude spectrum of a 20  $\Omega//1 \mu\text{F R//C}$  load

### IV.2.3 Least-squares forest boosting for noise removal

[56] Machine learning problems can be separated into two families: classification and regression, the first aiming to predict discrete characteristics, and the second

continuous ones. In the case of impedance spectra, the goal is to recreate functions that can take any real value, the problem is therefore a regression problem.

The way supervised machine learning algorithms are generally used for regression is the following: the objective is to find a model to approximate a function  $f(\cdot)$  of  $n$  variables. To that end, a dataset of points sampled from that function is created, consisting of several observations of the value of that function for different values of the  $n$  variables. The subtlety of machine learning is that these observations can be and typically are *noisy*, meaning that the sampled values of the function are not necessarily correct, and have some random errors added on top of them. Machine learning algorithms can fit models onto that dataset, and can be tuned to reject noise and create a general model that is well suited to then predict the value of  $f(\cdot)$ .

For this application, what will be done is not machine learning *stricto sensu*, as models will not be used to make predictions, but simply to approximate the noisy impedance spectra and reduce the noise by leveraging regression algorithms. In our case, we can consider that the only variable of the dataset is the frequency, and the function to approximate is the impedance magnitude as a function of frequency.

To select the right algorithm for the job, the notion of bias and variance of a machine learning algorithm can be described. Bias refers to the difference between a model generated by an algorithm and the Bayes model, a.k.a. a model that perfectly predicts the function to approximate. Variance quantifies the variation of the prediction of a model in response to noise within the dataset. In general, very simple models (such as linear regression) will display low variance and high bias, while complex models (like piecewise polynomials, interpolation models, ...) will have the opposite behavior. The words underfitting and overfitting are also used to describe models with high bias and high variance respectively. Very often, machine learning algorithms can be tuned towards under- or overfitting, depending on the amount of noise it has to deal with.

In the case of our noisy impedance spectra, it is abundantly clear that algorithm selection should be oriented towards underfitting models, as the data is under the effect of a lot of noise. Powerful machine learning algorithms are usually ensemble methods, that consist in training several models and combining them to create more powerful ones. The most suitable ensemble method for our problem is the boosting technique, which consists in combining several simple underfitting models to create a model with the low variance of the individual models while decreasing their bias and providing more accurate predictions. This technique is sequential: each model is created one after the other, according to the results obtained by the previous ones, and the final model is a weighted average of all previous models.

MATLAB's regression learner app is a powerful tool to easily try out different algorithms and visually assess their performance on different datasets. After trying different algorithms on several simulated impedance magnitude spectra, one of them stood out as the best performing and most satisfactory: the least-squares boosting algorithm, also referred to as least-squares forest boosting. Its general principle of

operation revolves around boosting regression trees. Without entering into details, a regression tree is basically a piecewise constant function of the variables of the dataset.

Regression results for the two previously analyzed and filtered impedance spectra are shown in Figures IV.7 and IV.8. These results are quite encouraging, as the boosted regression algorithm is able to make sense of the impedance spectrum and distinguish the general theoretical shape among all the noise. Results for a purely resistive load are good but not exceptional, which is not a concern as not encountering any capacitive effects in practice is rather unlikely. When a capacitance is added, the noise seems less prominent except at low frequencies, improving the regression fit. If the experimental conditions are such that noise is less of an issue, great fitting results can be expected.

The de-noising routine was tested on 10 different R//C loads, and fitting values of R and C using MATLAB's curve-fitting on the regressed spectra led to errors of 1 to 5 % on average, with larger errors of 10 to 20% appearing for very high impedances in the M $\Omega$  range.

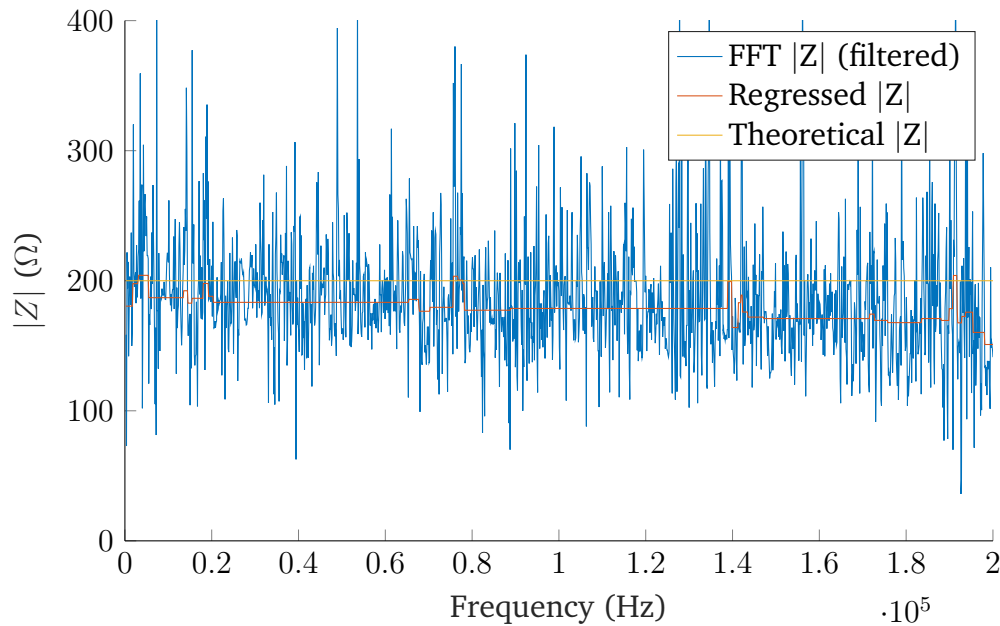


Figure IV.7: Least-squares forest boosting regression of the Hampel-filtered simulated spectrum of a 200  $\Omega$  resistive load



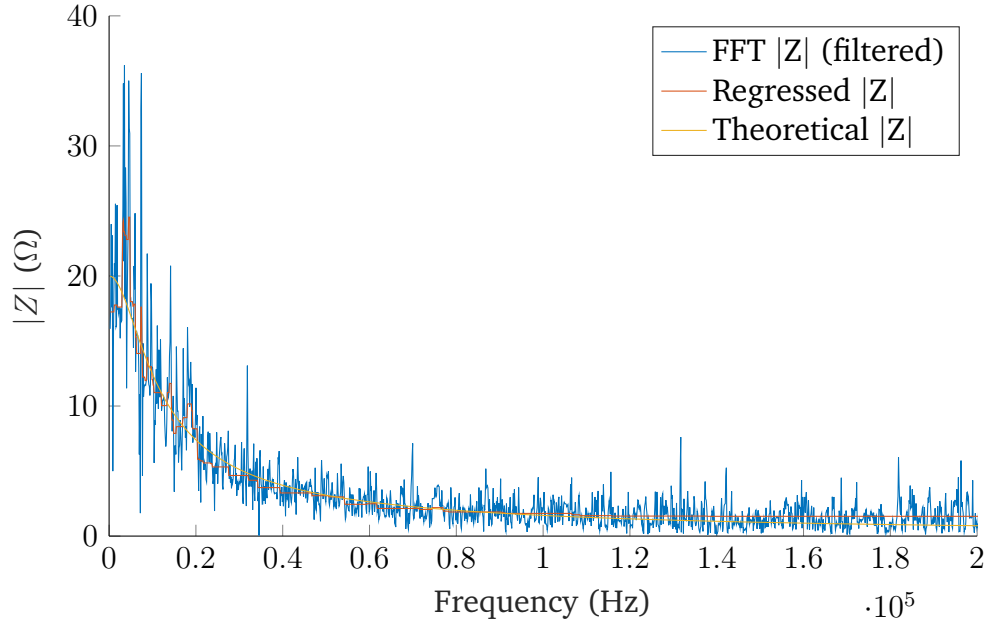


Figure IV.8: Least-squares forest boosting regression of the Hampel-filtered simulated spectrum of a  $20\ \Omega//1\ \mu\text{F}$  R//C load

### IV.3 Experimental results

While the simulations are promising and showcase the ability of the boosting regression to significantly mitigate the effects of noise and uncertainty on the measured impedance magnitude spectra, it is important to validate these results on actual measurements, as the accuracy of a computer model can always be put into question. More specifically, real-life scenarios can contain an endless number of non-idealities and noise sources that cannot necessarily be accounted for in simulations.

Once the manufacturing of the first PCB prototype was complete and the firmware was ironed out, it became possible to perform experimental measurements on some known loads to test the robustness and capabilities of the proposed noise removal routine against more realistic scenarios.

#### IV.3.1 Experimental setup

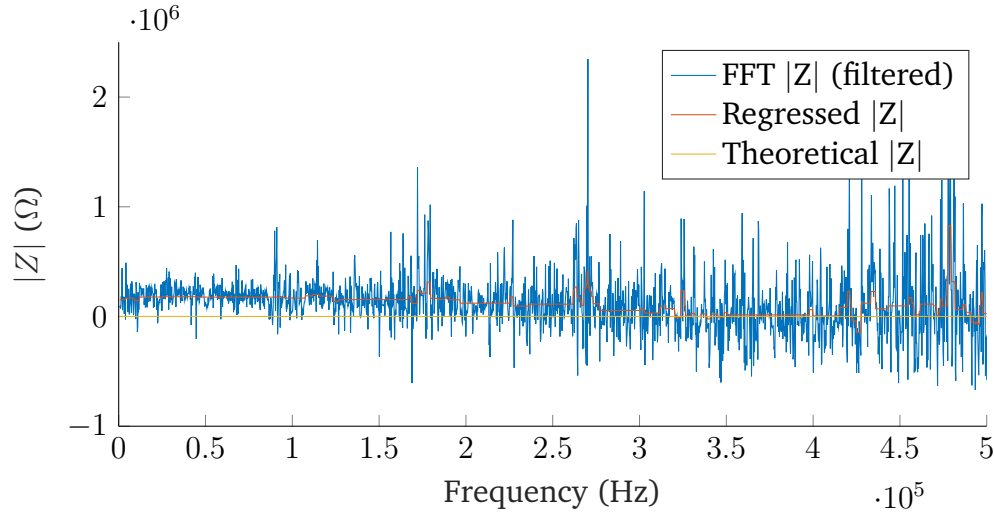
To replicate the simulated tests performed in the previous section, resistive and capacitive decade boxes were connected in parallel to create a tunable R//C dipole, which was connected to the PCB in a four-point measurement configuration. To mitigate interference pickup, all pairs of wires were twisted together whenever possible. Note that the values of the tested impedances were deliberately varied between experiments to validate and showcase the versatility of the noise removal procedure.

Because of a faulty Bluetooth module in the laptop used to retrieve and process measurements, communication with the PCB was established via UART. 5V power

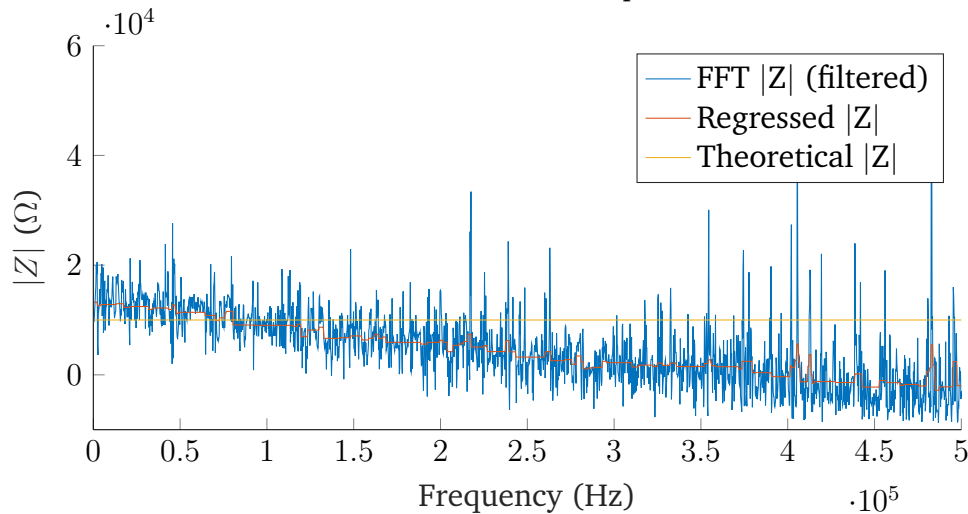
was provided to the PCB by one of the laptop's USB ports.

### IV.3.2 Initial tests and improvements

The first measurements were performed on a few different loads, either purely resistive or in an R//C configuration. The results of the Fourier impedance analysis and attempts at noise removal are shown in Figure IV.9.



(a) 700  $\Omega$ //1 nF R//C dipole

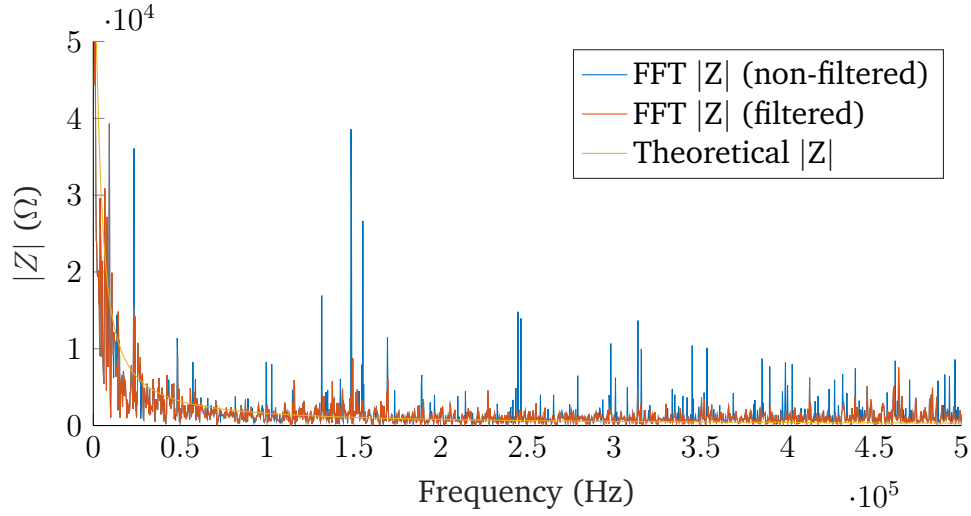


(b) 10 k $\Omega$  resistor

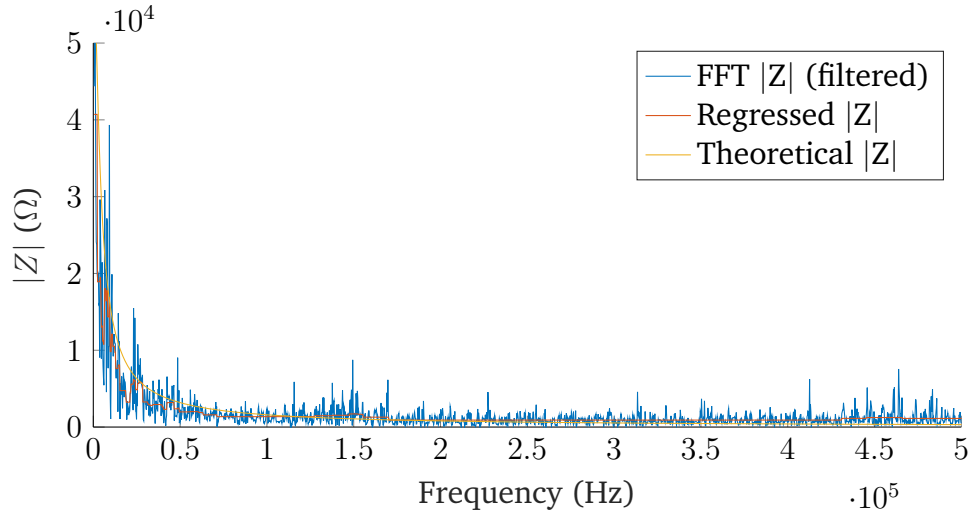
Figure IV.9: Initial signal processing tests on real measured loads

These results were very concerning for the project, as even worst-case simulations severely underestimated the extent of the noise present in the magnitude spectrum of the measured impedances. Looking at the amplitude of the noise and the deviations from the theoretical spectra, obtaining an approximation of the theoretical spectra from the measured ones seem quite utopic.

In an attempt to solve this issue, the experimental setup was moved into a metallic-screened room acting as a large Faraday cage. This was done hoping that the noise was the consequence of electromagnetic interference, picked up somewhere on the PCB. Some impedance spectra reconstructed in this room are given in Figures IV.10 and IV.11.

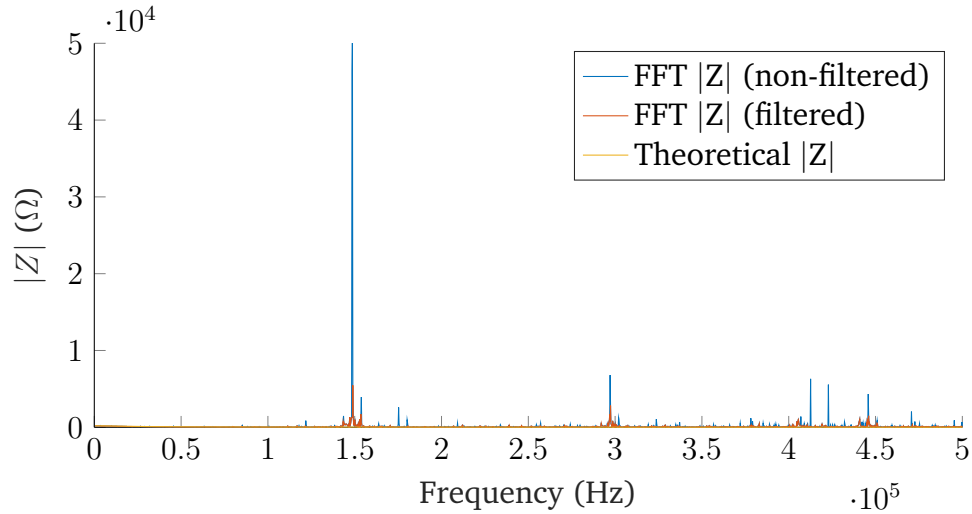


(a) Hampel filtering

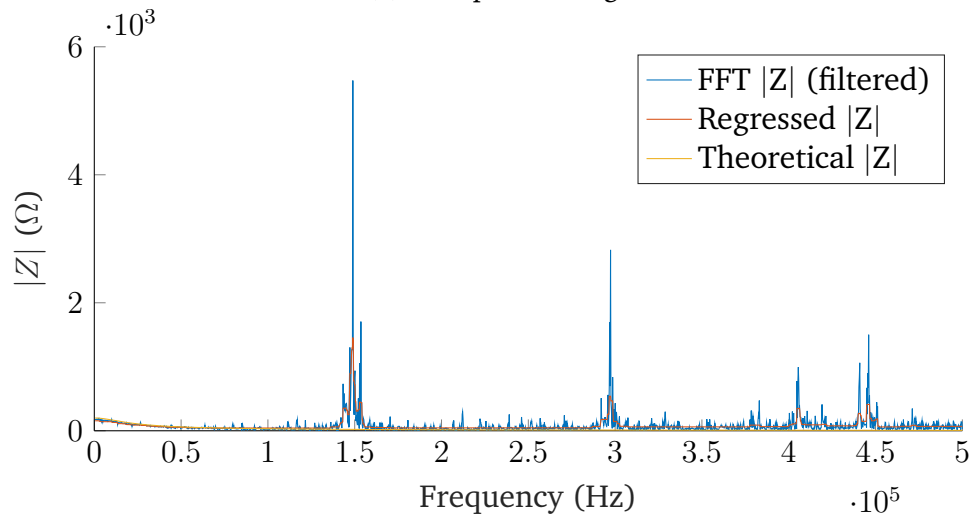


(b) Least-squares boosting regression

Figure IV.10: Processed impedance spectrum of a 60 kΩ//1 nF R/C load measured in a Faraday cage



(a) Hampel filtering



(b) Least-squares boosting regression

Figure IV.11: Processed impedance spectrum of a  $200\ \Omega//50\ \text{nF}$  R/C load measured in a Faraday cage

At first glance, it appears that the hypothesis of EMI pickup was correct and that the PCB would simply need to be shielded to solve these measurement issues. Indeed, the regression algorithm is now able to see through the noise and draw a magnitude spectrum reasonably close to the theoretical ones. Despite the noise seemingly decreasing inside of the Faraday cage, another variable ended up being the actual culprit and was glanced over at this stage. This was however discovered later in the experimental process and will be discussed in due time.

Figure IV.11 brought forward another issue: a prominent peak appears in the impedance spectrum at about 150 kHz, with 300 and 450 kHz harmonics also clearly being present. The issue did not particularly manifest itself in Figure IV.10, because the measured impedance was large and the Hampel filter removed most of it, but

the 150 kHz peak of more than 50 k $\Omega$  completely dwarfs the measured 200  $\Omega$  in the second case.

Analyzing the PCB with a current monitoring device, it was discovered that these peaks were associated with instants of unexpectedly large current consumption which, if left unchecked, would severely decrease the autonomy of the device and put sensitive components at risk of frying.

The cause of these peaks was a resonance phenomenon between an operational amplifier used for setting a voltage reference and capacitors used to stabilize supply voltage. Generally speaking, operational amplifiers are ill-suited to drive large, purely capacitive loads, and can enter a resonance mode. To remedy this issue, the values of the smoothing capacitors were reduced.

New measurements were performed with the newly modified PCB, once again in the Faraday cage. Disappointingly, the very high amplitude broadband noise observed in the initial experiments reappeared in the measurements once more and made it impossible to fit a regression model once again. After recalling the exact setup in which the improved measurements were performed, the real cause of this noise was discovered.

Actually, for the initial measurements and those performed with the modified PCB, the laptop powering the device was itself powered by an AC adapter. However, when the attempt was made to mitigate EMI pickup by moving the experimental setup into a shielded room, the laptop was left on battery power. This detail was crucial, as the real reason for the disappearance of noise was the use of a pure DC power source in the form of a battery to power the PCB, instead of a transformer converting the power line voltage into DC. The circuit was always designed to operate on a DC voltage source, which explains why it behaved badly when exposed to the noise of transformers and switching power supplies.

Powering the PCB directly via a lithium battery, most of the noise issues were thankfully gone, even outside of a Faraday cage, as shown by the results presented in Figures IV.12 and IV.13. These measurements still display a concerning resonance behavior at 250 kHz, which was fixed by removing all smoothing capacitors connected to the operational amplifier producing the voltage difference.

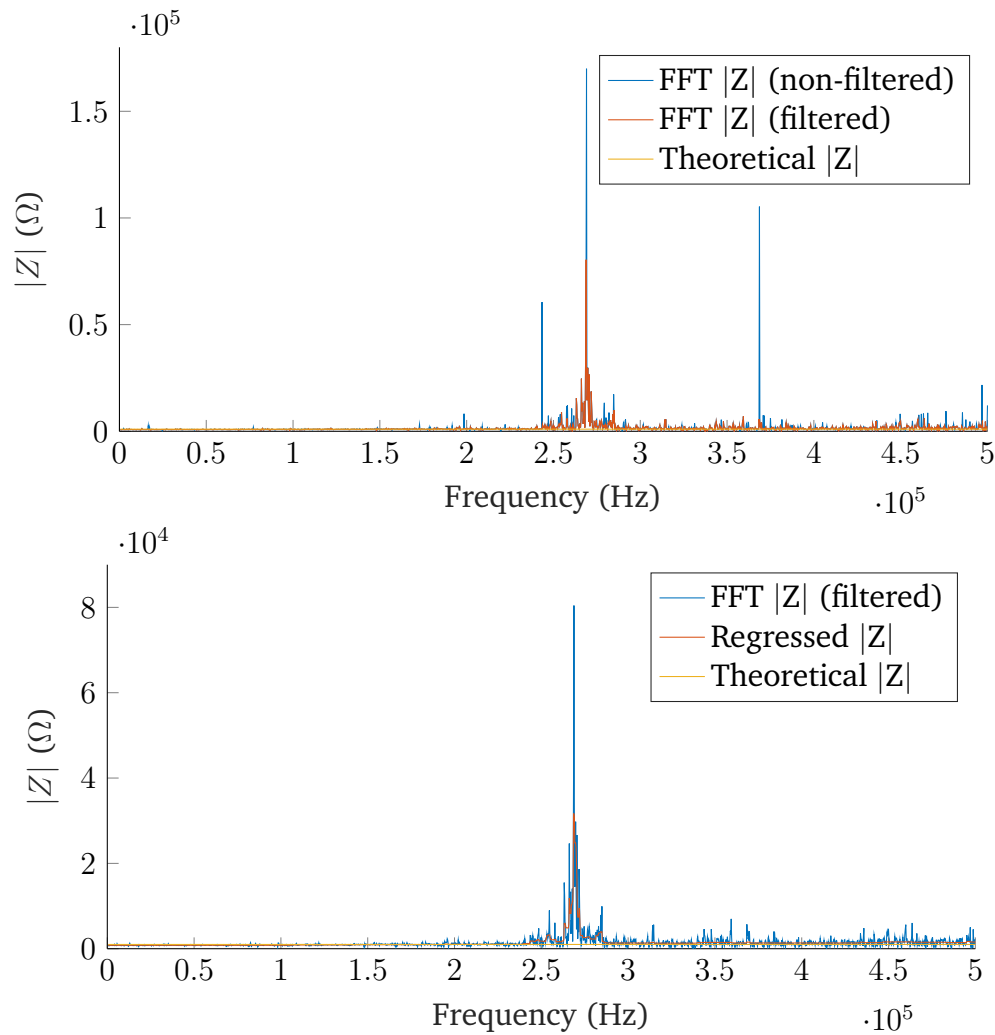


Figure IV.12: Processed impedance spectrum of a 1 kΩ resistive load measured with a battery-powered PCB

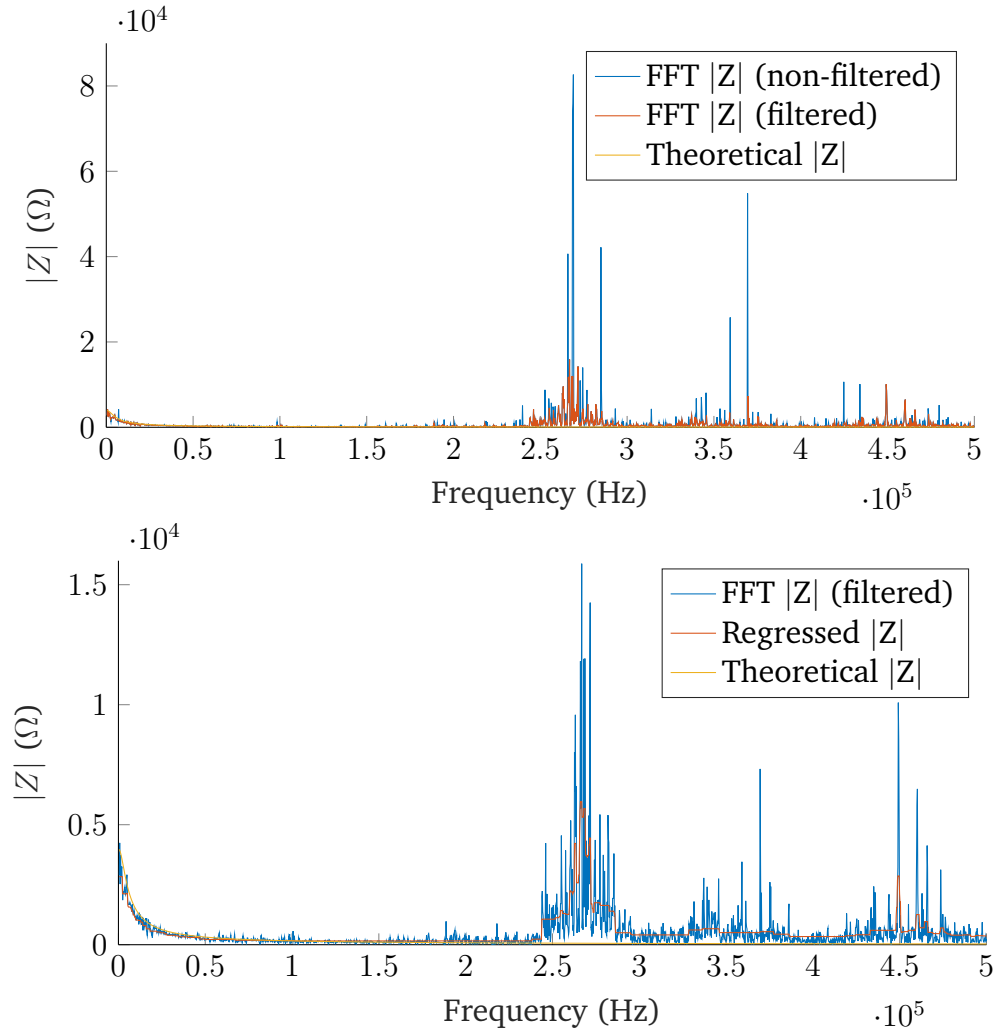


Figure IV.13: Processed impedance spectrum of a 4 kΩ//10 nF R//C load measured with a battery-powered PCB

Figure IV.14 shows the final results that were obtained after eliminating the resonance peaks from the measurements. These are a huge step up compared to the first measurements, but they are still far from perfect. Notably, some unexplained low-frequency attenuation is very apparent, leading to systematic errors of 10 to 20% in the evaluation of the impedance values from the regressed spectra.

Unfortunately, after several months of delay in the PCB manufacturing process, the improvements documented here are all that could be done before the time allocated to this thesis ran out. With more work and experiments, it should hopefully be possible to sort out that unwanted attenuation and potentially reduce the noise levels as well, to make good enough measurements for bioimpedance spectroscopy.

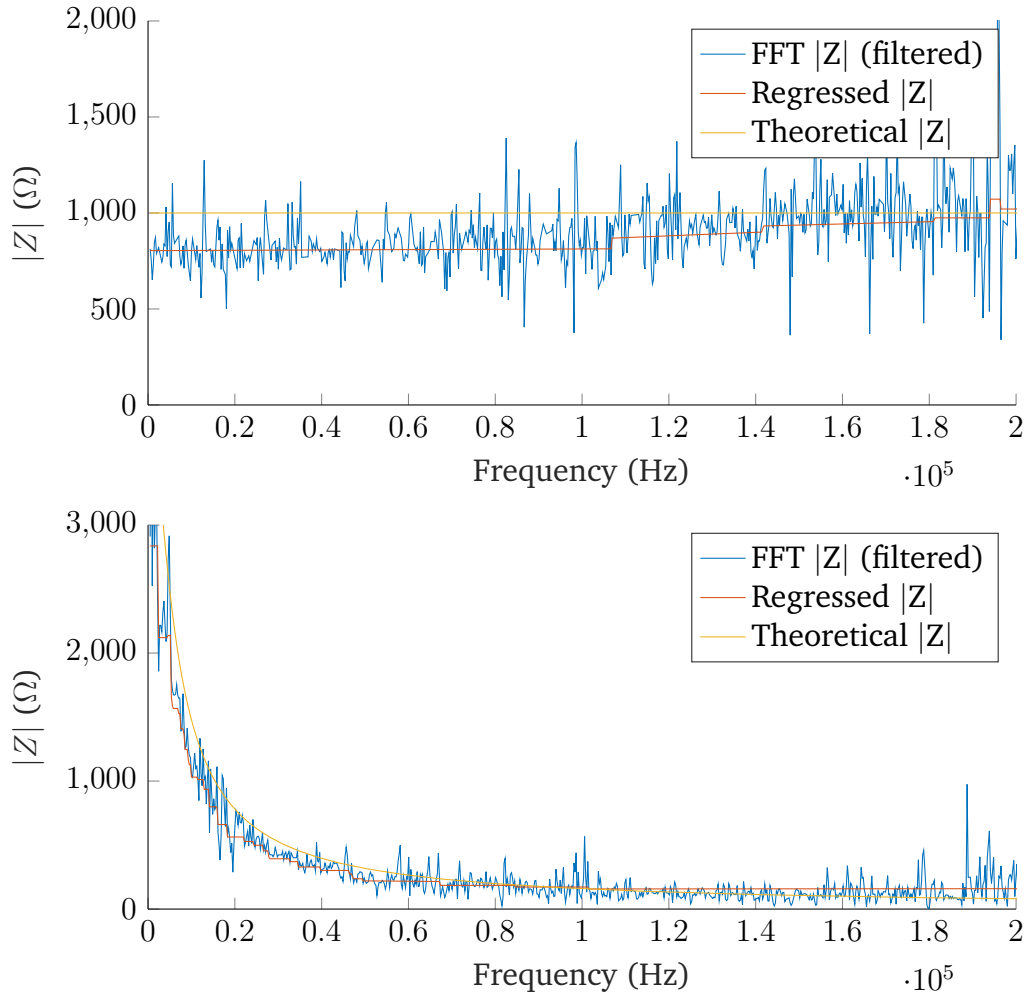


Figure IV.14: Zoom on the processed impedance spectra measured with a battery-powered PCB, from 0 to 200 kHz



## Part V

# Image reconstruction algorithms and methods

The next big objective of this project is the reconstruction of images of wounds from the non-invasive bioimpedance spectroscopy measurements described in the previous parts. The process of reconstructing images from a volume using measurements from the outside is called tomography and is a staple of medical imaging. Tomography requires knowledge about the physical processes involved in the measurements, and algorithms to infer the volume composition from the data acquired non-invasively.

While researching plausible techniques for evolving bioimpedance spectroscopy into image reconstruction, the concept of electrical impedance tomography was stumbled upon. This family of tomographic reconstruction algorithms seemed promising, as it precisely solves the problems that the Vitapatch project is trying to tackle. Hence, this image reconstruction technique quickly became the main focus for the rest of this work.

In this fifth part, the basics of medical tomographic imaging are described. Namely, the measurement methods and concepts used for the traditional computed tomography (*CT*) are briefly presented. Differences between x-rays and electric currents are pointed out, and the cousin of CT, electrical impedance tomography (*EIT*), which deals specifically with imaging based on electrical measurements, is introduced. The mathematical formulation, numerical methods, imaging modalities, and electrode arrangement for EIT are all discussed. EIT algorithms are presented and compared thanks to EIDORS, an EIT reconstruction software. Finally, a basic application of EIT is carried out to evaluate the capabilities of EIDORS in real scenarios.

## V.1 Principles of tomographic imaging and EIT

### V.1.1 Traditional tomographic imaging

Tomography refers to imaging techniques used to reconstruct images of the volume of an object using measurements acquired from the outside of this object. In the medical imaging domain, tomographic imaging is a widespread examination used for diagnosing or screening various conditions in several parts of the body. Computed tomography, or CT, also referred to as CT scan (or simply *scanner* in French), uses x-ray beams sent through the part of the body of interest, and arrays of x-ray receptors placed on the other side of the body to measure the intensity of the beam after going through the tissues. This way, the attenuation caused by the tissues can be measured. Measurements are performed by rotating the x-ray emitter and sensors around the patient's body, to perform measurements at various angles.

To reconstruct images, x-rays are assumed to travel in straight lines, which can be mostly guaranteed by using collimators. This way, all the measured attenuation characteristics can be assumed to belong to a single cross-sectional slice of the body, in the plane where the x-rays traveled.

Clearly, some parallels can be drawn between CT and bioimpedance measurements. The analogy between injected currents and x-rays traveling in the body holds well, as tissue-dependent absorption of radiations and heterogeneous resistivity distribution in tissues can be seen as similar reconstruction targets. Instead of measuring the attenuation of electric energy, impedance tomography is concerned with voltages along the imaged volume, which are nothing but another form of indication of the impedance of surrounding tissues under a certain current.

Despite these similarities, a major difference exists between CT and EIT, which explains why the former is a widespread technique, while the latter is confined to some niche uses in the medical world. Unlike x-rays, currents cannot be assumed to travel in straight lines at all. As shown in Figure V.1, current lines curve and spread in the body in which they are injected. This greatly complicates image reconstruction algorithms, as the path of injected currents has to be determined according to a conductivity distribution to make sense of the voltage measurements. Nevertheless, solutions for solving the EIT image reconstruction problems exist, and are explored in the next sections.

### V.1.2 Concepts of electrical impedance tomography

Electrical impedance tomography (*EIT*) is an imaging technique that aims at reconstructing the conductivity distribution of an object by means of external, non-invasive current injections and voltage measurements. In that sense, it is a natural extension of bioimpedance spectroscopy. This technique has found some uses in the medical domain, but its applications are still sparse, and it is still an active area of research.

As described in Part I, the electrical properties of skin and tissues are diverse,

which implies a heterogeneous distribution of conductivity and permittivity within the imaging body. Based on a continuous expression of Ohm's law in a volume, EIT algorithms are implemented to construct an image of that conductivity distribution based on voltage measurements.

Specialized algorithms are required to reconstruct images based on electrical currents, as they do not travel in a straight line in any material. This is in contrast with radiographic imaging, which uses the attenuation of straight-traveling x-rays to create images of a volume.

The following sections are derived from introductions to electrical impedance tomography by Lionheart [24], Adler and Boyle [37], Malone [57], and Adler and Lionheart [58].

#### **V.1.2.1 Mathematical formulation of the EIT reconstruction problem**

From a mathematical point of view, EIT is separated into two problems: the forward problem, and the inverse problem. The goal of the forward problem is to determine an electrical potential distribution inside a body of known conductivity, using boundary conditions to find a unique solution. The inverse problem, which is the image reconstruction problem, aims at reconstructing the conductivity distribution in a body from boundary conditions. Whereas a unique solution can generally be found for the forward problem, the inverse problem is severely ill-posed and requires a Bayesian approach, regularization, and iterative algorithms to be solved adequately.

The most common application of EIT starts with some sort of cylindrical body, electrically insulated from the outside, with conductive electrodes at the periphery. Currents are injected via one pair of electrodes at a time, while the other pairs of electrodes measure voltages. This procedure is illustrated in Figure V.1.

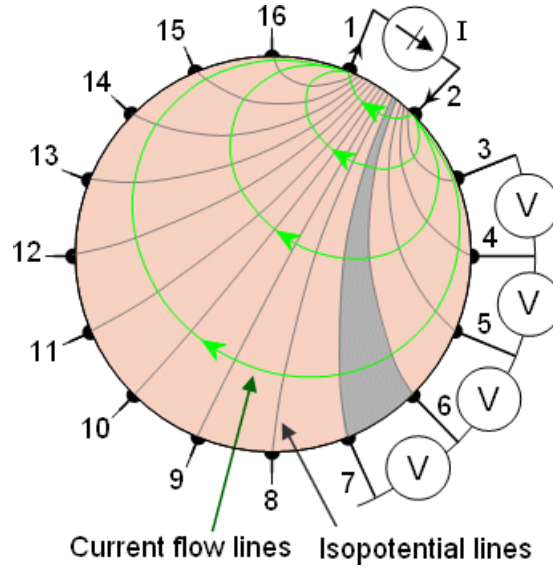


Figure V.1: General concept of electrical impedance tomography, with current flow lines and the resulting orthogonal isopotential lines (from [59])

**a) Forward problem** For electrical safety and physiological reasons mentioned in Section II.1.3, alternating currents are used for EIT on living tissues. The mathematical formulation of the forward EIT problem relies on the frequency of these currents being low enough for magnetic effects to be negligible, which simplifies Maxwell's equations and allows a quasi-static formulation of the problem to be derived. For now, assume a purely resistive body is studied.

Let  $\Omega$  be the imaging volume,  $\partial\Omega$  its boundary, and  $u(\mathbf{x})$  the scalar electric potential field within the volume. The electric field  $\mathbf{E}$  ( $\text{V m}^{-1}$ ) corresponding to this electric potential is given by

$$\mathbf{E} = -\nabla u \quad (\text{V.1})$$

In the absence of internal current sources, the electric current density  $\mathbf{J}$  ( $\text{A/m}^2$ ) satisfies

$$\mathbf{J} = \sigma \mathbf{E} = -\sigma \nabla u \quad (\text{V.2})$$

with the conductivity distribution  $\sigma(\mathbf{x})$  in the volume. This is the continuous 3D version of Ohm's law.

Kirchhoff's current law for current conservation in a volume writes as

$$\nabla \cdot \mathbf{J} = 0 \quad (\text{V.3})$$

once again in the absence of internal current sources.

Together, (V.2) and (V.3) yield

$$\nabla \cdot (\sigma \nabla u) = 0 \quad (\text{V.4})$$

This second order partial differential equation, which reduces to the Laplace equation for  $\sigma = 1$ , is the basis of the EIT forward problem. For a biological tissue, which is not purely resistive as explained in Section 1.2, the conductivity of materials needs to be generalized as the admittivity  $\gamma(\mathbf{x}, \omega) = \sigma(\mathbf{x}) + j\omega\varepsilon(\mathbf{x})$ , with  $\varepsilon$  the material permittivity. Thankfully, the development using complex numbers and fields lead to the same equation as (V.4) with the admittivity instead of the conductivity [57]:

$$\nabla \cdot (\gamma \nabla u) = 0 \quad (\text{V.5})$$

To find a unique solution to the forward problem, boundary conditions are required. These can either take the form of Dirichlet conditions  $u|_{\partial\Lambda}$  or Neumann conditions  $-\sigma \nabla u \cdot \mathbf{n} = -\mathbf{J} \cdot \mathbf{n}$ , where  $\mathbf{n}$  is the outward normal to the boundary  $\partial\Omega$ . In other words, Neumann boundary conditions refer to the currents injected into the volume, which is known at each electrode. Everywhere else on the boundary, there is simply no injected current density.

Aside from the Neumann boundary conditions everywhere on the boundary, a zero potential point (i.e. a ground point) has to be arbitrarily chosen in the volume to give the problem a unique solution.

Solving the forward problem provides valuable information for image reconstruction: conceptually, this step defines the relationship between a change in conductivity anywhere inside the body and the corresponding change in potential in the body, including at the boundaries where voltages are measured. Hence, an image reconstruction problem for EIT always requires the use of a forward model to establish this relationship.

This reasoning highlights the importance of creating an accurate geometric model of the measurement setup. In practice, small errors in the electrode placements or the shape of the body can have drastic consequences on image quality. For a better representation of the experimental conditions, advanced EIT techniques take the contact impedance between the electrodes and the body into account. An EIT problem using the contact impedance as well as the dimensions of the electrodes (as opposed to considering point electrodes) is said to use a complete electrode model (CEM).

**b) Inverse problem** The inverse problem of electrical impedance tomography consists in computing a plausible conductivity distribution for an object based on voltage measurements at its periphery during current injections. This problem is in essence the image reconstruction problem.

By using the sensitivity map defined by the forward model which relates a change in voltage at the boundary to a change in conductivity inside the body, and a Neumann-to-Dirichlet map which transforms the current injection boundary conditions into electric potential boundary conditions, EIT algorithms are able to estimate the conductivity distribution of the imaging body.

The inverse EIT problem is severely ill-posed, mainly because its solution is theoretically not unique, and does not depend continuously on the measured data as a small change in measured voltage can be related to an arbitrary change in conductivity anywhere in the body. Therefore, this problem requires regularization. In most cases, this regularization is brought by a prior estimation of the conductivity distribution.

The exact workings of the inverse problem solving will not be detailed here, as they are the subjects of entire books and theses. The description of the concepts of sensitivity map, forward model, Neumann and Dirichlet conditions, and the general reconstruction idea is sufficient to understand, compare and analyze the different reconstruction methods and algorithms available today. All these algorithms strive to minimize an objective function derived from the likelihood of a conductivity distribution based on the sensitivity map, measurements, and regularization method.

### V.1.2.2 Numerical methods

To reconstruct images in EIT, numerical methods are almost always required. This necessity stems from the fact that the forward problem can only be solved analytically for simple and symmetric geometries. When attempting to create models representing real scenarios with complex shapes and discontinuous conductivity distributions, it is necessary to turn to finite element methods (*FEM*).

FEM relies on a discretization of the domain  $\Omega$  into a finite number of 3D elements and nodes, on which the partial differential equations are solved. For this reason, forward models are generally created using meshing software, which creates a 3D representation of desired shapes and domains made up of irregular polyhedra. In the case of the forward EIT problem, the potential  $u$  is computed on each node of the model.

In a finite element problem, the sensitivity map can be written as a sensitivity matrix, also called Jacobian. Each entry of this matrix relates a change in one of the measurements to a change in conductivity of an element of the mesh.

To solve the inverse problem, numerical methods are also at play. Most algorithms used nowadays are based on an iterative minimization of an objective function. The most widely adopted technique for EIT is based on the Gauss-Newton algorithm<sup>1</sup>. Despite the prevalence of this technique, several variants exist and mainly differ based on the regularization techniques used. Concrete examples will be explored later.

At this point, an important remark needs to be made. Because of the dependence between every element of the volume in the reconstruction process, EIT is, despite its name, not a true *tomographic* imaging technique, in the sense that it is unable to reconstruct image slices independently. This is of course once again due to the fact that currents travel in all dimensions, as opposed to x-rays used in computed tomography.

---

<sup>1</sup>Wikipedia. *Gauss-Newton algorithm*. URL: [https://en.wikipedia.org/wiki/Gauss%E2%80%9993Newton\\_algorithm](https://en.wikipedia.org/wiki/Gauss%E2%80%9993Newton_algorithm) (visited on 07/21/2022).

However, the moving current injection source and the voltage measurements around the imaging body are reminiscent of a CT sequence, hence the name.

### V.1.2.3 Electrode patterns

A typical EIT system generally uses a ring of 8, 16, or 32 electrodes on a single plane. With this amount of electrodes, there are several ways of injecting currents and measuring the resulting voltages. In EIT literature, several current and voltage patterns are defined. In this section,  $N$  refers to the number of electrodes.

The first EIT systems used the adjacent pattern for currents and voltages. In this pattern, illustrated in Figure V.2a, a current is injected between adjacent pairs of electrodes, and the voltages are recorded between all other pairs of electrodes at the same time. This leads to  $N$  different current injection pairs, and  $N - 3$  voltage measurements per current injection, for a total of  $N(N - 3)$  measurements to reconstruct an image. This pattern is not commonly used anymore, as it suffers from a lack of sensitivity in the center of the domain. Indeed, most of the current injected between two adjacent electrodes will travel near the boundary, and only a few current lines will cross the center of the object.

To circumvent the lack of sensitivity in the center of the domain, newer EIT systems use an opposite current injection pattern illustrated in Figure V.2b, where current is injected between electrodes on either side of the electrode ring, greatly increasing the likelihood of current passing through the center of the imaging body. This injection pattern is however not optimal either, because of the symmetry of current injections. Indeed, for  $N = 8$ , injecting a current between electrodes 1 and 5 or between electrodes 5 and 1 will lead to the exact same voltage measurements in absolute value. This means that only  $\frac{N}{2}$  independent current injections are possible, with  $(N - 4)$  voltage measurements per injection and a total of  $\frac{N(N-4)}{2}$ . Similarly, opposite voltage measurements could be considered but would drive the number of measurements to  $\frac{N(N-2)}{4}$ .

A possibility for increasing the number of independent measurements while maintaining good sensitivity in the center of the object is to use a "just-off" opposite injection pattern. Despite its apparent benefits, it is still seldom used in EIT literature.

For traditional EIT geometries and applications, the opposite injection pattern has proven to be more effective than the adjacent one, despite the decreased amount of information collected. However, this might not necessarily hold for the low-currents, high-impedance EIT measurements that are envisioned for this project, especially considering the potential differences in geometry and the complexity and heterogeneity of human tissues. This question will be revisited in due time.

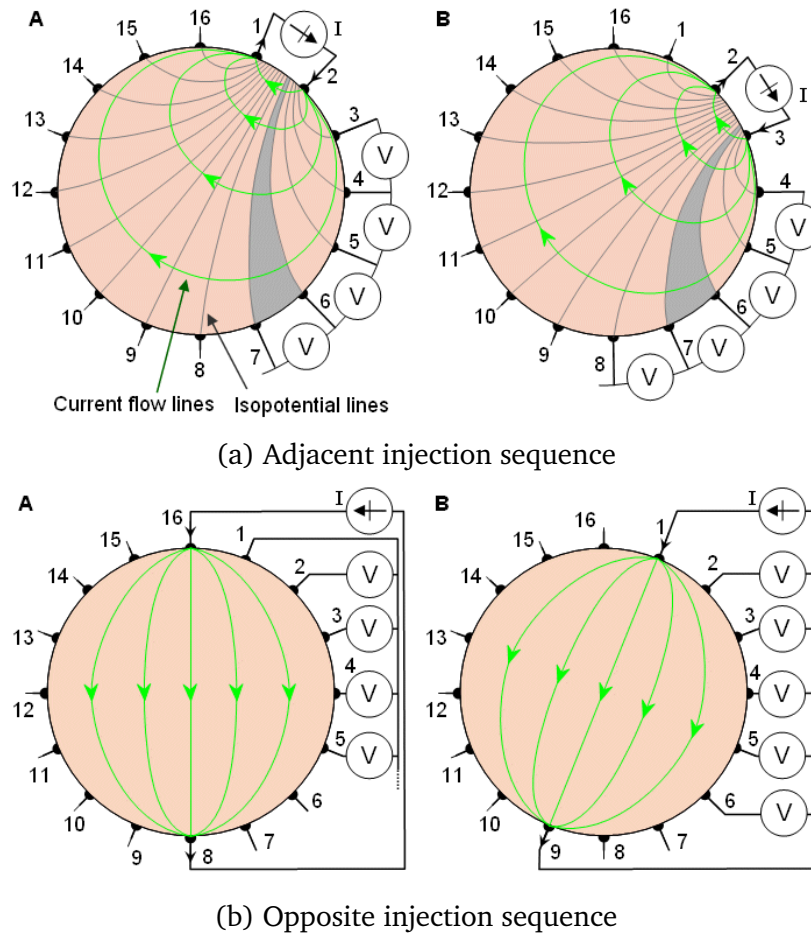


Figure V.2: Illustration of adjacent and opposite injection patterns with adjacent measurements (from [59])

#### V.1.2.4 Imaging modalities

Historically, EIT algorithms were made to create a map of conductivity changes between two measurements. The reason is that, as mentioned previously, the EIT reconstruction problem is very sensitive to small changes, measurement errors, or modeling inaccuracies. By performing a differential image reconstruction, most of these errors and the resulting inaccuracies cancel out.

The first EIT imaging modality is time-difference imaging. This modality is dynamic and qualitative, as it compares two measurements performed at different times and highlights small and localized changes in conductivity. This modality has some medical applications, for functional imaging of lung movement for example. However, it lacks the ability to provide diagnostic images for detecting anomalies, such as brain tumors, aneurysms, or, in our case, open wounds. Indeed, to do so, a background measurement of a healthy situation would be required. Unfortunately, due to the sensitivity of these imaging techniques to modeling errors, creating a generalized baseline for any body part is simply not feasible.



To remedy the shortcomings of time-difference imaging and allow for static measurements, multiple approaches have been developed, the first of which is an absolute reconstruction algorithm. Absolute EIT promises a quantitative image of the conductivity of an object, using a single measurement. Nowadays, absolute reconstruction is possible and provides promising results for imaging an anomaly without prior information or measurements, but the nonlinear and complex nature of the reconstruction problem means that the resulting images are more prone to noise and errors, and thus generally display poorer quality compared to time-difference images. Absolute EIT algorithms are also generally slower, as they require solving more complex problems.

An alternative to absolute imaging that still allows for a static measurement while keeping some of the advantages of time-difference imaging is frequency-difference EIT. Instead of acquiring data at two different times and looking for changes in conductivity between the two measurement instants, frequency-difference imaging uses measurements acquired with two different excitation frequencies. Frequency-difference EIT therefore evaluates the frequency dependence in conductivity and the capacitive part of the impedance of the imaging body.

For tissue imaging and wound monitoring, these three modalities can all be considered in some way.

Obviously, if achievable, absolute imaging would be the ideal solution for wound assessment, as it would enable diagnostic imaging without any sort of calibration or baselining necessary. Its ability to reconstruct images in the context of wound monitoring would nevertheless need to be assessed to ensure that the complexity of the conductivity distribution and the eventual sources of noise would not result in a failure.

The other natural candidate is frequency difference imaging. Supposedly, damage to the external layers of the skin should change its frequency-dependent behavior (as explained in Section 1.3), and therefore allow the use of this imaging modality. Once again, experiments are required to validate the potency of this method, as the change in behavior may or may not be significant enough to lead to good imaging using EIT. Finally, "time"-difference EIT should not be ruled out, as two methods could allow purely differential image reconstruction to be performed. First, one could imagine a calibration step, which would consist in performing a first measurement on a healthy portion of the skin as a baseline, before moving the electrodes to the wound. The success of this method lies in the ability to find a comparable portion of skin for baselining and to maintain geometric accuracy across all measurements. Second, difference EIT could be used to assess wound *healing*, by observing the progressive decrease in conductivity at the periphery of the wound while it heals. This method is not suitable for assessment of the wound as it would require days between measurements to observe a difference but could be an interesting secondary application nonetheless. Note that, in both cases, displacement of the electrodes between measurements could completely invalidate the reconstruction process, as the imaging bodies of both measurements would differ.

## V.2 Electrical impedance tomography algorithms

### V.2.1 The EIDORS software

To perform electrical impedance tomography simulations and image reconstructions, this project relies on the *Electrical Impedance Tomography and Diffuse Optical Tomography Reconstruction Software*, or *EIDORS* [58]. This open-source software is presented as a MATLAB library and provides free algorithms and tools for forward and inverse modeling for EIT. EIDORS has been in constant development and improvement for nearly two decades and is a convenient and powerful solution to tackle electrical impedance tomography problems.

As the manufacturing of the prototype measurement PCB was delayed by several months, the simulation capabilities of EIDORS offered a chance at trying out different image reconstruction algorithms on suitable models and exploring the potential uses of EIT for wound imaging. EIDORS is bundled with the Netgen FEM meshing software, allowing the creation of complex and relevant models for simulation and reconstruction.

EIDORS is not necessarily easy to apprehend for advanced problems, as its documentation is mostly based on simple examples, and the descriptions of functions and data structures can be a bit scarce. After experimenting with the basics for a while, and a lot of trial and error, it is nevertheless possible to create advanced and interesting simulations. A full code example for simulating measurements and reconstructing images is given and commented on in Appendix B. This code corresponds to simulations performed in Part VI.

### V.2.2 Gauss-Newton algorithms

The Gauss-Newton algorithm is the most widely used algorithm to approximate the solution of the inverse EIT problem [57, 58]. In EIDORS, this algorithm is implemented and ready to use with a variety of parameters and regularization techniques.

#### V.2.2.1 Principles

Because the inverse problem of EIT is highly non-linear and ill-posed, one can only hope to approximate a solution via numerical algorithms. The Gauss-Newton algorithm is an iterative method aimed at solving multidimensional non-linear least squares problems. For inverse EIT, this algorithm is used to minimize the difference between the predicted data and the measured data [61]. More specifically, this method aims at minimizing the quadratic norm of the difference between the predicted voltage measurements according to the estimated conductivity distribution and the forward map, and the actual voltage measurements.

To perform time or frequency-difference imaging, predicted and measured changes in conductivity and voltages are compared instead.

The Gauss-Newton algorithm is an iterative algorithm, which decreases the value

of the objective function at each iteration. For electrical impedance tomography, most applications are however satisfied by performing a single iteration of the minimization algorithm, which is then referred to as a one-step Gauss-Newton reconstruction. Indeed, in generic reconstruction problems, the first step of the algorithm reduces the value of the objective function by around 80%, while further iterations only shave off a further 5 to 10% of the original value [62].

### V.2.2.2 Available priors

As mentioned several times already, the inverse EIT problem is ill-posed. Conditions for a mathematical problem to be well-posed are the following [57, 61]:

- For any given input data, a solution exists,
- This solution is unique, and
- The solution is stable, i.e. it depends continuously on changes in the input.

Because a change in measured voltage at one electrode could be linked to a conductivity change anywhere in the body, a solution to the inverse EIT problem is generally not unique nor stable.

To remedy the ill-posedness of the problem and allow the Gauss-Newton algorithm to a unique solution, the objective function contains a regularization term, a function of the predicted conductivity that compares it to à priori information. Numerous types of à priori information, called priors, can be used to regularize EIT problems depending on the need of the application. Certain types will favor smooth solutions, others will allow sharp changes, and some will prefer sparse solutions, ... Some well-established priors available in EIDORS are briefly presented below.

**a) Tikhonov prior** The Tikhonov regularization is historically the most frequently used regularization method for ill-posed mathematical problems [63]. A zeroth-order Tikhonov prior steers the reconstruction problem towards small solutions and limits high oscillations. For EIT image reconstruction, this prior will therefore tend to create images with small conductivity changes (for difference imaging) and a smooth conductivity distribution in space [57]. Because spatial smoothing is not desired to identify objects in EIT, other priors are generally preferred.

**b) Laplace prior** The Laplace prior is the default prior for image reconstruction in EIDORS and is generally referred to as a second-order high-pass filter. It tends to ignore small conductivity changes between elements and prioritizes sparse solutions with well-defined objects in space [61, 64].

**c) NOSER prior** The NOSER prior, for Newton's One Step Error Reconstruction, assumes a constant conductivity distribution as an initial guess and constrains the solution where sensitivity is the highest, i.e. closer to the electrodes. By the admission of the creators of this method themselves, this prior tends to limit the accuracy of the

reconstructed conductivity distribution in terms of conductivity values, but has the advantage of providing useful medical images as geometric features are typically well reproduced. [65]

**d) Total Variation prior** The total variation prior has been developed as a more suitable alternative to other priors for several fields such as medical imaging. Compared to other priors, it does not impose a penalty for the non-smoothness of the obtained solutions, and therefore allows discontinuous domains to be preserved in reconstructed images [66]. The general idea behind this prior is the use of a  $l_1$  norm for regularization, instead of the more usual  $l_2$  norm. The  $l_1$  norm is generally recognized as being more likely to produce sparse solutions because it uses absolute values instead of squaring a difference to keep it positive<sup>2</sup>.

### V.2.3 The Graz consensus algorithm

The Graz consensus Reconstruction algorithm for Electrical Impedance Tomography (GREIT) [68] is a novel reconstruction algorithm imagined by a consensus of experts for the fields of EIT and medical imaging in Graz, Austria. Their goal was to create a new reconstruction method suited specifically for medical imaging, to avoid relying on legacy, proprietary algorithms using techniques and constraints that generally did not make sense for clinical applications (such as most of the regularization techniques presented previously).

The Graz consensus defined multiple *figures of merit* to evaluate the performance of a medical image reconstruction algorithm. These are

- The amplitude, or value of the reconstructed conductivity change,
- The position error, to evaluate the spatial accuracy of the reconstructed image,
- The resolution, the smallest volume conductivity change that can be reconstructed,
- The shape deformation, which compares the shapes of the reconstructed and imaged objects and,
- Ringing, which is the amount of noise appearing around the reconstructed objects, typically in the form of rings.

Just like other methods, the GREIT algorithm uses a forward FEM model for simulating currents and voltages in a given conductivity distribution. Where it deviates from older EIT algorithms is in its image reconstruction phase. Instead of using a prior conductivity distribution and minimizing an objective function, the GREIT algorithm creates a set of training samples using the forward model and uses the figures of merit defined above to create "desired" images from these samples. Noisy measurements on the training samples are simulated, and a reconstruction strategy is created around

---

<sup>2</sup>Abhimanyu Dubey on Quora. *When would you chose L1-norm over L2-norm?* 2016. URL: <https://www.quora.com/When-would-you-chose-L1-norm-over-L2-norm> (visited on 08/18/2022).

the desired images and training simulations. The exact mathematical process is too complicated to explain in this thesis, but the most important detail to keep in mind is that GREIT relies on training examples and figures of merit that can respectively be tuned to resemble expected measurements and preferred image characteristics.

Because the GREIT algorithm was imagined for applications in lung imaging and breathing analysis, it is only capable of performing difference imaging. It relies on a 3D forward model of traditional EIT geometries and reconstructs a 2D image of conductivity changes.

## V.2.4 Comparison of available EIT algorithms

With the variety of available algorithms and priors for EIT image reconstruction, it is important to identify each one's strengths and weaknesses and find the most promising candidates for an application to wound imaging. In the following, several simulations and image reconstructions are performed to observe the qualities of each algorithm on relevant examples.

### V.2.4.1 Simulation setup

**a) Finite-element geometry** To simulate voltage measurements and reconstruct images in EIDORS, finite-element models are required. For this algorithm comparison section, the traditional cylindrical EIT geometry is used. To make the model closer to a situation of non-invasive measurements from the skin of a patient, the electrodes were placed at the periphery of the top surface of the model, rather than on the sides. For these first simulations, 1D point electrodes are used for simplicity. The cylindrical body has a radius of 5 cm and a height of 2 cm. These dimensions are generous compared to the size of an ulcer, but the goal here is to study the behavior of different algorithms without running into issues regarding mesh generation and lengthy computations. The finite-element model generated via Netgen is represented in Figure V.3.

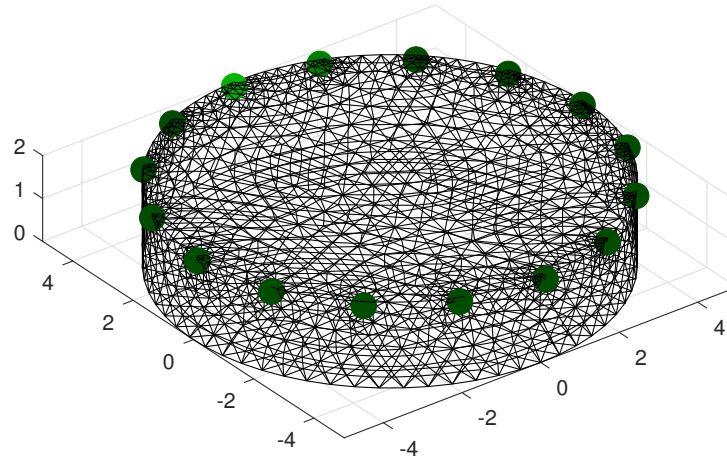


Figure V.3: Finite element model of a cylindrical conductive body used for algorithm comparison, with boundary point electrodes at the top (in green) (dimensions in cm)

**b) Imaged objects** To create a very simple model of a plausible wound-like object within the imaging body, a half-ellipsoid target with a higher conductivity than the rest of the body was placed in the forward models. The flat side of the object was placed right at the top surface of the body, to mimic the decrease in top layer resistance observable on wounded human skin.

The choice of an elliptic object was done for several reasons. First, the horizontal asymmetry will highlight the (in)ability of an algorithm to recreate the shape of the object at the surface, in the horizontal plane of the electrodes, accurately. Indeed, as will be seen later, not all algorithms can make out the details of an object and will tend to assume a symmetric or circular object when it is not the case. Second, this shape will allow the assessment of the vertical resolution of each algorithm. Because electrodes are only placed at the top of the model, they have access to limited information about the shape of the object beneath the surface and its depth within the body. Some algorithms will therefore potentially behave better than others in that regard, and reconstruct a more faithful 3D shape.

To evaluate the sensitivity of the algorithms on the horizontal plane, two sets of simulations are performed, one with the object placed in the center of the body, and the other with it placed on one side. These two situations, represented in Figures V.4a and V.5a, are useful to assess the accuracy of the image reconstructions on the entire plane since some algorithms will fare better with objects placed in the center of the body, while others will manage a decent image even when the object is placed closer to some electrodes.

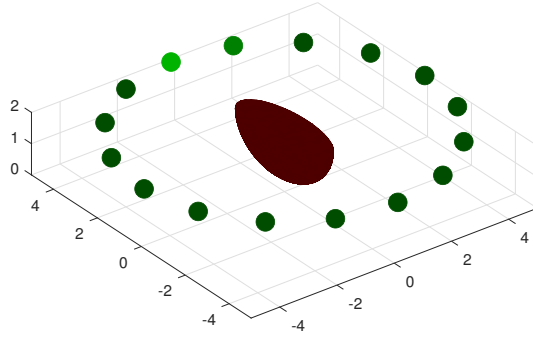
**c) Injection and measurement patterns** To comply with the objectives of the Vitapatch project, 16 electrodes were specified on the model. For these initial simulations, difference imaging between a homogeneous model and the same model with the added elliptic objects was simulated. Because it is known to work better on traditional EIT geometries such as this one, the opposite current injection pattern was

used, with adjacent voltage measurements. Absolute imaging of the object was also attempted.

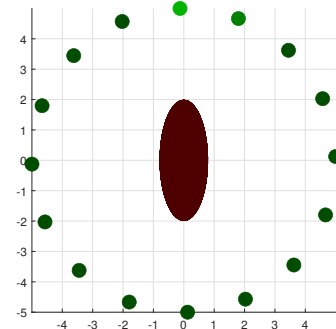
#### **V.2.4.2 Results**

The One-step Gauss-Newton algorithm was tested using the Laplace, NOSER, and Total Variation priors for difference imaging. The GREIT algorithm was also tested, using the default tuning hyperparameters. Finally, a NOSER absolute reconstruction, which performs multiple iterations of the Gauss-Newton algorithm, was also used. Results are showcased in Figures V.4 to V.8.

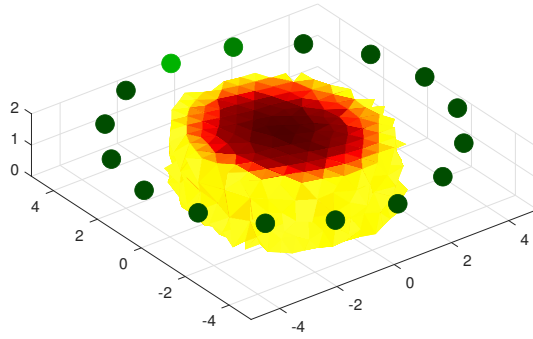
The color convention for all of the electrical impedance tomography reconstructed images in this work is that the warmest colors represent the highest conductivity values in the image, while colder colors are areas of lower conductivity.



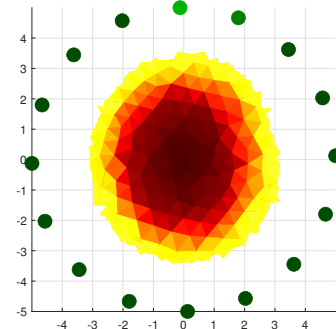
(a) Simulation model : centered half ellipsoid conductive object



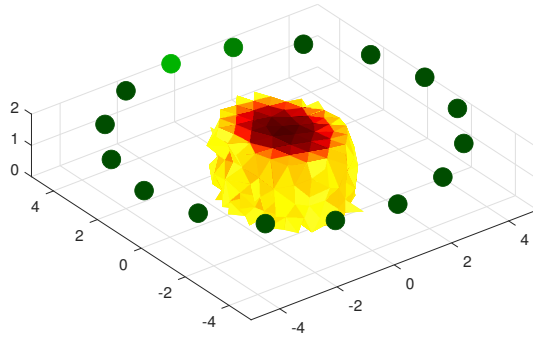
(b) Top view of the simulation model



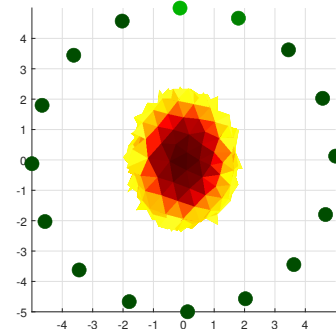
(c) Reconstructed object with a Laplace prior



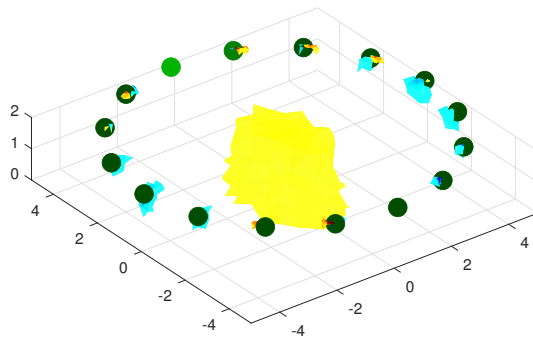
(d) Top view of the Laplace reconstruction



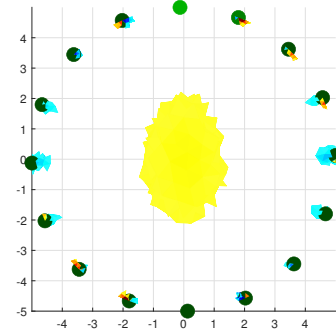
(e) Reconstructed object with a NOSER prior



(f) Top view of the NOSER reconstruction



(g) Reconstructed object with a Total Variation prior



(h) Top view of the Total Variation reconstruction

Figure V.4: Comparison of Gauss-Newton difference EIT reconstruction priors for a centered object



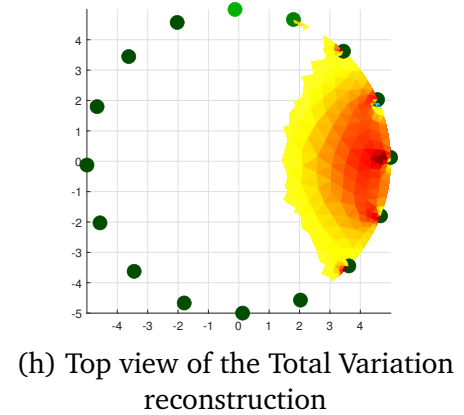
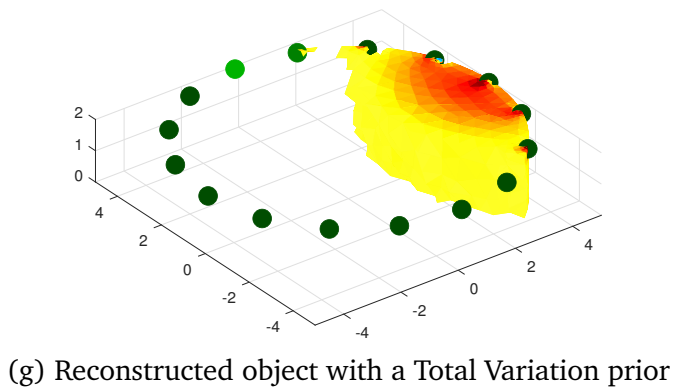
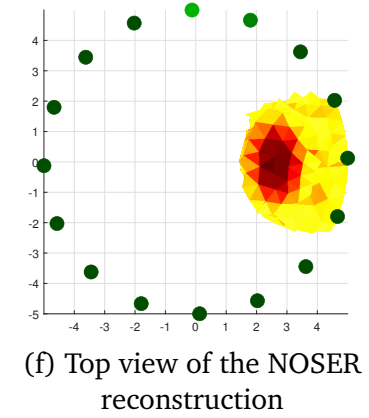
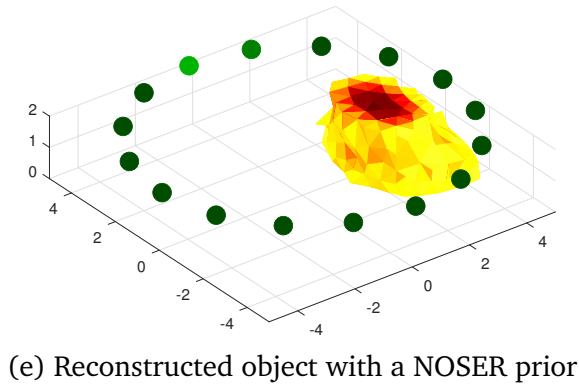
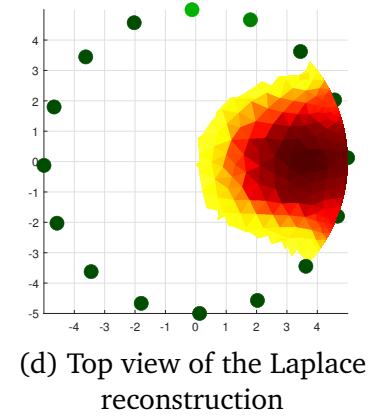
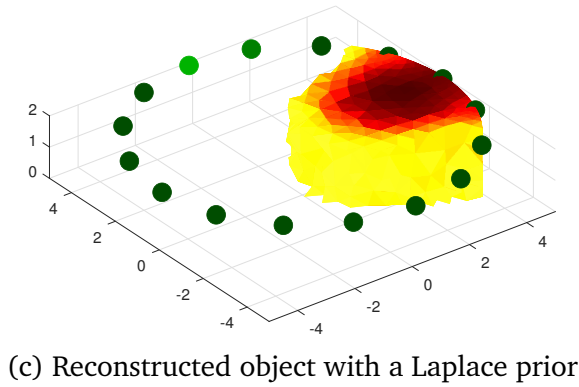
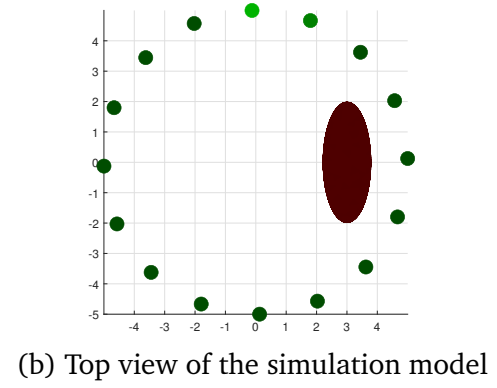
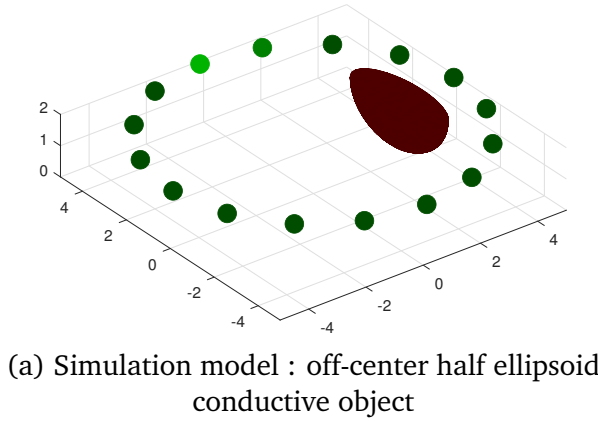


Figure V.5: Comparison of Gauss-Newton difference EIT reconstruction priors for an off-center object

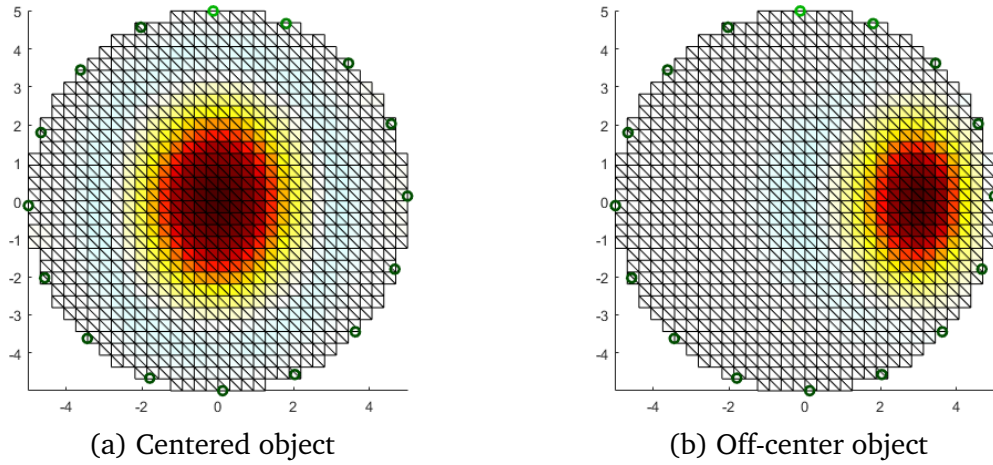


Figure V.6: GREIT reconstruction of the two conductive targets used for algorithm comparison

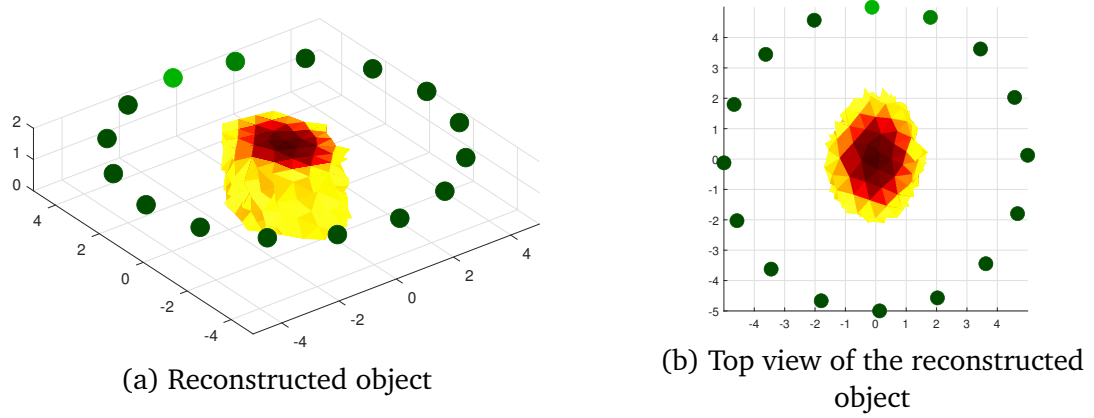


Figure V.7: Absolute Gauss-Newton EIT reconstruction with NOSER prior for the centered object

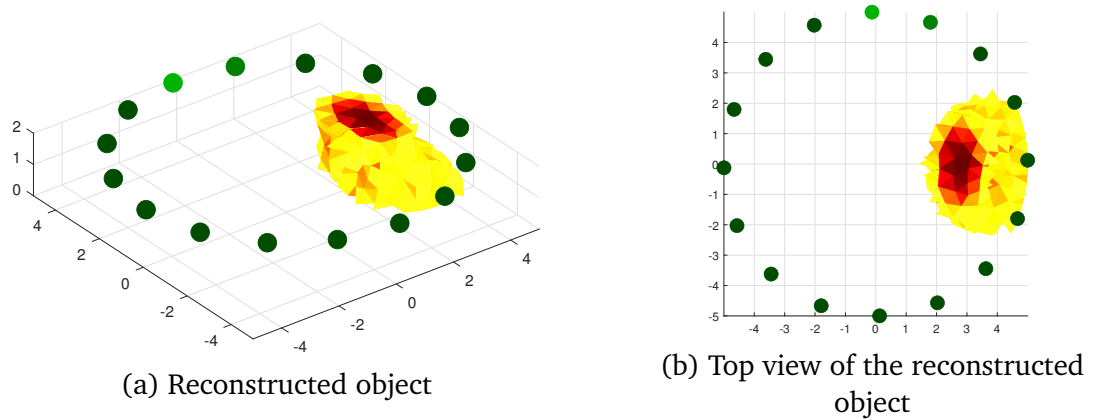


Figure V.8: Absolute Gauss-Newton EIT reconstruction with NOSER prior for the off-center object

These simulations allow two algorithms to stand out. The first is the Gauss-Newton reconstruction with NOSER prior. In both cases, it was able to create a faithful image of the top slice of the imaged object, respecting its shape and dimensions well compared to the other priors. The Laplace prior showed poor spatial accuracy in both reconstruction scenarios, while the Total Variation prior looked promising in the case of the centered object, producing arguably the closest and cleanest image of the conductive target. However, it completely fails to reiterate that success for the off-center object, faring no better than the Laplace prior. The results of Figure V.5 show how important the high sensitivity near the electrodes provided by the NOSER prior is, as all other algorithms are negatively influenced by the proximity between the target and the electrodes and produce images stretched to the boundaries of the model. The absolute reconstruction attempts using the NOSER prior on these simple problems perform about as well as the difference imaging, which is a pleasant finding that implies that such a technique might be viable for diagnostic imaging.

The second algorithm to stand out is the GREIT algorithm. Its 2D reconstruction is not a particular disadvantage compared to the Gauss-Newton algorithm either. Indeed, all the reconstructions of Figures V.4, V.5, V.7 and V.8 display no vertical sensitivity whatsoever, which was expected due to the positioning of the electrodes. The 3D reconstructed shapes are nothing but vertically spread out equivalents of the reconstructed shape of the object at the surface. The GREIT algorithm produces fairly accurate images of the shapes of the conductive objects, and only minor ringing artifacts can be observed. In both cases, the images produced by this algorithm are quite satisfactory, although one might argue that the off-center object is reconstructed even more precisely, which may indicate that the areas of highest sensitivity of this algorithm lie closer to the electrodes.

### V.3 Preliminary application: object imaging in aqueous medium

To better grasp the concepts and utilization of electrical impedance tomography algorithms before moving on to the challenge of wound imaging, a preliminary application of EIDORS to real measurements was explored.

The goal was to use a commercially available EIT kit, the [SPECTRA kit](#) sold by Mindseye Biomedical, and their [OpenEIT](#) software platform to perform traditional EIT measurements, and exploit EIDORS to test the performance of the algorithms in a practical scenario. Besides getting more familiar with EIDORS and observing its reconstruction capabilities on real data, the motivation behind this application also stemmed from manufacturing delays of the Vitapatch PCB.

The kit contains a SPECTRA PCB, built to perform bioimpedance spectroscopy and single-frequency EIT, and different sets of electrodes. For this experiment, a flex array of electrodes placed into a circular plexiglass tank, mimicking basic EIT geometries, will be used.

The OpenEIT platform is a Python-based, open-source software running as a local server on a computer. It communicates via UART with the SPECTRA board to control its functions and receive the voltage measurements. OpenEIT also features image reconstruction capabilities directly within its interface. This feature is based on [pyEIT](#), a Python framework for electrical impedance tomography [69]. Compared to EIDORS, pyEIT is still in its infancy, and the version used by OpenEIT lacks many features, the most important being 3D meshing. As a consequence, the images obtained via this method are rather lacking compared to what EIDORS is capable of delivering, as will be shown later.

### V.3.1 Experimental setup

The plexiglass tank was used as the imaging volume for this first application. The electrodes were placed at the bottom of the tank and held in place with double-sided tape, making sure to avoid creating wrinkles or creases in the flex cable to make the electrode array as circular and symmetrical as possible. The tank was filled with tap water up to 20 mm to create a homogeneous conductive background.

As for the object to image, a machined iron piece provided by Microsys was placed inside of the tank, in two different orientations shown in Figure V.9. Time-difference imaging was performed, by first measuring the conductivity distribution of the water only, before placing the metal piece in the tank.

For image reconstruction with EIDORS, a 3D finite-element model of the tank was generated, using the physical dimensions of the tank and specifying 1D point electrodes near the bottom of the tank. This model is shown in Figure V.10. The current injection pattern used by the SPECTRA is not specified on their website nor on OpenEIT. Thankfully, as the data export function of OpenEIT provides 192 measurements at a time in the 16-electrode mode, it can be deduced that it uses an opposite injection pattern with adjacent voltage measurements (which leads to  $N(N - 4)$  measurements as explained in Section V.1.2.3).

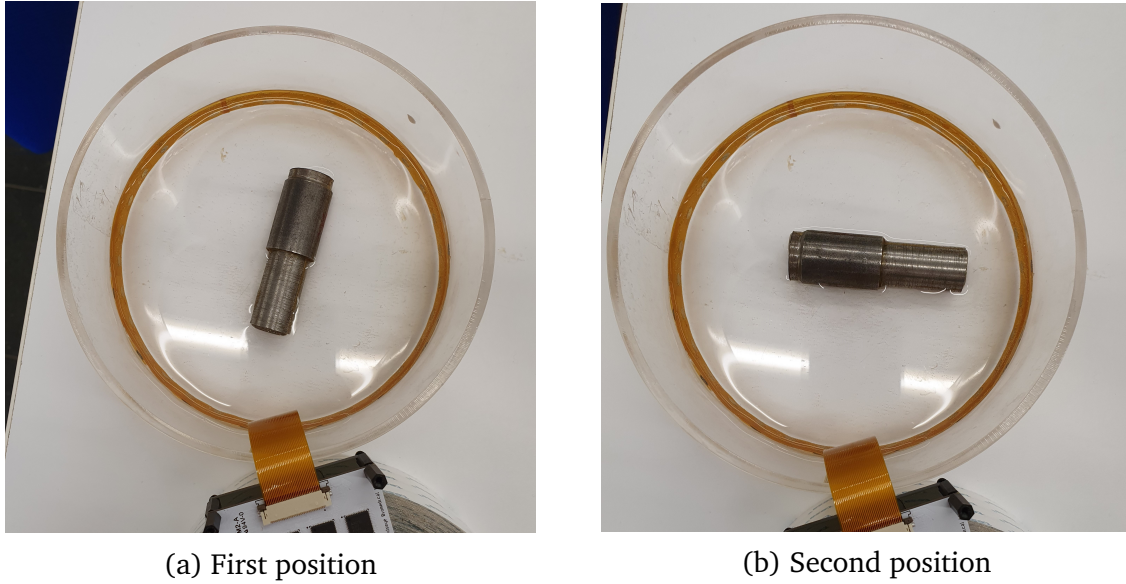


Figure V.9: Metal piece immersed in the SPECTRA electrode tank filled with tap water

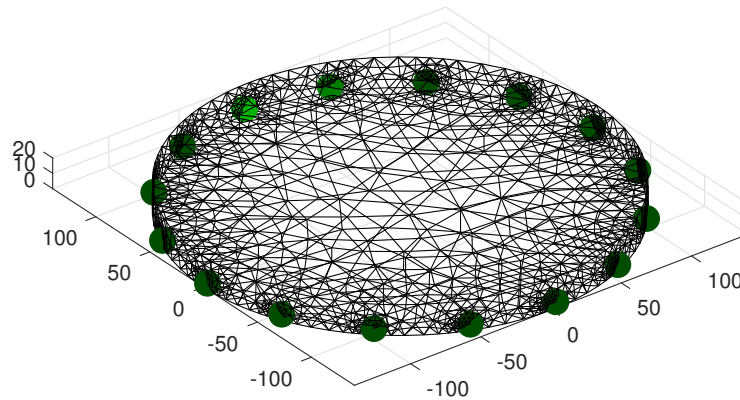


Figure V.10: 3D FEM model of the SPECTRA EIT tank using point electrodes (in green) (dimensions in mm)

### V.3.2 Results

OpenEIT provides three different algorithms for image reconstruction: a backprojection, a Jacobian method (which is another name for One-step Gauss-Newton reconstruction with a NOSER prior [64]), and a GREIT reconstruction. Disappointingly, neither the backprojection nor the Jacobian method led to any exploitable image. The GREIT reconstruction was the only type of algorithm leading to a somewhat plausible image. OpenEIT image reconstruction results are shown in Figure V.11.

These results are frankly disappointing, as they barely showcase the orientation of the metal piece in the tank. Image resolution is severely lacking to make out any details about the object, and there is practically no contrast in the conductivity

changes shown in the longitudinal axis of the piece, with the blue area spreading between the two edges of the image.

The measurement data used to reconstruct these images was retrieved from OpenEIT, converted into the right format, and imported into MATLAB for use with EIDORS. The GREIT algorithm was trained on the tank model shown in Figure V.10, and the resulting image reconstructions are shown in Figure V.12.

These images are definitely not perfect reconstructions of the objects, as the boundaries are not exact and the images show some noise around the objects, but they are still far superior to the results obtained by OpenEIT. This positive result concludes this first part on electrical impedance tomography and motivates a continuation of the use of EIDORS as a framework for EIT applied to imaging of open wounds.

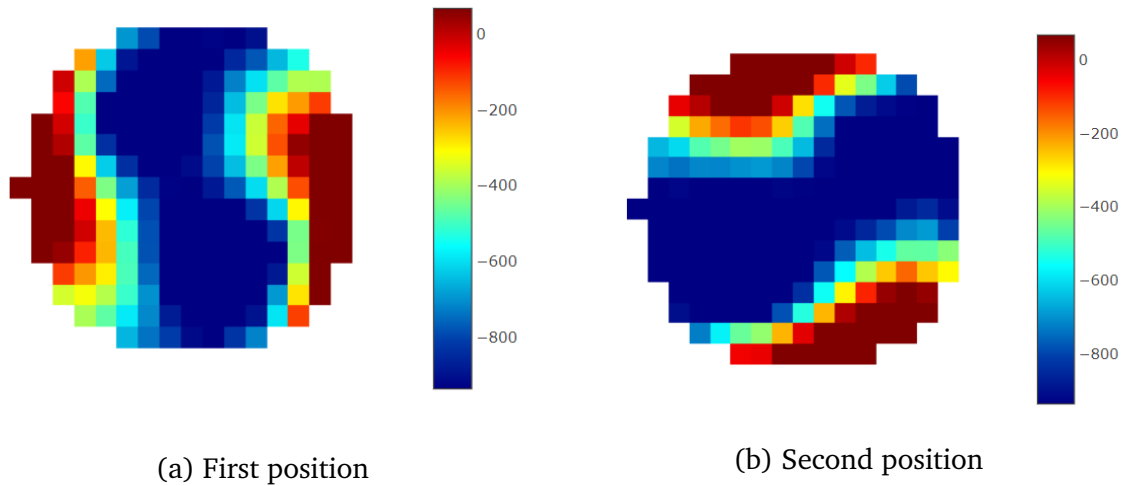


Figure V.11: OpenEIT image reconstruction of the metal pieces of fig. V.9 using the built-in GREIT algorithm

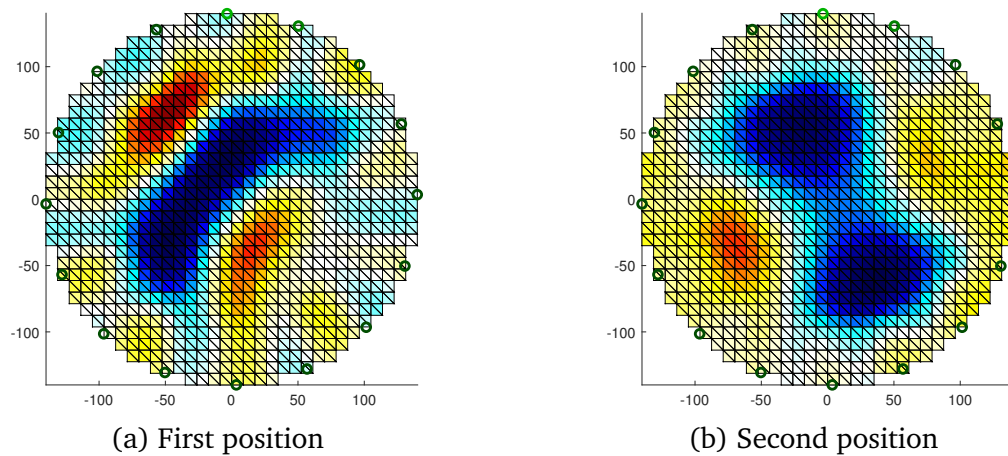


Figure V.12: EIDORS image reconstruction of the metal pieces of fig. V.9 using a tuned GREIT algorithm (dimensions in mm)

## Part VI

# Electrical impedance tomography applied to wound imaging

In Part V, EIT simulations and experiments have been carried out in traditional EIT geometries. These geometries consist of a conductive body delimited by electrodes placed at its boundaries. The volume delimited by the electrodes is thus assumed to be electrically insulated from the outside.

However, when looking at the geometry of the application planned for the Vitapatch project, assuming that the electrodes are delimiting a closed and isolated 3D volume appears unreasonable, as the skin spans on the inside of the electrode ring just like it does on the outside.

In this sixth part, modifications of the traditional EIT geometry and workflow to conform to the reality of skin measurements are explored. A finite-element model of the layers of the skin usable for EIT simulations is then presented. The effectiveness of current injection patterns is reevaluated on the new geometry after some interesting simulation results. After finding the solution to a bug in EIDORS, realistic simulations of EIT reconstruction for a wound integrated into the skin FEM model are presented. Finally, the performances of EIDORS are evaluated in terms of computation times.

## VI.1 Adaptation of the reconstruction problem

This section will explore how the reconstruction problem can be modified to comply with the geometry of the Vitapatch application. For this, a circular ring of 16 electrodes is envisioned to be placed around the wound. It was decided to fix the diameter of this ring to 6 cm, and to consider circular electrodes of 9 mm in diameter.



### VI.1.1 Inadequacy of traditional EIT geometries

So far, the geometries used for simulating and testing EIT have consisted of cylindrical bodies delimited by a ring of electrodes. At first glance, one might not think twice and believe that such a model would be suitable to represent a ring of electrodes placed on a relatively flat portion of skin, as is the aim of the Vitapatch project. However, in the case of electrodes placed anywhere on a human body, nothing guarantees that the currents injected for EIT measurements will be confined to the inside of the electrode ring.

Currents flowing outside of the cylindrical volume defined by the electrodes would violate the current conservation inside the imaging body, which is a basic hypothesis of the mathematical formulation of EIT (section V.1.2.1) and completely compromise image reconstruction. Boundary conditions would also naturally be incorrect.

Ideally, the current should only travel on the inside of the electrode ring. If it occurs that only a negligible fraction of the current finds its way outside of the ring, the boundary conditions could still hold up to some degree of approximation, and reconstruction could still succeed. This situation appears rather unlikely to occur in practice, especially for adjacent current injections, as there is no reason for the current to only spread on the inside of the ring if the skin conductivity is the same on both sides. However, opposite injection patterns might lead to suitable results.

To evaluate the extent of the problem, a simulation of current injections via an electrode ring on a large surface can be carried out. Depending on the outcome, some actions may need to be taken to ensure the success of image reconstruction. To that end, current propagation simulations can be set up on the COMSOL Multiphysics FEM simulation software.

Figure VI.1 showcases the results of a 3D steady-state simulation of alternating electric currents in a cylindrical portion of skin with a ring of 16 electrodes on top of it. The material used for the main cylindrical body is "Human skin" in COMSOL, which uses low-frequency conductivity and permittivity values of bulk skin similar to those presented in Section I.2.3.1. The electrodes were set to the properties of gold, and the highest contact impedance supported by the COMSOL solver of  $3 \times 10^{-4} \Omega\text{m}^2$  was set between the electrodes and the skin. One electrode was set as a terminal onto which an injected current can be specified, and another was set as a ground for the return current. The current was set to  $10 \mu\text{A}$  to comply with the Vitapatch PCB, and both adjacent and opposite injection patterns were tested.

The simulated path of the current lines confirms the inadequacy of using a cylinder model delimited by the electrodes to represent current flows in the skin because a non-negligible portion of the injected current ends up traveling outside of the electrode ring. Not only that, but these simulations also highlight another significant phenomenon that had not been anticipated. Indeed, it appears that the electrodes used for voltage measurements, that are still present on the skin at all times despite not being used for current injection, have a significant influence on the path taken by the current. Despite their relatively high contact impedance with the skin, the



electrodes themselves appear to represent a path of least impedance for the current, thanks to their high conductivity as a metal. Because of that, many current lines are being channeled by the electrodes, and a large part of the current injected is traveling on the circumference of the electrode array.

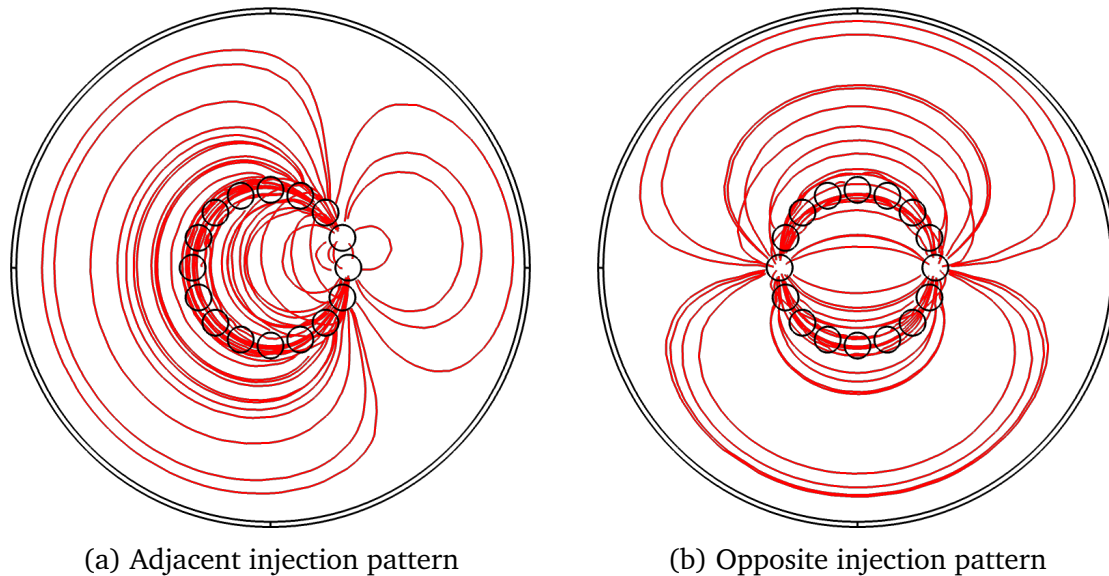


Figure VI.1: Qualitative COMSOL simulations of current propagation in a cylinder of skin with a ring of electrodes

Despite making the model much larger than the ring of electrodes, current lines are still going up to the boundaries of the cylindrical system. This is an inevitable limitation of FEM modeling using simple geometries, but it still proves that currents are traveling far outside of the electrode ring. This may cause an issue when transitioning from well-delimited FEM models to actual measurements on the skin, but it is impossible to confine all current lines within a closed volume when that current is free to spread in the entire body. The expected effect on reconstructed images is unwanted artifacts at the border of the models, but, granted that these borders are far from the conductivity distribution of interest (the wounds in this case), this should not represent a serious issue. One potential solution to this problem could be to use guard electrodes<sup>1</sup> to limit the spread of current to a known volume, but this goes beyond the scope of this project.

Aside from confirming that more accurate models are required for surface EIT, these COMSOL simulations have brought forward a potentially interesting observation for the rest of the project. Because of the channeling effect causing current lines

<sup>1</sup>The Photon (<https://electronics.stackexchange.com/users/6334/the-photon>). *Implementing guard trace/ring in PCB design.* Electrical Engineering Stack Exchange. URL: <https://electronics.stackexchange.com/q/24890> (version: 2012-01-11). eprint: <https://electronics.stackexchange.com/q/24890>. URL: <https://electronics.stackexchange.com/q/24890>.

traveling between the two injection electrodes to tend to conform to the shape of the electrode ring, the efficiency of both current injection patterns could need to be re-evaluated for a surface electrode ring configuration.

Indeed, in Figure VI.1a, the current lines inside of the ring appear as circular arcs of increasing radius from the right to the left of the image. As a consequence, the entire interior of the electrode ring is being swept by currents, which means sensitivity across the entire interior volume could be better than anticipated.

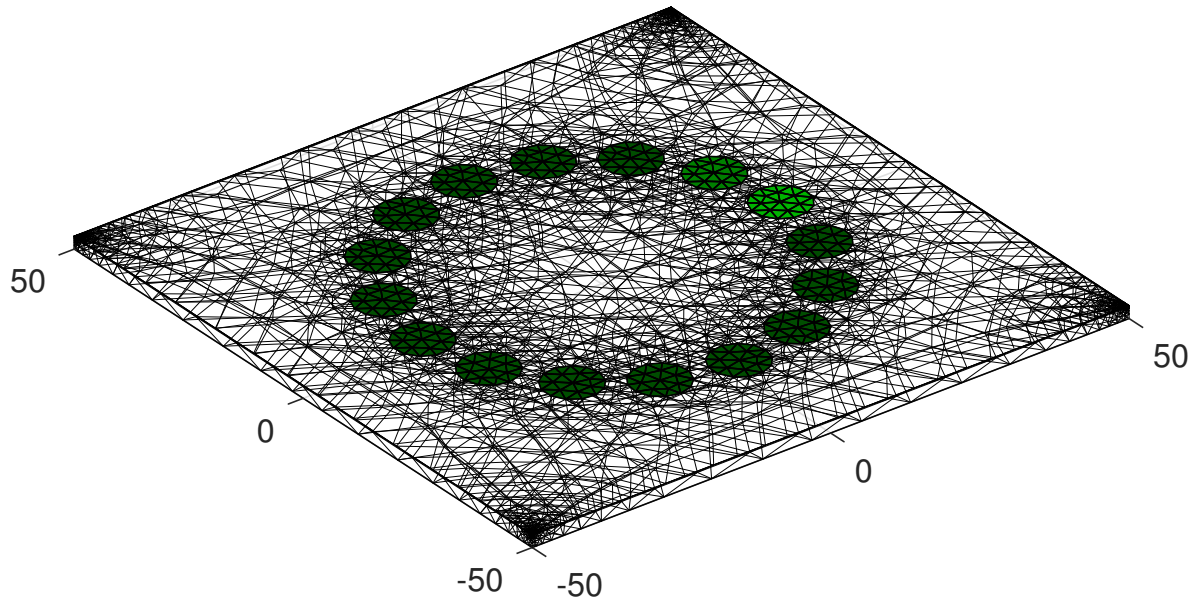
By contrast, Figure VI.1b shows that the progressive arcing of the current lines towards the electrodes may leave the center of the ring without much current going through it, potentially starving the image reconstruction algorithms of data regarding the center of the volume. This observation will motivate a reassessment of the two injection methods using comparative simulations of image reconstructions on this kind of geometry.

### VI.1.2 Skin EIT experimental model

Thankfully, extensions of the EIT problem exist to properly simulate and reconstruct images from geometries that consist of an electrode array placed at the surface of a conductive body.

The need for such geometries historically comes from geophysical applications of EIT, where electrodes are placed on the surface of the earth to measure the composition of the soil and detect objects underneath [58]. EIDORS includes models that represent geophysical applications and can take into account current propagation from electrodes placed on a flat surface anywhere in a body. Importantly, the channeling of the current lines by the path of least impedance provided by the electrodes themselves should be properly simulated and accounted for in the reconstruction, preventing the electrodes from appearing on top of the reconstructed image.

With simple trigonometry, it is possible to specify the positions of each electrode such that they are arranged in a circle in the EIDORS models. Additionally, the model can be separated into layers of different conductivities, to create a faithful model for simulating measurements on human skin. Each layer is meshed individually, to ensure appropriate finite element sizes and maintain accuracy across the entire model. The code used for generating this model can be found in Appendix B. The dimensions used for each layer are close to the typical dimensions of the stratum corneum, epidermis and dermis given in Table I.1. The resulting FEM model is illustrated in Figure VI.2. The horizontal dimensions of the model are 10 cm by 10 cm, to fully represent the electrode ring and take into account current propagation on the outside.



(a) 3D view of the model



(b) Slice of the model with only horizontal edges of the finite elements represented, to show the three individually meshed layers of different thicknesses

Figure VI.2: Three-layer finite element model of a piece of skin with a ring of surface electrodes for forward EIT simulations (dimensions in mm)

When EIT models are not bounded by electrodes, an additional optimization step can be taken for image reconstruction. In EIDORS, it is possible to specify a different mesh for image reconstruction than for forward modeling. In the case of surface electrode geometries, this allows the forward model to be used for simulations of current propagation outside of the electrode array while restricting the image reconstruction process to a confined volume closer to the electrodes. This distinction between the forward and reconstruction model helps reduce computation times by skipping the inverse problem where image reconstruction is irrelevant, while still acknowledging the complete physical nature of the problem. Note that a correspondence between the nodes and elements of the forward and reconstruction meshes has to be pre-computed to match the forward simulation data with the reconstruction model before solving the EIT inverse problem. This process is computationally costly but only needs to be

done once per problem geometry.

For reconstructing images using the layered FEM model of the skin as a forward model, a simpler and smaller, the non-layered mesh was used. The choice of not reconstructing an image in layers makes sense as it has already been established that information in the vertical dimension cannot be inferred accurately by EIT algorithms with a surface electrode array. The reconstruction mesh is 70 mm by 70 mm horizontally, which is just large enough to contain the entirety of the electrode ring. The reconstruction model is displayed on top of the forward model in Figure VI.3.

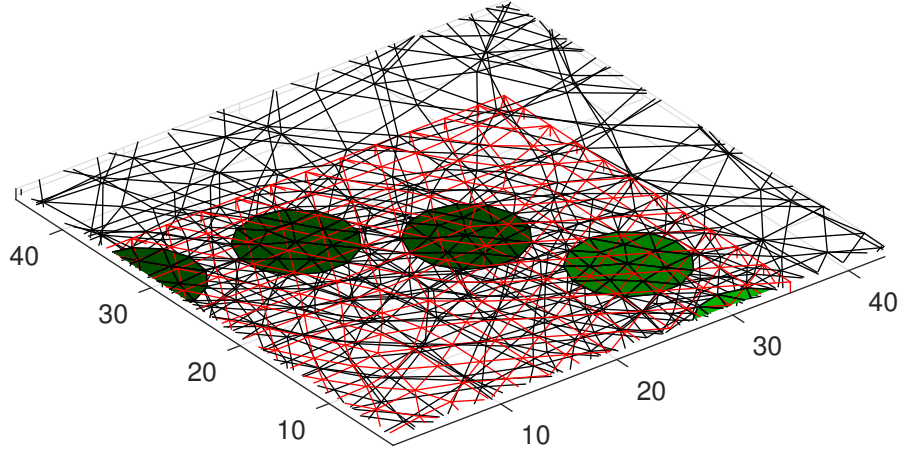


Figure VI.3: Illustration of the reconstruction model (red mesh) on top of the forward FEM model (dimensions in mm)

## VI.2 Simulations

### VI.2.1 Injection patterns evaluation

A first set of simulations was performed on a simpler, deeper homogeneous FEM model using the same electrode geometry as described before. The purpose of these simulations was to test the abilities of both adjacent and opposite current injection patterns, as the COMSOL simulations of Figure VI.1 reopened the debate regarding which of these patterns provided the best sensitivity to the EIT reconstruction. As in Part V, a centered and an off-center object were used to evaluate the performances and spatial sensitivity of EIT on this new geometry. To keep things simple, a difference Gauss-Newton algorithm with a NOSER prior, which proved very effective for qualitative image reconstruction before, was used. The results are shown in Figure VI.4.

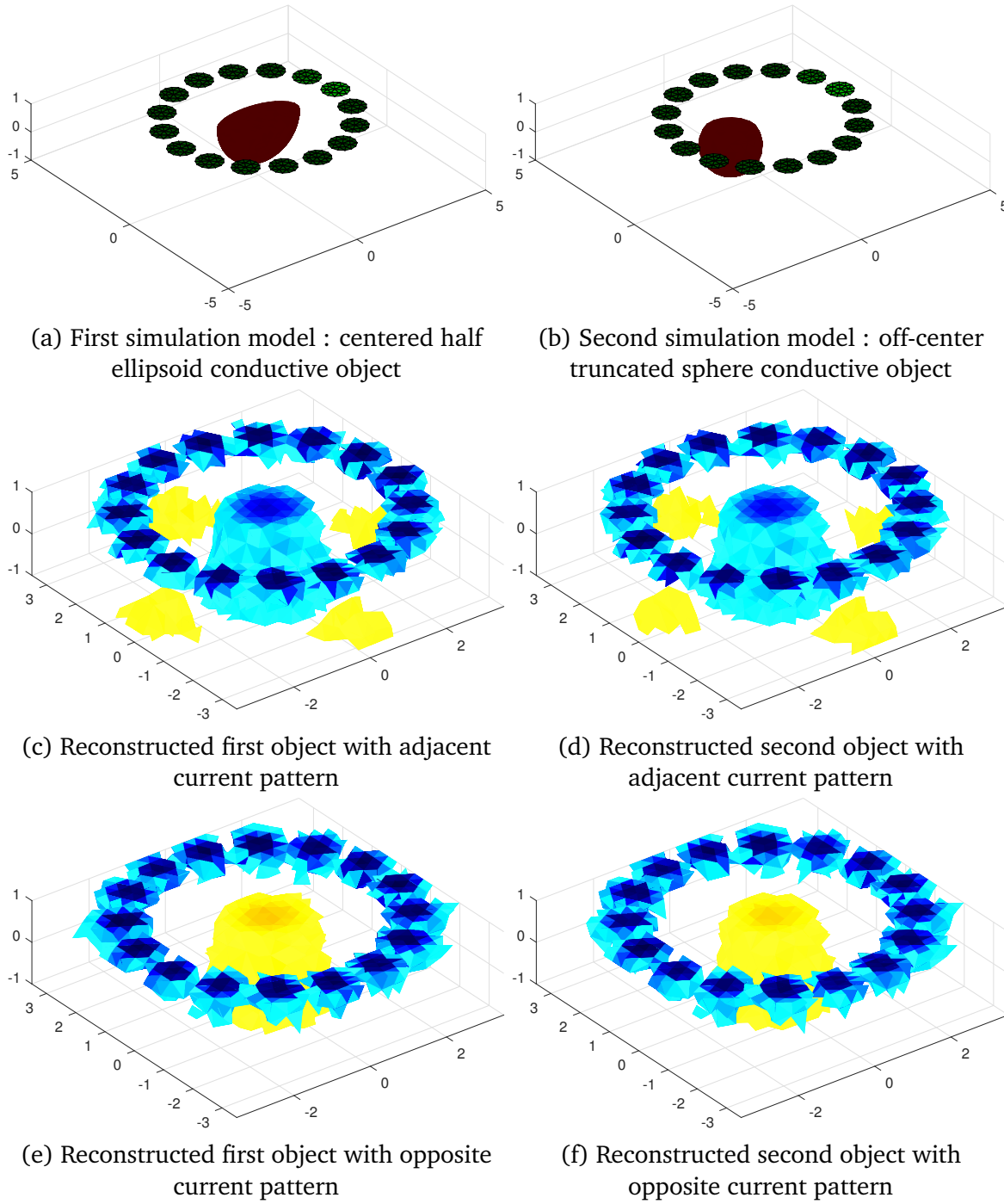


Figure VI.4: First simulated image reconstruction attempts with a circular electrode array on a flat surface using a difference Gauss-Newton algorithm with NOSER prior (dimensions in cm)

This first set of simulations is not exactly promising and is in fact quite worrying, as it seems that despite the creators' claims, EIDORS is not capable of reconstructing images in a configuration where electrodes are placed on an open surface. Indeed,

nothing in these images even hints at the presence of an object where it was placed in the forward model. Moreover, the reconstructed image clearly shows the presence of the electrodes as shown by the blue ring at the surface of each reconstruction, as if the channeling of the current lines had not been taken into account and the entire ring was considered as an object from the model by the EIT algorithm. Just to be sure, the Laplace prior was tested instead of the NOSER prior but does not lead to better results at all.

One possible explanation for this problem is that, in geophysical applications, electrodes are not placed in a circle, but rather in a rectangular array. If an image can be reconstructed in this configuration, it means that the EIT algorithms may lack information about the inside of the electrode ring and that an intermediate electrode configuration should be considered, although this would certainly mark the failure of one of the goals of this project, which was to avoid placing electrodes on the wound itself.

In one of their [tutorials](#), the EIDORS developers provide an example of a simulated reconstruction problem with a rectangular surface electrode array. This example was reimplemented to the letter as a basis for testing the invalidity of circular electrode arrays. However, even then, something unexpected occurs. Despite recopying the example exactly, the results are very different from what is showcased on the EIDORS website, and the reconstruction process appears to encounter the same issues as the attempted reconstruction with the circular electrode array, as shown in Figure VI.5.

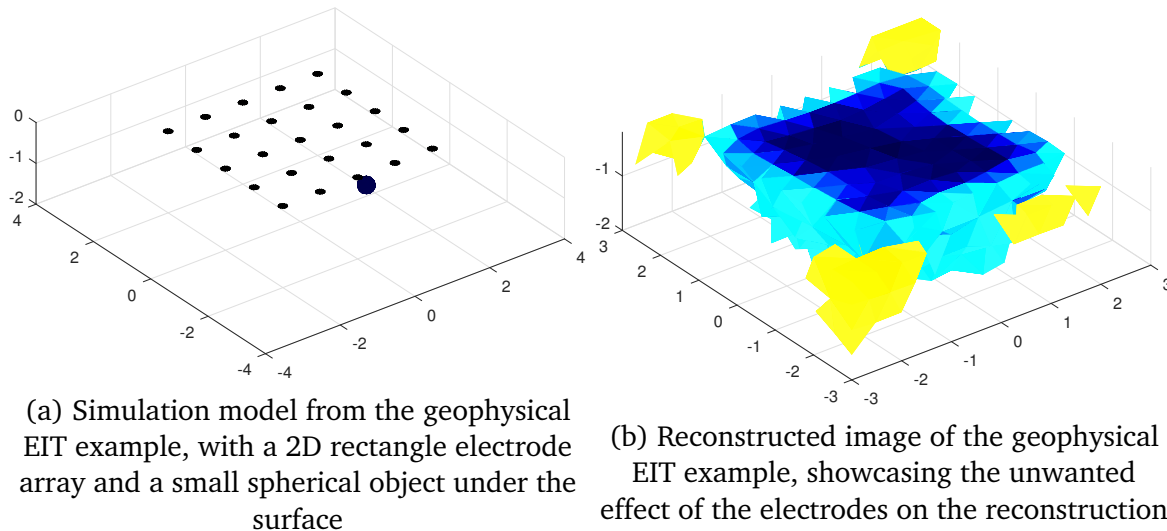


Figure VI.5: Simulation of the geophysical EIT example

At this stage, it was clear that the problem was coming from EIDORS itself, as even example code written and tested by the developers themselves was not producing the right results. With this in mind, I contacted the team maintaining EIDORS, notifying them of the issue and asking about the versions of MATLAB and EIDORS on which the results of the website were obtained. A few weeks later, I was fortunate



enough to hear back from them, informing me that this was indeed a bug that had gone unnoticed for some time due to the seldom use of EIDORS for surface electrode configurations. This problem was actually an issue in the measurements simulations caused by a change in the order of output variables of some Netgen functions. This change caused some elements of the FEM models to have no conductivity assigned, making the simulated measurements erroneous and preventing a correct image from being reconstructed.

With the appropriate fixes implemented, the circular electrode array model was simulated again, with successful results this time. The same simulation setups as the first attempts were used, with results for the centered half-ellipsoid shown in Figure VI.6 and the ones for the off-centered truncated sphere in Figure VI.7.

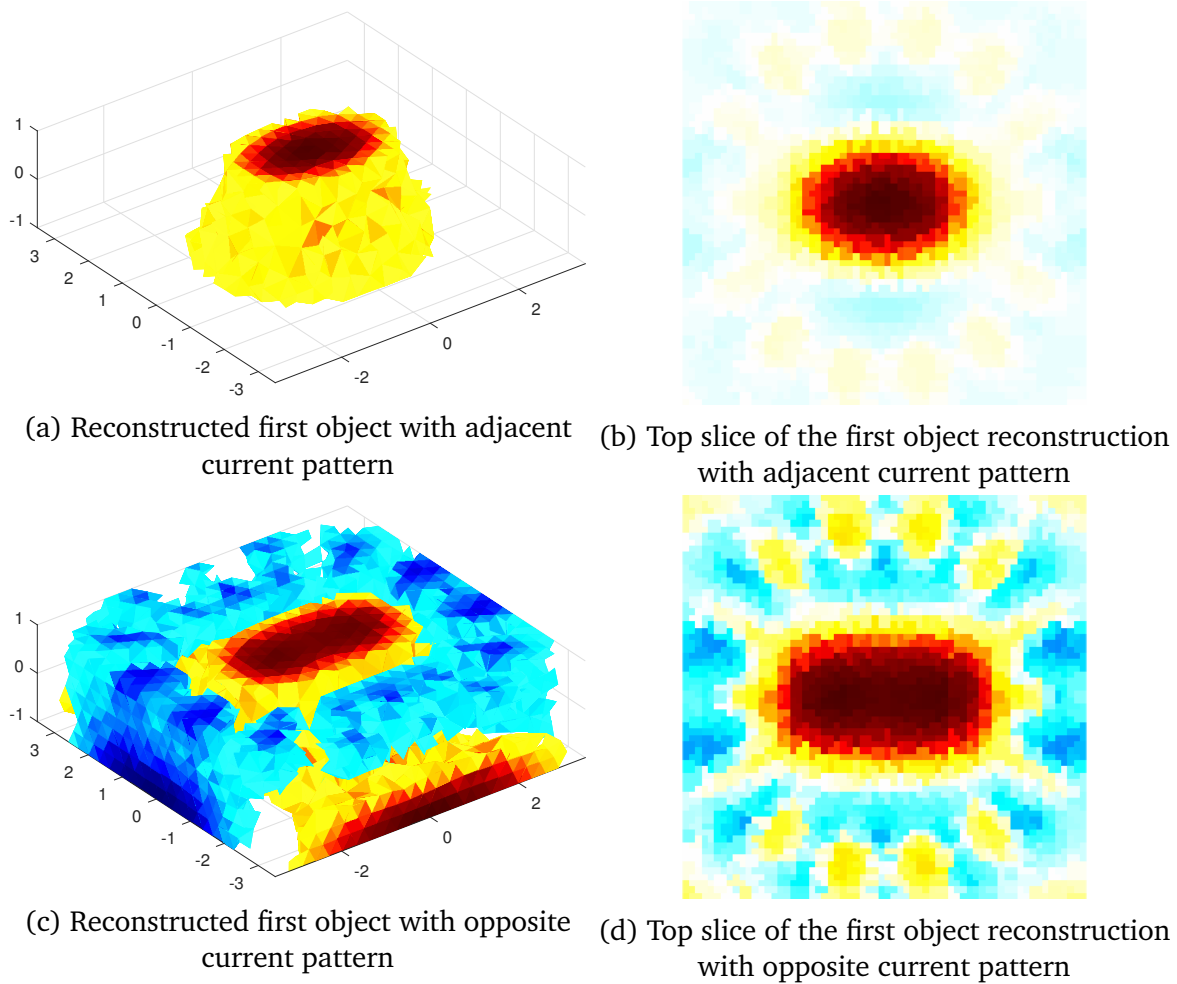


Figure VI.6: Fixed simulated image reconstruction of the centered object with a circular electrode array on a flat surface using a difference Gauss-Newton algorithm with NOSER prior (dimensions in cm)

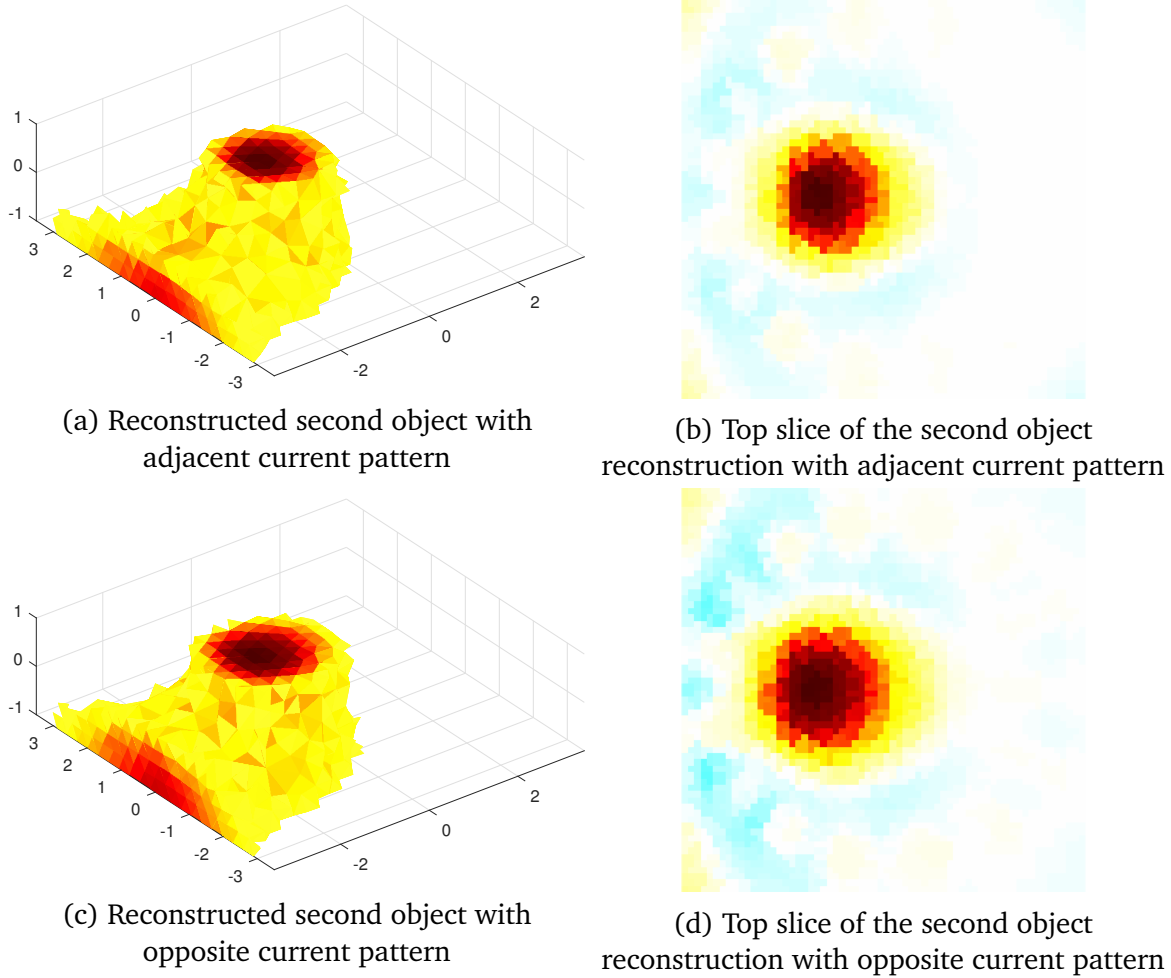


Figure VI.7: Fixed simulated image reconstruction of the off-center object with a circular electrode array on a flat surface using a difference Gauss-Newton algorithm with NOSER prior (dimensions in cm)

These reconstructions on simplified models teach us a few things. Firstly, just like for the algorithm comparison on a traditional EIT geometry performed in Section V.2.4, the reconstructed objects lack any vertical resolution and their top surface is just stretched to the bottom of the reconstruction space. Once again, this is caused by the lack of 3D information for the algorithms to use, as electrodes are only positioned on a single plane. It is now clear that, without additional data, EIT algorithms cannot be expected to reconstruct the depth of a wound using non-invasive surface measurements.

Secondly, the images reconstructed using adjacent current injection patterns appear to be more geometrically accurate than those using opposite current injection. Indeed, Figure VI.6b showcases an elliptic shape closer in size to the top of the simulation model of Figure VI.4a, while the reconstructed object of Figure VI.6d takes a boxier and more elongated shape. A similar observation can be made with the reconstructions of the off-center object of Figure VI.4b : Figure VI.7b clearly displays the



straight left edge of the truncated circle better than Figure VI.7d.

Finally, aside from being a bit more accurate, the adjacent pattern also produces significantly less noise in the reconstructed images. This is particularly apparent when looking at Figure VI.6, where the opposite pattern causes a lot of noise around the electrode ring, similar to what was observed before EIDORS was patched. This confirms the intuition developed with the COMSOL simulations of the two injection patterns, which showed that the channeling of current lines by the electrode ring could cause more current to flow on the inside of the ring with an adjacent injection pattern, traveling through more tissues and gathering more information for image reconstruction.

### VI.2.2 Simulated reconstructions on skin layers model

Now that the best injection pattern for surface electrode geometries has been identified, reconstructions on the full layered FEM skin model can be simulated to assess the performance of EIT for wound imaging with surface measurements. Different conductivities were attributed to each layer of the model to represent the stratum corneum, the rest of the epidermis, and the dermis. The values used are shown in the code example of B, and correspond to the low-frequency conductivity values of each layer from Section I.2.

Different shaped wounds were added to the model in a similar fashion as before. To mimic a reasonably sized ulcer, the penetration of the wound was kept to 0.15 mm, simulating a complete breach of the stratum corneum reaching down to the rest of the epidermis, but keeping the dermis intact.

Finding the right forward models for measurement simulations and image reconstruction was not as straightforward as it seemed. While simulating measurements on the full layered FEM model was good for realism, this model proved unnecessarily complex for the forward simulations involved in image reconstruction. When trying to reconstruct an image on the layered model, the resulting images were nothing but noise, as the irregular FEM meshing was apparently complicating the forward steps of the reconstruction. The fix was quite simple and involved using a different homogeneous forward model for image reconstruction, to emphasize reconstruction of the shape of the wound instead of the skin layers.

Difference and absolute imaging were attempted using the Gauss-Newton algorithm with a NOSER prior. The data for difference imaging was obtained by simulating measurements on the unwounded skin model first, then adding the wound, supposing a calibration step on a healthy and comparable portion of skin. The GREIT algorithm was also tested for difference imaging. The results of all these tests are represented in Figures VI.8 to VI.10.

## VI.2.2.1 Difference imaging

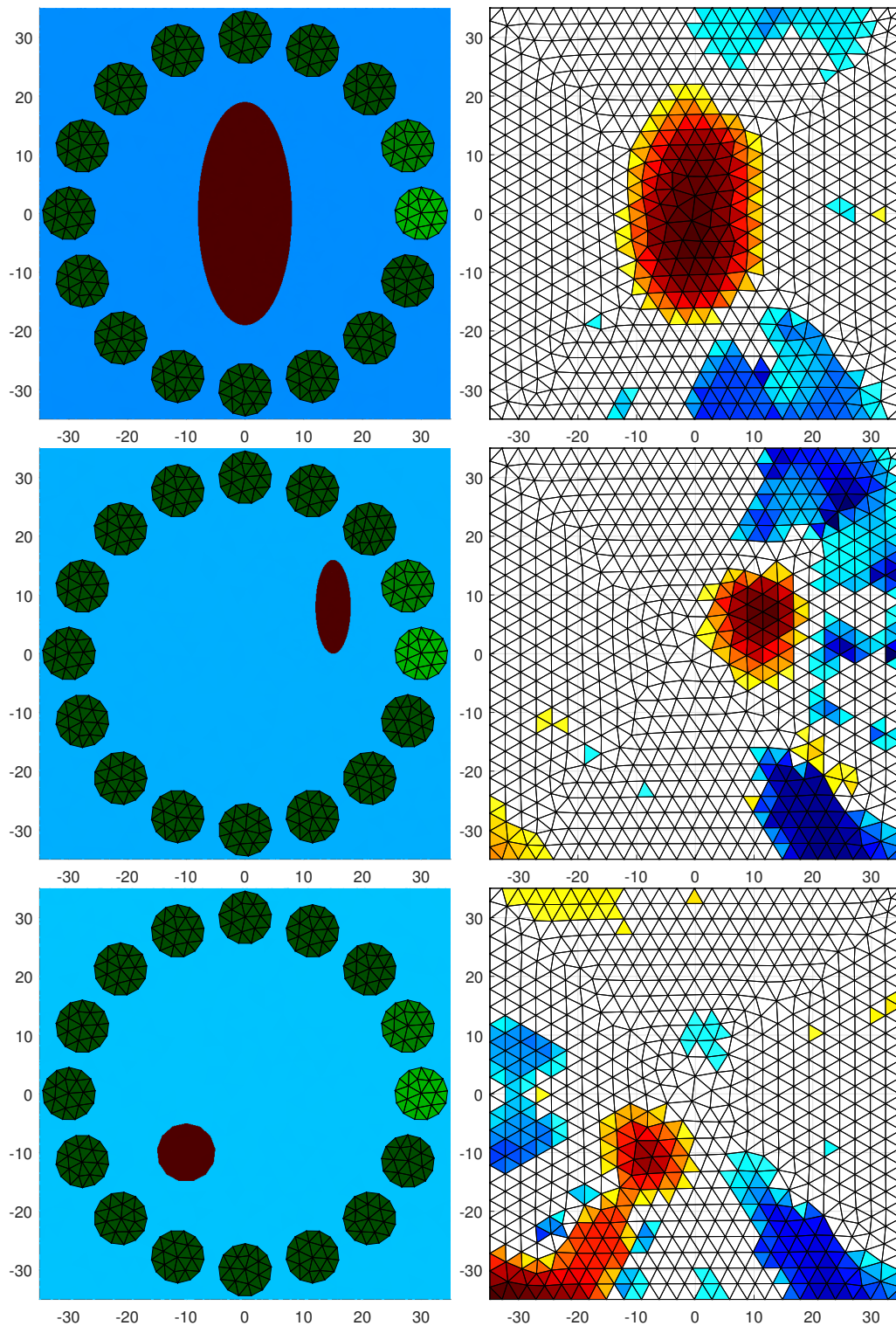


Figure VI.8: Difference imaging of several simulated wounds on the skin FEM model (top views, wound models on the left and corresponding reconstructed images on the right, dimensions in mm)

### VI.2.2.2 Absolute imaging

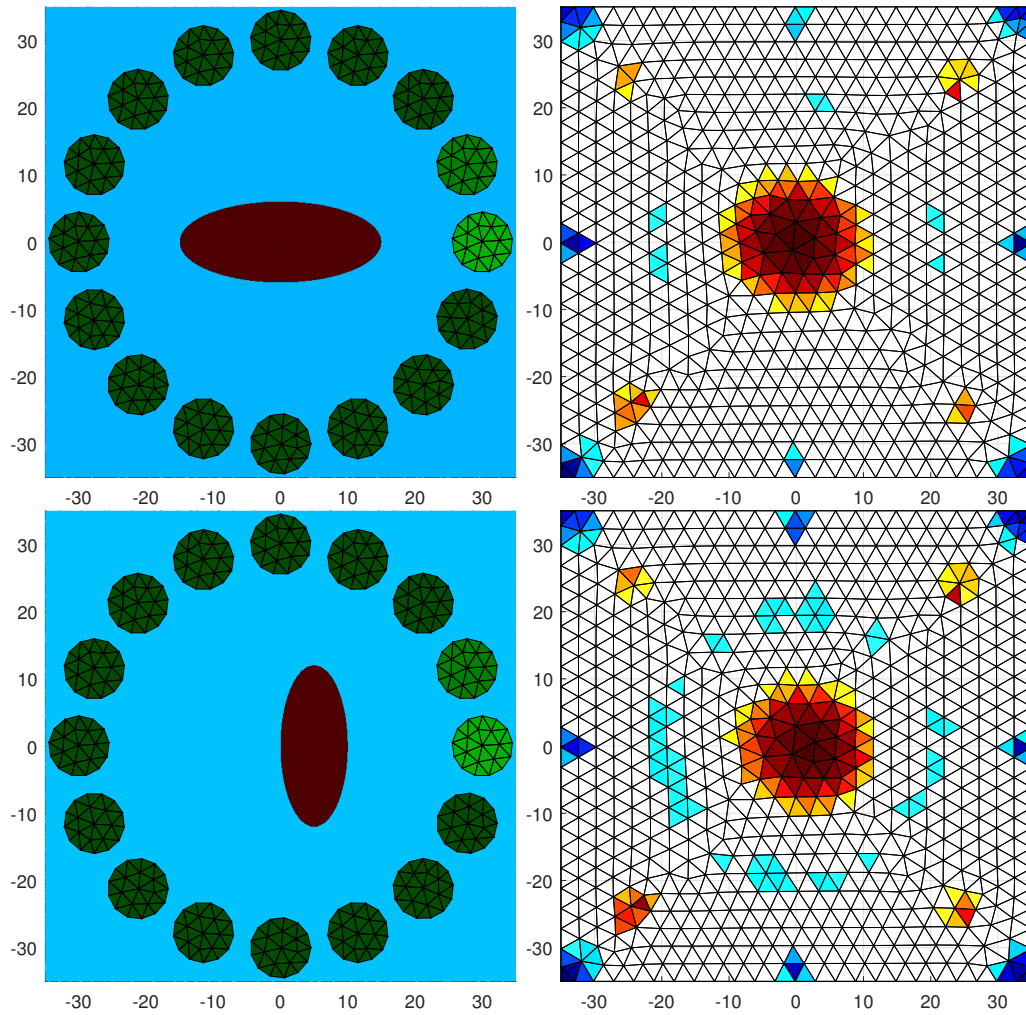


Figure VI.9: Absolute imaging of several simulated wounds on the skin FEM model (top views, wound models on the left and corresponding reconstructed images on the right, dimensions in mm)

### VI.2.2.3 GREIT reconstruction

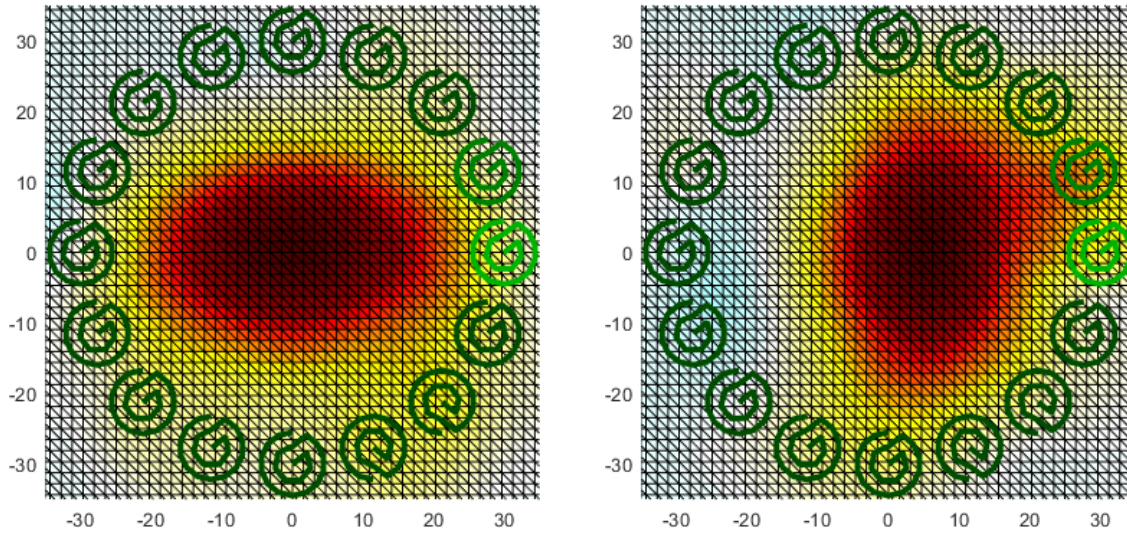


Figure VI.10: GREIT reconstruction of the wound models of Figure VI.9 (dimensions in mm)

### VI.2.2.4 Conclusions

Results from difference imaging are promising. Indeed Figure VI.8 shows good spatial accuracy of the reconstructed images compared to the simulated wounds. Some noise (in blue) is apparent in the images and is caused by the high resistivity of the stratum corneum. Running the same simulations while artificially increasing the conductivity of the stratum corneum layer reduces that noise. Thankfully, it is not difficult to envision a thresholding procedure to remove that noise, as it shows up as low conductivity artifacts.

The GREIT algorithm (Figure VI.10) produces very shape-accurate images with minimal noise, but the dimensions of the reconstructed wounds are clearly too large. Once again, thresholding the images to only keep the highest conductivity values (in dark red) may be a viable solution to improve the wound characterization. One could also imagine using both GREIT and Gauss-Newton reconstructions and combining the information they provide.

Unfortunately, absolute imaging (Figure VI.9) does not lead to satisfying results, as two almost identical images have been reconstructed from completely different wound models. This was somewhat predictable, as the geometry may have become too complicated to handle for this sensitive and unstable algorithm.

To conclude, it seems that, out of the traditional imaging modalities, difference imaging between a calibrated background and the wounded tissues has the highest potential of success, as shown by the promising simulations performed on a realistic layered skin FEM model. It is also important to note that the spatial resolution of the reconstructed images could be increased by decreasing the maximum element size in

the reconstruction meshes. However, going from a 3 mm element size (used for all images showcased in this section) to a 1 mm size makes the problem impossible to solve on a regular computer, as the mapping between the forward and reconstruction models (Figure VI.3) would require more than 40 GB of RAM to be computed.

### VI.2.3 Performance numbers

To conclude this part about simulations of image reconstruction for EIT, some performance numbers, expressed in computation time required for different tasks, are given in Table VI.1. These numbers show which parts of the EIT workflow, if any, represent a potential bottleneck for clinical applications. It is also important to keep in mind that most of these tasks, such as FEM model generations, only need to be performed once in practice, while the EIT inverse solve has to run every time an image is reconstructed.

These computation times were measured on a Windows 10 desktop computer, equipped with a quad-core Intel Core i5 7600K overclocked to 4.5 GHz and 16 GB of dual channel 2666 MHz DDR4 RAM and running MATLAB R2021a.

Maximum element size in FEM models	3 mm	2 mm
Homogeneous mesh generation	1.5 s	2.5 s
Layered skin mesh generation	5.5 s	9.5 s
Measurement forward simulation	0.5 s	0.8 s
Forward and reconstruction models mapping	10 s	25.5 s
Difference image reconstruction	1 s	3 s
GREIT reconstruction	20 s	28 s
Absolute image reconstruction	5 s	15 s

Table VI.1: Computation times of various EIDORS tasks for measurement simulation and image reconstruction

In practice, an entire image reconstruction from real measurements can be performed in less than a minute, which is very promising.

## Part VII

# Experimental setup for skin phantom experimentation

Performing real measurements on wounded skin and trying out the image reconstruction algorithms explored in Part VI would be the perfect way to finalize the investigation of electrical impedance tomography for wound imaging. However, because the project is still in its infancy, clinical trials are out of the equation. Thankfully, finding suitable materials that replicate the electrical properties of human skin is feasible, and imitating wounds on such materials to try out a real image reconstruction would make a great proof of concept.

In this final part, the planned experimental setup for real-life validation of EIT for open wound imaging is described. An electrode setup suited for experimentations is presented, and relevant skin phantom materials are mentioned.

## VII.1 Experimental setup

### VII.1.1 Measurements

So far, practical measurements have included impedance spectroscopy with pseudo-random binary sequences using the Vitapatch prototype PCB, and mono-frequency voltage measurements using the SPECTRA board. EIDORS also uses single frequency voltage measurements in simulations and image reconstructions.

From an EIDORS stimulation data structure, it is not difficult to extract instructions to send via Bluetooth or UART to the PCB to ask it to perform the required sequence of measurements. The measurement data received from the PCB is encoded in base 64 and consists of interlaced values of the sampled response and stimulation as 16-bit integers that simply need to be decoded using a couple of MATLAB commands.



To perform electrical impedance tomography using the Vitapatch PCB, the gap between impedance spectroscopy and single voltage measurements used by EIDORS has to be bridged. It is abundantly clear that the sampled response sequence cannot be used by itself as it lacks any meaning before being processed together with the corresponding stimulation. In an EIT geometry, dividing the voltage between a pair of electrodes by the injected current to compute an impedance as if these signals came from four-point measurements is not strictly correct, as the current distribution in the imaging body is complex and the voltage measured between two electrodes does not stem from the entirety of the stimulation current. However, the resulting spectra should still be suitable for use in EIT. Indeed, measuring voltages resulting from a fraction of the total injected current in a portion of the total volume is precisely what EIT requires. By dividing the spectra of all measured voltages by the one of the total stimulation current, the magnitude spectrum of the voltages are "normalized" with respect to the spectral density of the stimulation. As all measurements are divided by the same stimulation spectrum, the proportionality between measured voltages should still be kept identical.

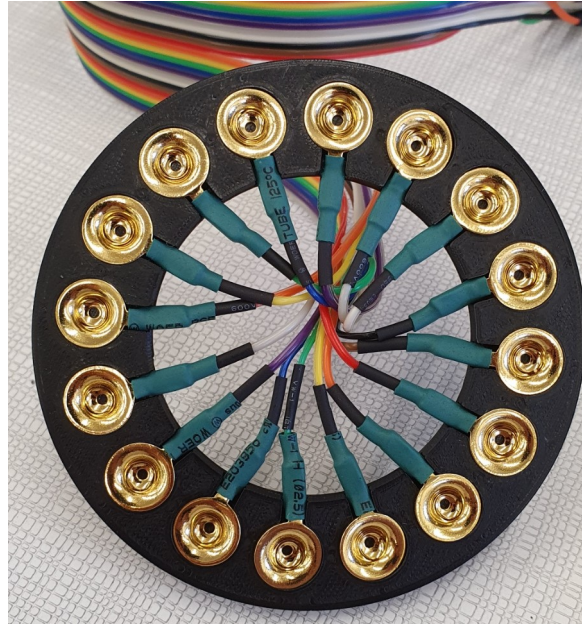
Once the measurements have been processed following the procedure of Part IV, providing data to EIDORS is simply a matter of choosing one or two frequencies of interest (if performing frequency difference imaging), and gathering the magnitude values of all voltage measurements at these frequencies from the regressed spectra.

### VII.1.2 Electrode setup

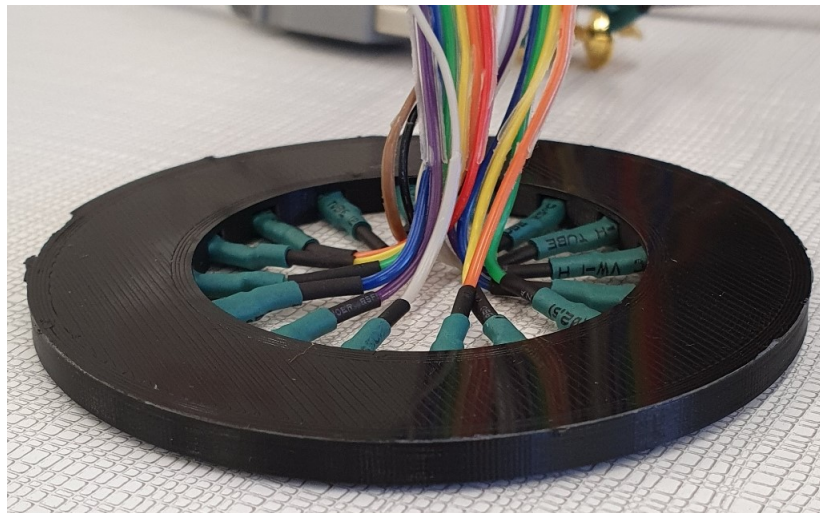
Because the Vitapatch project is still at an early stage of development, experiments that aim at validating the capabilities of EIT for wound imaging are the first physical experiments to take place for this project. Therefore, it is too early to consider using specialized, long-term, and biocompatible electrode solutions such as those presented in Section II.2.2.3. As a consequence, readily available gold-plated cup electrodes, which require the use of a conductive gel will be used for convenience. Using these known good electrodes makes sense at this stage, as experimental electrodes could end up being a confounding variable for the validation of EIT techniques.

This experiment uses a ring of 16 electrodes to place around the wound to be monitored. For the early stages of the project, it was decided to fix the radius of this ring to 6 cm.

As explained in Section V.1.2, an accurate geometric model of the electrodes is crucial for the success of EIT reconstruction. To ensure consistency between measurements and the creation of an accurate model, a 3D printed support bracket for the electrodes was designed. This ensures that electrodes will stay in place during the whole experiment process, and guarantees that their relative positions precisely match those specified in the FEM models. This bracket, shown in Figure VII.1, was designed for gold-plated cup electrodes to clip into and stay in place with friction. Grooves were added to allow the cables to exit the ring from the inside in one neat bunch.



(a) Bottom view, with 16 gold plated cup electrodes



(b) Side view when applied to a flat surface

Figure VII.1: 3D-printed electrode holding ring for preliminary experiments

### VII.1.3 Skin phantoms

To perform realistic experiments and validate the ability of EIT to reconstruct an accurate image of a wound using a circular electrode array placed around the wound, it is necessary to find a suitable material to use for testing impedance measurements on. Unfortunately, the project is still in its infancy, and performing animal or clinical trials on patients suffering from chronic wounds is out of the question.

Therefore, it is necessary to find a material that would be suitable to mimic human skin, and on which various incisions could be performed. Thankfully, studies [71]



report that porcine skin is very similar to human skin in terms of thickness and content (amount of hair follicles, sweat glands, ...), making it especially suitable to study wounds and their healing process. Hence, a fresh sample of pork skin was sourced from a local butcher to experiment on. Importantly, this sample was never frozen, as storing meat in a regular food freezer can often cause ice crystals to form in and out of cells, and puncture cell membranes [72]. As these membranes are an integral component in the electrical behavior of tissues, as explained in Section 1.2.2, it was important to avoid this damage.

Unfortunately, a meat sample can lack some properties of living tissues such as sweating or the manifestation of biological potentials. Fortunately, other studies [7, 31] suggest that to simulate superficial wounds, moisturizer can be used locally on some part of the skin to decrease the overall resistance of that area by mitigating the high resistance of the stratum corneum (as described in Section 1.2). This would allow some other experiments to be performed on a healthy volunteer to explore the impact of these properties.

To experiment with the pork skin and compare measurements before and after creating a wound on it, the first electrode ring was not practical, as the cables blocked the inside of the ring where imaging is supposed to take place. To circumvent this issue, a second version of the electrode holder was 3D printed, this time with the cable channels facing outside the ring, as shown in Figures VII.2 and VII.3.

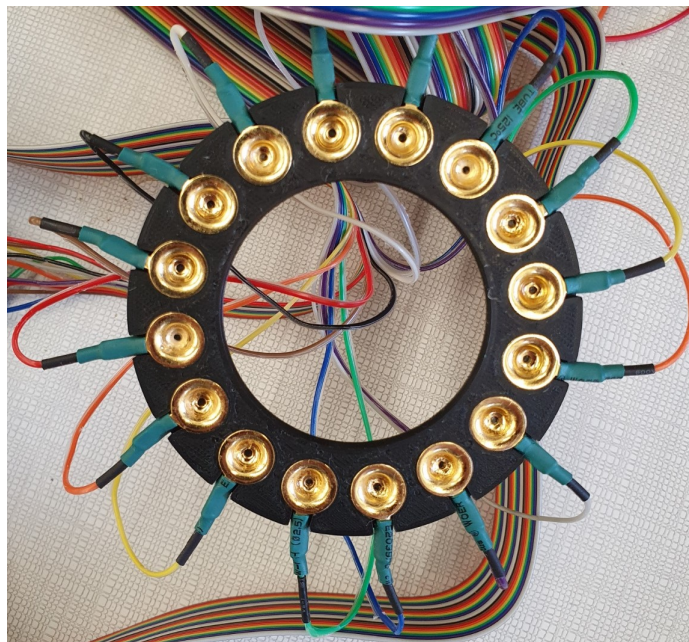


Figure VII.2: Second version of the 3D-printed electrode holder, with wires exiting from the outside for easy access to the imaged surface

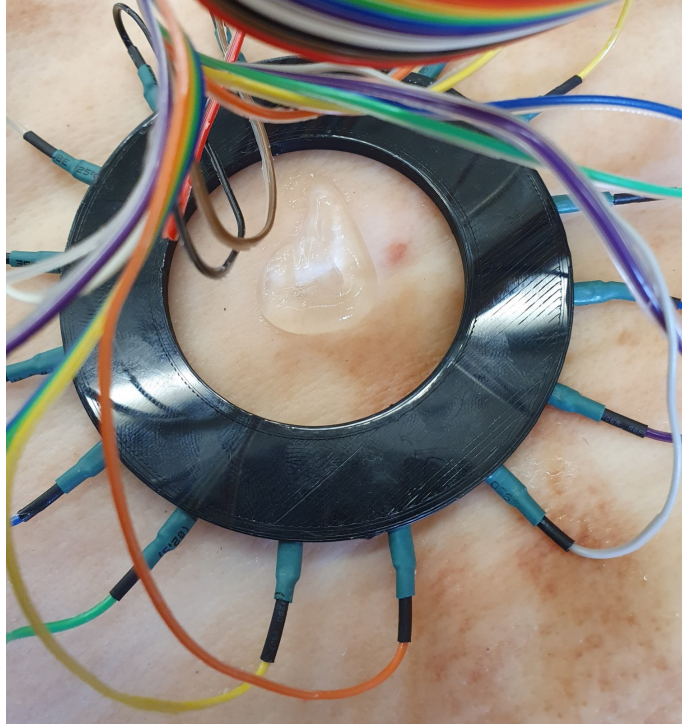


Figure VII.3: Electrode ring applied to pork skin, with a blob of conductive gel as the object to image

## VII.2 Results

Unfortunately, the planned wound image reconstruction experiments on skin phantoms could not be performed in the time frame of this thesis. As already mentioned at the end of Part IV, prolonged delays in the manufacturing of the prototype Vitapatch PCB have greatly limited the available time for hardware debugging opportunities. As things stand, issues with measurements of lower frequency responses still remain, compromising the bioimpedance spectroscopy protocol. Using the SPECTRA board as a backup bioimpedance measurement device was considered to validate the EIT image reconstruction, but damage to its fragile flex cable used for connecting cup electrodes put a stop to that idea as well.

Hopefully, the Vitapatch PCB will be operational in the near future, and similar experiments to the one set up in this part will be carried out to show the potential of EIT for open wound imaging. In the meantime, the detailed FEM simulations of Part VI hopefully serve as convincing proofs of concept for this technique.

# Conclusion and perspectives

During the course of this project, the electrical properties of skin layers have been gathered to understand the effect of a wound on impedance measurements. Wounded skin is expected to display lower resistivity because of the rupture of the external layers of the skin made up of keratin. Frequency-dependent properties are also expected to be modified. These electrical properties can be measured according to medical protocols and good practice in electrical engineering, including four-point measurements and respect for safe current limits. For long-term applications, some novel types of biocompatible electrodes exist and can be used to monitor a chronic wound for extended periods.

By analyzing, simulating, and using the prototype Vitapatch PCB, an unusual signal processing routine suited for analyzing measurements involving pseudo-random binary sequence signals used for ultra-low-power spectroscopy has been developed. This routine includes the use of a machine learning regression algorithm to eliminate noise in the impedance spectra obtained after Fourier analysis. A few limitations of the prototype PCB have been discovered during experiments, and some improvements were implemented. Ultimately, long delays in the manufacturing of this prototype left little time to experiment with it during this project, but advances have been made nonetheless.

The use of electrical impedance tomography algorithms for image reconstruction of a wound proved promising, even though it was challenging at times. Initial simulations and experiments on traditional geometries went well, but trying to adapt the reconstruction problem to a surface electrode array around a wound was not straightforward. After fixing a bug in EIDORS, convincing image reconstruction results were obtained, and subtleties of flat electrode arrays were explored. Concluding the investigation of EIT were simulations performed on a finite element model made to represent the different layers of the skin and their unique electrical properties. These simulations brought less ideal but still promising results, and would have been compared to practical experiments, had more time been left to iron out issues in the experimental setup.

The results obtained by the end of this work are promising for the success of the Vitapatch project. Some future work and prospects to capitalize on the contents of this thesis naturally include resolving the last remaining issues with the bioimpedance

PCB. SPICE simulation software could be used to perform more advanced circuit simulations and investigate the low-frequency errors, as well as the noise sources.

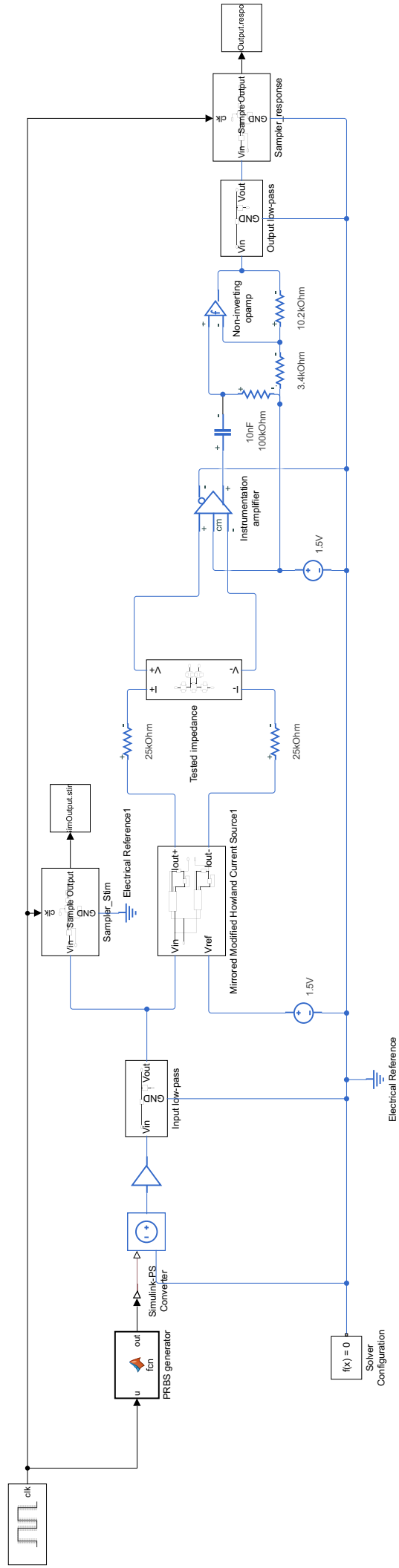
Afterward, the skin phantom experiment started in Part VII can be completed, to hopefully reproduce the success of the simulated image reconstructions using real data. Appropriate baselining calibration methods to obtain some generic background measurements and exploit the most effective difference imaging algorithms for wound imaging can also be explored.

Looking further, one could look to exploit the entirety of the bioimpedance spectrum recovered thanks to PRBS spectroscopy to assess the state of the wound. Using the information about the electrical properties of skin gathered in Part I, some classification methods could be established and used in conjunction with EIT image reconstruction. This would provide both a qualitative visual representation of the wound as well as quantitative data about the status of the injured tissues.

Alternatively, novel multifrequency EIT modalities using entire spectroscopic measurements to reconstruct more comprehensive and quantitative images, such as the fraction volume imaging researched by Malone [57], could be investigated. Such methods would blend spectroscopy and tomography, with the prospect of creating the most clinically relevant images possible.

# Appendices

## Appendix A : Simulink circuit model



## Appendix B : EIDORS code example

```
%% Start EIDORS
run 'C:\Program Files\MATLAB\eidors-v3.10-ng\eidors\startup
    .m';

%% FEM models creation
%Dimensions in mm
model_radius = 50;
el_radius = 4.5;
ring_radius = 30;
model_height = 2;
n_elects = 16;

perm_skin = 8.854e-12 * 1e3;

% Netgen commands for FEM modeling
shape_str_bg = ['solid top = plane(0,0,1;0,0,1);\n' ...
    'solid mainobj = top and orthobrick(-50,-50,-1;50,50,1)
    -maxh=3;\n'];

shape_str_lay = ['solid top = plane(0,0,1;0,0,1);\n' ...
    'solid lay1 = orthobrick(-50,-50,-1;50,50,0.8); tlo
    lay1;\n' ...
    'solid lay2 = orthobrick(-50,-50,0.8;50,50,0.98); tlo
    lay2;\n' ...
    'solid mainobj = top and orthobrick(-50,-50,-1;50,50,1)
    and not lay1 and not lay2 -maxh=3;\n'];

shape_str_wound = ['solid top = plane(0,0,1;0,0,1);\n' ...
    'solid wound = ellipsoid(0,0,1;0,0,5;5,0,0;0,12,0) and
    orthobrick(-20,-20,0.85;20,20,1); tlo wound;\n' ...
    'solid lay1 = orthobrick(-50,-50,-1;50,50,0.8) and not
    wound; tlo lay1;\n' ...
    'solid lay2 = orthobrick(-50,-50,0.8;50,50,0.98) and
    not wound; tlo lay2;\n' ...
    'solid mainobj = top and orthobrick(-50,-50,-1;50,50,1)
    and not lay1 and not lay2 and not wound -maxh=3;\n'
    ];

% The top solid is a vertical plane where electrodes are
    placed
% Orthobricks are rectangular prisms, the coordinates are
    two diagonally
% opposed edges
```

```

% For an ellipsoid, the center and the lengths of its 3
    axes in all
% directions are specified
% 'and' and 'and not' are used to create solids from
    intersections of
% shapes and make all solids mutually exclusive
% a 'mainobj' needs to be specified for each model, '-maxh'
    specifies the
% maximal element size for the model
% 'tlo' indicates that the solid has to be meshed
    independently

% Electrodes are positioned in a circle on the top layer of
    the models
ang = linspace(0,2*pi*(1-1/n_elecs), n_elecs);
elec_pos_x = ring_radius .* cos(ang);
elec_pos_y = ring_radius .* sin(ang);
% elec_pos contains the positions and normal vector of each
    electrode
elec_pos = [elec_pos_x(:), elec_pos_y(:), ones(size(
    elec_pos_x(:)))*[1,0,0,1]];
elec_obj = 'top';

% Netgen model generation
model_b = ng_mk_gen_models(shape_str_bg, elec_pos,
    el_radius, elec_obj);
model_s = ng_mk_gen_models(shape_str_lay, elec_pos,
    el_radius, elec_obj);
model_w = ng_mk_gen_models(shape_str_wound, elec_pos,
    el_radius, elec_obj);

% Contact impedances are added to the electrodes
for i=1:n_elecs
    model_b.electrode(i).z_contact = 5000;
    model_s.electrode(i).z_contact = 5000;
    model_w.electrode(i).z_contact = 5000;
end

% Images are created from models. Images have conductivity
    values assigned
% to each element
% model.mat_idx contains the indices of the elements of
    each solid in the
% order they were specified to Netgen
img1 = mk_image(model_s, 1);

```



```

img1.elem_data(model_s.mat_idx{1}) = 0.4; %dermis
img1.elem_data(model_s.mat_idx{2}) = 0.3; %epidermis
img1.elem_data(model_s.mat_idx{3}) = 4e-4; %SC

img2 = mk_image(model_w, 1);
img2.elem_data(model_w.mat_idx{1}) = 1; %wound
img2.elem_data(model_w.mat_idx{2}) = 0.4; %dermis
img2.elem_data(model_w.mat_idx{3}) = 0.3; %epidermis
img2.elem_data(model_w.mat_idx{4}) = 4e-4; %SC

%% Calculate a stimulation pattern and simulate the voltage
    measurements for the background and the object

stim = mk_stim_patterns(16,1,'{ad}','{ad}',{},1); %16
    electrodes, 1 ring, adjacent drive and measurement, no
    options, 1 mA arbitrary current

% For simulations, a stimulation must be attributed to each
    model and image
img1.fwd_model.stimulation = stim;
img2.fwd_model.stimulation = stim;

model_b.stimulation = stim;
model_s.stimulation = stim;
model_w.stimulation = stim;

v_bg = fwd_solve(img1);
v_obj = fwd_solve(img2);

%% Inverse solve and difference image reconstruction
% Reconstruction model: a smaller region directly over the
    electrodes
shape_str = 'solid mainobj= orthobrick(-35,-35,-1;35,35,1)
    -maxh=3;';
cmd1 = ng_mk_gen_models(shape_str, [], [], '');

% Define the mapping between the two meshes
c2f= mk_coarse_fine_mapping( model_b, cmd1);

% Create an inverse reconstruction model with NOSER prior
    using the
% homogeneous model_b as a forward model
inv3d= select_imdl(model_b, {'NOSER dif'});
inv3d.prior_use_fwd_not_rec = 1;
inv3d.fwd_model.coarse2fine = c2f;

```

```

inv3d.rec_model = cmdl;

% Solve the image reconstruction problem and display the
    result
img_s = inv_solve(inv3d, v_bg, v_obj);
show_fem(img_s);
%% Absolute reconstruction
inv3d= select_imdl(model_b, {'Basic GN abs'});
inv3d.RtR_prior= @prior_noser;
inv3d.prior_use_fwd_not_rec = 1;
inv3d.fwd_model.coarse2fine = c2f;
inv3d.rec_model = cmdl;

img_s = inv_solve(inv3d, v_obj);

%% GREIT reconstruction
% if the NF is too low, too much weight is given to the
    training examples
% and the image recreated is just the training distribution
% if it is too high, the reconstruction is just a uniform
    image
% -> play with noise figure until the reconstruction looks
    good
opts.noise_figure = 0.4;
weights = [];
opts.imgsz = [64 64]; % Double the default image resolution

% Train a GREIT model and reconstruct an image
imdl = mk_GREIT_model(model_b,0.2,weights,opts);
imgr = inv_solve(imdl, v_bg, v_obj);

```

# Bibliography

- [1] Wikipedia. *Chronic wound*. URL: [https://en.wikipedia.org/wiki/Chronic\\_wound](https://en.wikipedia.org/wiki/Chronic_wound) (visited on 07/21/2022).
- [2] Wikipedia. *Wound*. URL: <https://en.wikipedia.org/wiki/Wound> (visited on 07/21/2022).
- [3] UK National Health Service. *Pressure ulcers (pressure sores)*. URL: <https://www.nhs.uk/conditions/pressure-sores/> (visited on 07/21/2022).
- [4] UK National Health Service. *Venous leg ulcer*. URL: <https://www.nhs.uk/conditions/leg-ulcer/> (visited on 07/21/2022).
- [5] Atte Kekonen et al. "A Quantitative Method for Monitoring Wound Healing". In: *International Journal of Bioelectromagnetism* 17 (Dec. 2015), pp. 36–41.
- [6] Atte Kekonen et al. "Bioimpedance method for monitoring venous ulcers: Clinical proof-of-concept study". In: *Biosensors and Bioelectronics* 178 (2021), p. 112974. ISSN: 0956-5663. DOI: <https://doi.org/10.1016/j.bios.2021.112974>. URL: <https://www.sciencedirect.com/science/article/pii/S0956566321000105>.
- [7] SooIn Kang et al. "Development of an Electrical Impedance Tomography Spectroscopy for Pressure Ulcer Monitoring Tool: Preliminary study". In: vol. 2020. July 2020, pp. 5073–5076. DOI: [10.1109/EMBC44109.2020.9176256](https://doi.org/10.1109/EMBC44109.2020.9176256).
- [8] Ulrik Birgersson. *Electrical Impedance of Human Skin and Tissue Alterations : Mathematical Modeling and Measurements*. Stockholm, Sweden: Karolinska Institutet, Jan. 1, 2013. ISBN: 978-91-7549-019-9.
- [9] TELEDYNE SYSTEMS CORPORATION. *Electrical resistance of the skin*. Contractor report NASA-CR-57212. Hawthorne, California: for Spacelabs Inc., Nov. 1964. URL: <https://ntrs.nasa.gov/citations/19660021872>.
- [10] Cleveland Clinic. *Health library : Skin*. 2006. URL: <https://my.clevelandclinic.org/health/articles/10978-skin> (visited on 08/10/2022).
- [11] John Blamire. *Skin Morphology*. 2005. URL: [http://www.brooklyn.cuny.edu/bc/ahp/LAD/C4d/C4d\\_skin.html](http://www.brooklyn.cuny.edu/bc/ahp/LAD/C4d/C4d_skin.html) (visited on 07/20/2022).
- [12] Tasneem Poonawalla. *Anatomy of the Skin*. 2008. URL: [https://www.utmb.edu/pedi\\_ed/CoreV2/Dermatology/page\\_03.htm](https://www.utmb.edu/pedi_ed/CoreV2/Dermatology/page_03.htm) (visited on 07/20/2022).

- [13] Ronald Pethig. "Dielectric properties of body tissues". In: *Clinical physics and physiological measurement : an official journal of the Hospital Physicists' Association, Deutsche Gesellschaft für Medizinische Physik and the European Federation of Organisations for Medical Physics* 8 Suppl A (Feb. 1987), pp. 5–12. DOI: [10.1088/0143-0815/8/4A/002](https://doi.org/10.1088/0143-0815/8/4A/002).
- [14] Tushar Kanti Bera. "Bioelectrical Impedance and The Frequency Dependent Current Conduction Through Biological Tissues: A Short Review". In: *IOP Conference Series: Materials Science and Engineering* 331 (Mar. 2018), p. 012005. DOI: [10.1088/1757-899X/331/1/012005](https://doi.org/10.1088/1757-899X/331/1/012005).
- [15] Carlos-Augusto Gonzalez-Correa. "Clinical Applications of Electrical Impedance Spectroscopy". In: Mar. 2018, pp. 187–218. ISBN: 978-3-319-74387-5. DOI: [10.1007/978-3-319-74388-2\\_10](https://doi.org/10.1007/978-3-319-74388-2_10).
- [16] Camelia Gabriel. *Compilation of the Dielectric Properties of Body Tissues at RF and Microwave Frequencies*. Final technical report ADA303903. KING'S COLL LONDON (UNITED KINGDOM) DEPT OF PHYSICS, Jan. 1996. URL: <https://apps.dtic.mil/sti/citations/ADA303903>.
- [17] Sami Gabriel, R.W. Lau, and Camelia Gabriel. "The dielectric properties of biological tissue II: Measurements in the frequency range 10 Hz to 20 GHz". In: *Physics in medicine and biology* 41 (Dec. 1996), pp. 2251–69. DOI: [10.1088/0031-9155/41/11/002](https://doi.org/10.1088/0031-9155/41/11/002).
- [18] S Gabriel, R W Lau, and C Gabriel. "The dielectric properties of biological tissues: III. Parametric models for the dielectric spectrum of tissues". In: *Physics in Medicine and Biology* 41.11 (Nov. 1996), pp. 2271–2293. DOI: [10.1088/0031-9155/41/11/003](https://doi.org/10.1088/0031-9155/41/11/003). URL: <https://doi.org/10.1088/0031-9155/41/11/003>.
- [19] D.Andreuccetti, R.Fossi, and C.Petrucci. *An Internet resource for the calculation of the dielectric properties of body tissues in the frequency range 10 Hz - 100 GHz*. Based on data published by C.Gabriel et al. in 1996. IFAC-CNR, Florence (Italy). 1997. URL: <http://niremf.ifac.cnr.it/tissprop/> (visited on 08/12/2022).
- [20] K Wake, K Sasaki, and S Watanabe. "Conductivities of epidermis, dermis, and subcutaneous tissue at intermediate frequencies". In: *Physics in Medicine and Biology* 61.12 (May 2016), pp. 4376–4389. DOI: [10.1088/0031-9155/61/12/4376](https://doi.org/10.1088/0031-9155/61/12/4376). URL: <https://doi.org/10.1088/0031-9155/61/12/4376>.
- [21] Keysight Technologies. *Materials Measurement: Dielectric Materials*. Application Brief. July 2014. URL: <https://www.keysight.com/us/en/assets/7018-08589/brochures/5989-4713.pdf>.
- [22] Tatsuma Yamamoto and Yoshitake Yamamoto. "Electrical Properties of Epidermal Stratum Corneum". In: *Japanese journal of medical electronics and biological engineering* 11.5 (1973), pp. 337–343. DOI: [10.11239/jsmbe1963.11.337](https://doi.org/10.11239/jsmbe1963.11.337).

- [23] Valerica Raicu, Nobuko Kitagawa, and Akihiko Irimajiri. “A quantitative approach to the dielectric properties of the skin”. In: *Physics in Medicine and Biology* 45.2 (Dec. 1999), pp. L1–L4. DOI: [10.1088/0031-9155/45/2/101](https://doi.org/10.1088/0031-9155/45/2/101). URL: <https://doi.org/10.1088/0031-9155/45/2/101>.
- [24] Bill Lionheart. *Electrical impedance tomography Reconstruction Course*. 2010. URL: [https://youtube.com/playlist?list=PL14-1W19d3VN9uu\\_\\_UK8\\_Z--rQo07Vr1Z](https://youtube.com/playlist?list=PL14-1W19d3VN9uu__UK8_Z--rQo07Vr1Z) (visited on 07/31/2022).
- [25] Damijan Miklavcic, Natasa Pavselj, and Francis Hart. “Electric Properties of Tissues”. In: vol. 6. Apr. 2006. ISBN: 9780471740360. DOI: [10.1002/9780471740360.ebs0403](https://doi.org/10.1002/9780471740360.ebs0403).
- [26] Wikipedia. *Electrodermal activity*. URL: [https://en.wikipedia.org/wiki/Electrodermal\\_activity](https://en.wikipedia.org/wiki/Electrodermal_activity) (visited on 08/12/2022).
- [27] Hank Lukaski and Micheal Moore. “Bioelectrical Impedance Assessment of Wound Healing”. In: *Journal of diabetes science and technology* 6 (Jan. 2012), pp. 209–12. DOI: [10.1177/193229681200600126](https://doi.org/10.1177/193229681200600126).
- [28] Monica Christine Lin. “Impedance Spectroscopy for Surface and Fracture Wounds: Sensor Development and Clinical Application”. PhD thesis. University of California, San Francisco and University of California, Berkeley, 2018.
- [29] Carlos Marquez. “Electrical Characterization of Reliability in Advanced Silicon-On-Insulator Structures for sub-22nm Technologies”. PhD thesis. Mar. 2017. DOI: [10.13140/RG.2.2.34719.56489](https://doi.org/10.13140/RG.2.2.34719.56489).
- [30] Kenneth S. Cole and Robert H. Cole. “Dispersion and Absorption in Dielectrics I. Alternating Current Characteristics”. In: *The Journal of Chemical Physics* 9.4 (1941), pp. 341–351. DOI: [10.1063/1.1750906](https://doi.org/10.1063/1.1750906). eprint: <https://doi.org/10.1063/1.1750906>. URL: <https://doi.org/10.1063/1.1750906>.
- [31] Arijit Roy et al. “Measurement of bioimpedance and application of Cole model to study the effect of moisturizing cream on human skin”. In: *AIMS Biophysics* 7.4 (2020), pp. 362–379. ISSN: 2377-9098. DOI: [10.3934/biophy.2020025](https://doi.org/10.3934/biophy.2020025). URL: <https://www.aimspress.com/article/doi/10.3934/biophy.2020025>.
- [32] Goran Lazović et al. “Modeling of Bioimpedance for Human Skin Based on Fractional Distributed- Order Modified Cole Model”. In: *FME Transactions Faculty of Mechanical Engineering, Belgrade* 42 (Jan. 2014), pp. 74–81. DOI: [10.5937/fmet1401075L](https://doi.org/10.5937/fmet1401075L).
- [33] Matt Lacey. *The constant phase element*. URL: <http://lacey.se/science/eis/constant-phase-element/> (visited on 08/20/2022).
- [34] José Guerreiro, Andre Lourenco, and Ana Fred. “A Biosignal Embedded System for Physiological Computing”. PhD thesis. Dec. 2013, pp. 13–17. DOI: [10.13140/2.1.4596.0481](https://doi.org/10.13140/2.1.4596.0481).
- [35] Raymond M. Fish and Leslie A. Geddes. “Conduction of Electrical Current to and Through the Human Body: A Review”. In: *Eplasty* 9 (2009).

- [36] *Medical electrical equipment — Part 1-11: General requirements for basic safety and essential performance — Collateral standard: Requirements for medical electrical equipment and medical electrical systems used in the home healthcare environment*. Standard. Geneva, CH: International Organization for Standardization, Jan. 2015.
- [37] Andy Adler and Alistair Boyle. “Electrical Impedance Tomography”. In: (May 2019), pp. 1–16. DOI: [10.1002/047134608x.w1431.pub2](https://doi.org/10.1002/047134608x.w1431.pub2).
- [38] Akinori Ueno et al. “Feasibility of Capacitive Sensing of Surface Electromyographic Potential through Cloth”. In: *Sensors and Materials* 24 (Jan. 2012), pp. 335–346.
- [39] Lei Zhang et al. “Fully organic compliant dry electrodes self-adhesive to skin for long-term motion-robust epidermal biopotential monitoring”. In: *Nature Communications* 11.1 (Sept. 2020), p. 4683. ISSN: 2041-1723. DOI: [10.1038/s41467-020-18503-8](https://doi.org/10.1038/s41467-020-18503-8). URL: <https://doi.org/10.1038/s41467-020-18503-8>.
- [40] Lin Yang et al. “Optimal combination of electrodes and conductive gels for brain electrical impedance tomography”. In: *BioMedical Engineering OnLine* 17.1 (Dec. 2018), p. 186. ISSN: 1475-925X. DOI: [10.1186/s12938-018-0617-y](https://doi.org/10.1186/s12938-018-0617-y). URL: <https://doi.org/10.1186/s12938-018-0617-y>.
- [41] Momona Yamagami et al. “Assessment of Dry Epidermal Electrodes for Long-Term Electromyography Measurements”. In: *Sensors (Basel, Switzerland)* 18 (Apr. 2018). DOI: [10.3390/s18041269](https://doi.org/10.3390/s18041269).
- [42] *Multiprotocol wireless 32-bit MCU Arm®-based Cortex®-M4 with FPU, Bluetooth® 5.2 and 802.15.4 radio solution*. DS11929. Rev. 13. ST Microelectronics. 2022. URL: <https://www.st.com/resource/en/datasheet/stm32wb55rg.pdf>.
- [43] E. Chassande-Mottin and P. Flandrin. “On the stationary phase approximation of chirp spectra”. In: *Proceedings of the IEEE-SP International Symposium on Time-Frequency and Time-Scale Analysis (Cat. No.98TH8380)*. 1998, pp. 117–120. DOI: [10.1109/TFSA.1998.721375](https://doi.org/10.1109/TFSA.1998.721375).
- [44] MathWorks Inc. *PRBS Input Signals*. URL: <https://www.mathworks.com/help/slcontrol/ug/prbs-input-signals.html> (visited on 08/01/2022).
- [45] Zeyang Geng et al. “On-board Impedance Diagnostics Method of Li-ion Traction Batteries Using Pseudo-Random Binary Sequences”. In: *2018 20th European Conference on Power Electronics and Applications (EPE'18 ECCE Europe)*. 2018, P.1–P.9.
- [46] Dimitris G. Manolakis and Vinay K. Ingle. *Applied Digital Signal Processing: Theory and Practice*. Cambridge University Press, 2011. DOI: [10.1017/CB09780511835261](https://doi.org/10.1017/CB09780511835261).
- [47] P Bertemes-Filho et al. “Mirrored Modified Howland Circuit for Bioimpedance Applications: Analytical Analysis”. In: *Journal of Physics: Conference Series* 407 (Dec. 2012), p. 012030. DOI: [10.1088/1742-6596/407/1/012030](https://doi.org/10.1088/1742-6596/407/1/012030). URL: <https://doi.org/10.1088/1742-6596/407/1/012030>.



- [48] *High-Speed, Precision, Gain of 0.2 Level Translation Difference Amplifier*. SBOS333B. Rev. B. Texas Instruments. 2005. URL: <https://www.ti.com/lit/ds/symlink/ina159.pdf>.
- [49] All About Circuits. *The Instrumentation Amplifier*. URL: <https://www.allaboutcircuits.com/textbook/semiconductors/chpt-8/the-instrumentation-amplifier/> (visited on 08/20/2022).
- [50] *Zero Drift, Digitally Programmable Instrumentation Amplifier*. AD8231. Rev. E. Analog Devices. 2017. URL: <https://www.analog.com/media/en/technical-documentation/data-sheets/AD8231.pdf>.
- [51] ElectronicsTutorials. *Non-inverting Operational Amplifier*. URL: [https://www.electronics-tutorials.ws/opamp/opamp\\_3.html](https://www.electronics-tutorials.ws/opamp/opamp_3.html) (visited on 08/20/2022).
- [52] *0.2  $\mu\text{V}/^\circ\text{C}$  Offset Drift, 105 MHz Low Power, Low Noise, Rail-to-Rail Amplifiers*. ADA4805. Rev. B. Analog Devices. 2014. URL: [https://www.analog.com/media/en/technical-documentation/data-sheets/ADA4805-1\\_4805-2.pdf](https://www.analog.com/media/en/technical-documentation/data-sheets/ADA4805-1_4805-2.pdf).
- [53] Wikipedia. *Multiplexer*. URL: <https://en.wikipedia.org/wiki/Multiplexer> (visited on 08/20/2022).
- [54] MathWorks Inc. *Sampling Clock Source, generate clock signal with aperture jitter*. 2019. URL: <https://mathworks.com/help/msblks/ref/samplingclocksource.html> (visited on 07/29/2022).
- [55] Wikipedia. *Phase-locked loop*. URL: [https://en.wikipedia.org/wiki/Phase-locked\\_loop](https://en.wikipedia.org/wiki/Phase-locked_loop) (visited on 08/20/2022).
- [56] Pierre Geurts and Louis Wehenkel. *Introduction to Machine Learning*. 2021.
- [57] Emma Rosa Malone. “Multifrequency methods for Electrical Impedance Tomography”. PhD thesis. Department of Medical Physics and Biomedical Engineering, University College London, 2015.
- [58] Andy Adler and William RB Lionheart. “Uses and abuses of EIDORS: an extensible software base for EIT”. In: *Physiological measurement* 27.5 (2006), S25.
- [59] Jaakko Malmivuo and Robert Plonsey. “Bioelectromagnetism. 26. Impedance Tomography”. In: Jan. 1995, pp. 420–427. ISBN: 978-0195058239.
- [60] Wikipedia. *Gauss–Newton algorithm*. URL: [https://en.wikipedia.org/wiki/Gauss%E2%80%93Newton\\_algorithm](https://en.wikipedia.org/wiki/Gauss%E2%80%93Newton_algorithm) (visited on 07/21/2022).
- [61] Md. Rabiul Islam and Md. Adnan Kiber. “Electrical Impedance Tomography imaging using Gauss-Newton algorithm”. In: *2014 International Conference on Informatics, Electronics & Vision (ICIEV)*. 2014, pp. 1–4. DOI: [10.1109/ICIEV.2014.6850719](https://doi.org/10.1109/ICIEV.2014.6850719).
- [62] Andy Adler. *Iterative Gauss Newton reconstruction in 3D*. 2017. URL: [http://eidors3d.sourceforge.net/tutorial/adv\\_image\\_reconst/basic\\_iterative.shtml](http://eidors3d.sourceforge.net/tutorial/adv_image_reconst/basic_iterative.shtml) (visited on 08/11/2022).
- [63] Wikipedia. *Tikhonov regularization* — Wikipedia, The Free Encyclopedia. <http://en.wikipedia.org/w/index.php?title=Tikhonov%20regularization&oldid=1085400279>. [Online; accessed 11-August-2022]. 2022.

- [64] Vidya Sarode, Sneha Patkar, and A.N. Cheeran. “Comparison of 2-D Algorithms in EIT based Image Reconstruction”. In: *International Journal of Computer Applications* 69 (May 2013), pp. 6–11. DOI: [10.5120/11860-7642](https://doi.org/10.5120/11860-7642).
- [65] M Cheney et al. “NOSER: An algorithm for solving the inverse conductivity problem”. In: *International journal of imaging systems and technology*. 2.2 (1990). ISSN: 0899-9457.
- [66] Andrea Borsic et al. “Total Variation Regularization in Electrical Impedance Tomography”. In: (May 2007). ISSN: 1749-9097. URL: <http://eprints.man.ac.uk/813/>.
- [67] Abhimanyu Dubey on Quora. *When would you chose L1-norm over L2-norm?* 2016. URL: <https://www.quora.com/When-would-you-chose-L1-norm-over-L2-norm> (visited on 08/18/2022).
- [68] Andy Adler et al. “GREIT: A unified approach to 2D linear EIT reconstruction of lung images”. In: *Physiological measurement* 30 (July 2009), S35–55. DOI: [10.1088/0967-3334/30/6/S03](https://doi.org/10.1088/0967-3334/30/6/S03).
- [69] Benyuan Liu et al. “pyEIT: A python based framework for Electrical Impedance Tomography”. In: *SoftwareX* 7 (2018), pp. 304–308.
- [70] The Photon (<https://electronics.stackexchange.com/users/6334/the-photon>). *Implementing guard trace/ring in PCB design*. Electrical Engineering Stack Exchange. URL: <https://electronics.stackexchange.com/q/24890> (version: 2012-01-11). eprint: <https://electronics.stackexchange.com/q/24890>. URL: <https://electronics.stackexchange.com/q/24890>.
- [71] Michael Swindle. “Porcine Integumentary System Models: Wound Healing”. In: *Journal of Physics: Conference Series* (). URL: <https://info.sinclairresearch.com/porcine-integumentary-system-models-wound-healing>.
- [72] Cook’n & Eat’n. *What Happens When Meat Freezes?* 2018. URL: <https://www.dvo.com/newsletter/weekly/2018/1-19-193/notes1.html> (visited on 08/10/2022).